Euler-Lagrangian Simulations of Turbulent Bubbly Flow

A DISSERTATION
SUBMITTED TO THE FACULTY OF THE GRADUATE SCHOOL
OF THE UNIVERSITY OF MINNESOTA
BY

Michael David Mattson

IN PARTIAL FULFILLMENT OF THE REQUIREMENTS
FOR THE DEGREE OF
DOCTOR OF PHILOSOPHY

Krishnan Mahesh, Adviser

March 2011

Acknowledgements

First and foremost, I would like to thank my adviser, Prof. Krishnan Mahesh for his advice, encouragement and support. I have greatly benefitted from his experience and expertise and I am grateful for the opportunity to work alongside a great teacher and mentor.

My parents, Brian and Robin, have been a source of great support and inspiration. Without them, this achievement would not have been possible. My brothers, sister, grandparents and extended family have always supported me in my endeavors and I am very grateful.

My coworkers and close friends have been very supportive and provided helpful advice and many wonderful conversations. In no particular order, I would like to thank Dr. Suman Muppidi, Prof. Jeffrey Doom, Zane Nitzkorski, Dr. Pradeep Babu, Aman Verma, Prahladh Iyer, Raja Asaithambi, Aswin Gnanaskandan, Hyunchul Jang and Xiaochuan Chai. I have enjoyed sharing this chapter of my life with them and wish them all a happy and successful future. I would especially like to thank Erin Skiba for all of her support.

This work was supported by the United States Office of Naval Research under ONR Grant N00014-07-1-0420 with Dr. Ki-Han Kim as technical monitor. Computing resources were provided by the Minnesota Supercomputing Institute (MSI), Arctic Region Supercomputing Center (ARSC), the San Diego Supercomputing Center (SDSC), the National Institute for Computational Sciences (NICS) and the Texas Advanced Computing Center (TACC).

To my parents and grandparents

Abstract

A novel one-way coupled Euler-Lagrangian approach, including bubble-bubble collisions, coalescence and variable bubble radius, was developed in the context of simulating large numbers of cavitating bubbles in complex geometries using direct numerical simulation (DNS) and large-eddy simulation (LES). This dissertation i) describes the development of the Euler-Lagrangian approach, ii) outlines the novel bubble coalescence model derived for this approach and iii) describes simulations performed of bubble migration in a turbulent boundary layer, bubble coalescence in a turbulent pipe flow and cavitation inception in turbulent flow over a cavity.

The coalescence model uses a hard-sphere collision model is used and determines coalescence stochastically. The probability of coalescence is computed from a ratio of coalescence timescales, which are dynamically determined from the simulation. Coalescence in a bubbly, turbulent pipe flow ($\mathrm{Re}_\tau = 1920$) in microgravity was simulated with conditions similar to experiments by Colin et al. [1] and excellent agreement of bubble size distribution was obtained. With increasing downstream distance, the number density of bubbles decreases due to coalescence and the average probability of coalescence decreases due to an increase in overall bubble size.

The Euler-Lagrangian approach was used to simulate bubble migration in a turbulent boundary layer ($420 < \mathrm{Re}_\theta < 1800$). Simulation parameters were chosen to match Sanders et al. [2], although the Reynolds number of the simulation is lower than the experiment. The simulations show that bubbles disperse away from the wall as observed experimentally. Mean bubble diffusion and profiles of bubble concentration are found to be similar to the passive scalar results, except very near the wall. The carrier-fluid acceleration was found to be the reason for moving the bubbles away from the wall.

The one-way coupled Euler-Lagrangian approach was applied to simulate the experiment of cavitating turbulent flow over a cavity by Liu and Katz [3]. The classical Rayleigh-Plesset equation is integrated using adaptive time-stepping to accurately and efficiently solve for the change of the bubble radius over time. The one-way coupled Euler-Lagrangian model predicts cavitation inception at the trailing edge of the cavity and also in the vortices shed from the leading edge, in qualitative agreement with experiment.

Contents

Acknowledgements **i**

Abstract **iii**

List of Figures **vii**

List of Tables **xiii**

Abbreviations **xiv**

Physical Constants **xv**

Symbols **xvi**

1 Introduction **1**
1.1 Motivation and background 1
1.2 Numerical challenges 4
1.2.1 Bubble physics and modeling 4
1.2.2 Turbulence modeling and simulations 5
1.3 Review of past work 8
1.4 Overview 10

2 Numerical Methods **12**
2.1 Free-surface axisymmetric Navier-Stokes approach 12
2.1.1 Numerical details 13
2.1.2 Validation 17
2.1.2.1 Bubble oscillation in a sinusoidal acoustic field 17
2.1.2.2 Bubble collapse near wall 18
2.1.3 Comments 19
2.2 Force coupling method 20
2.2.1 Numerical approach 20
2.2.2 Validation: Single sphere rising in an inclined channel 23
2.2.3 Comments 25
2.3 One-way coupled Euler-Lagrangian approach 25
2.3.1 Carrier-phase solver 26
2.3.2 Equations of bubble motion - constant bubble radius 28

2.3.3 Accounting for change in bubble size . . . 30
2.3.4 Bubble time integration . . . 32
2.3.5 Time integration of bubble radius . . . 35
2.3.6 RK4 validation: a single oscillating bubble . . . 40
2.3.7 Validation: Gas nuclei trajectories over a blunt body . . . 41
2.3.8 Collision Model . . . 45
2.3.8.1 Constant Radius . . . 45
2.3.8.2 Allowing for variable radius . . . 47
2.3.8.3 Collision list . . . 48
2.3.9 Coalescence Model . . . 52
2.3.10 Conservation of kinetic energy . . . 53
2.3.11 Interaction time . . . 57
2.3.12 Drainage time . . . 58
2.3.13 Collision, no coalescence . . . 59
2.3.14 Collision, with coalescence . . . 60

3 Bubble migration in a turbulent boundary layer 61
3.1 Introduction . . . 61
3.2 Computational and Physical Parameters . . . 63
3.3 Results . . . 66
3.3.1 Carrier-phase Turbulence . . . 66
3.3.2 Bubble Trajectories . . . 66
3.3.3 Budgets of Bubble Acceleration . . . 69
3.3.4 Role of Turbulence: Bubbles in a Laminar Boundary Layer . . . 76
3.3.5 Effect of Bubble Size . . . 78
3.3.6 Comparison to a Passive Scalar . . . 80
3.4 Discussion . . . 82

4 Coalescence in a turbulent pipe flow 86
4.1 Introduction . . . 86
4.2 Model validation . . . 87
4.3 Results . . . 91
4.3.1 Single-Phase Turbulence . . . 91
4.3.2 Effect of coalescence . . . 91
4.4 Collision details . . . 93
4.5 Discussion . . . 97

5 Cavitation in a turbulent flow over a cavity 107
5.1 Computational and Physical Parameters . . . 108
5.2 Low Reynolds-number simulation . . . 110
5.2.1 Single-phase statistics . . . 112
5.2.2 Cavitating flow . . . 114
5.3 High Reynolds-number simulation . . . 116
5.3.1 Single-phase statistics . . . 118

5.3.2 Cavitating flow 119

Bibliography **125**

A Bubble time integration **133**

B 2nd-order spatial interpolation **135**

List of Figures

1.1 Cavitation damage to a Francis turbine, with large sections of the blades completely worn away [10]. . . . 3
1.2 Transition from sheet-to-cloud cavitation (Callenaere et al. [12]). Flow is from left to right. . . . 6
1.3 Schematic of the computational grid of a free-surface DNS simulation. The small flow scales around the bubble (blue) and the bubble surface are fully resolved. . . . 7
1.4 Schematic of the computational grid of an Euler-Lagrangian simulation, with the bubbles (blue) smaller than the computational mesh. . . . 7
1.5 Schematic of the computational grid of an Euler-Euler simulation, with the bubble phase (blue) and carrier-phase (white) both described by continuum equations. . . . 8

2.1 Schematic of grid and bubble interface of the axisymmetric Navier-Stokes solver. The bubble interface is described by N marker points located at position S_i. . . . 14
2.2 Control volume discretization of free-surface Navier-Stokes equations for u_r. . . . 16
2.3 Bubble oscillation (R/R_o versus t) in a sinusoidally-varying pressure field. —, free-surface Navier-Stokes; —, Rayleigh-Plesset. . . . 17
2.4 Evolution of bubble collapsing near a wall at Re = 18.4. Wall is along the bottom of each box. Time between each frame is 0.634 non-dimensional units of time, based on a timescale of $\sqrt{\rho_f R_o^2/p_\infty}$. . . . 19
2.5 Evolution of bubble collapsing near a wall at Re = 18.4 for the Popinet and Zaleski [23] simulation. Wall is along the bottom of each box. . . . 20
2.6 Schematic of the computational grid of an FCM simulation, with each bubble represented by a discrete Lagrangian element that is resolved by ~ 5 grid points across the diameter. . . . 21
2.7 Comparison of bubble trajectories and velocities with experiment. The simulation quantities are represented by small black squares (■) and experimental quantities are represented by red squares (□). Figure (a) plots the advance of the particle position, while figures (b) and (c) plot the particle streamwise and stream-normal velocities vs. y-position, respectively. 24

2.8 Schematic of Lagrangian bubbles (blue spheres) distributed throughout the unstructured domain between two processors on a two-dimensional grid. Vectors denote instantaneous velocity of discrete bubble. The thick line represents the inter-processor boundary of processors 1 and 2. 26
2.9 Discretization of control volume and face-normal velocities (u_i and $u_{f,i}$, respectively). u_i is located at the control volume centroid and $u_{f,i}$ is located at the face centroid. The face-normal vector $\hat{n}$ points from icv1 to icv2. 27
2.10 Discretization of fluid timestep Δt and bubble timestep Δt_{bub} from time t_1 to t_2. 32
2.11 Discretization of bubble timestep Δt_{bub} and Runge-Kutta timestep Δt_{RK} from time t_k to t_{k+1}. 35
2.12 Convergence of bubble radius vs. time for different values of ϵ. 40
2.13 Relationship between ϵ and runtime. 41
2.14 Unstructured mesh generated for simulation of gas nuclei flowing over a blunt body. (a) Full mesh. (b) Zoomed-in view near blunt body. 43
2.15 Comparison of bubble trajectories to Johnson and Hsieh [38], with $\sigma_v = 0.4$. The data by Johnson and Hsieh [38] is given in (a) by the filled circles, with $y_o/h = 0.05$ (•), $y_o/h = 0.1$ (•) and $y_o/h = 0.2$ (•). Figure (b) plots bubble trajectories along with pressure color contours and velocity streamlines. Red represents high pressure and blue low pressure. 44
2.16 Schematic of parameters of collision between bubble 1 and bubble 2. . . . 46
2.17 Schematic of collision partner calculations for bubbles 1 and 2. Arrows denote evaluation of collision timescale for bubble i with j. 49
2.18 Schematic of collision partner calculations for bubble $i = 4$, which has just collided with another bubble and requires updating to find its new collision partner. 51
2.19 Update procedure for collision list when losing / gaining particles on processor after inter-processor communication or injection of bubbles. (a): Bubbles a and c have previously computed bubbles e as collision partner. Bubbles b and c have been moved to another processor. Bubbles f and g have been passed into the local processor from another processor or through bubble injection directly. (b): Packing procedure has been applied so that all local bubbles (from 1 to N_{sys}) are included in updated collision list. Collision partners updated for bubbles f and g through down-list procedure. 51

3.1 Comparison of mean streamwise velocity to results from the Simens et al. [66] simulation. —, DNS, ($\text{Re}_\theta = 1100$); - -, DNS, ($\text{Re}_\theta = 1551$); □, Simens, ($\text{Re}_\theta = 1100$). △, Simens, ($\text{Re}_\theta = 1551$). 65
3.2 Comparison of turbulence intensities to results from the Simens et al. [66] simulation. (a) RMS of the turbulence intensities versus wall-normal distance for $\text{Re}_\theta = 1100$. (b) RMS of the turbulence intensities versus wall-normal distance for $\text{Re}_\theta = 1551$. —, $u^+_{x,\text{rms}}$, DNS; - -, $u^+_{y,\text{rms}}$, DNS; -···-, $u^+_{z,\text{rms}}$, DNS; □, $u^+_{x,\text{rms}}$, Simens; △, $u^+_{y,\text{rms}}$, Simens; ▷, $u^+_{z,\text{rms}}$, Simens. 65

3.3 Instantaneous bubble position with only a part of the domain shown ($5 < x < 15$). (a) Bubble position in streamwise and wall-normal coordinates with ensemble-averaged position $\langle Y_y \rangle_e$ vs. $\langle Y_x \rangle_e$ shown by the black line. (b) Close-up view of (a) along with bubble velocity vectors (v_x, v_y). (c) Bubble position in streamwise and spanwise coordinates. 66
3.4 Ensemble-averaged bubble trajectory and evolution of boundary layer thickness, along with bubble concentration profiles. Bubble concentration C is plotted versus y/L_{ref} at $x/L_{\text{ref}} = 10, 15, 20$ and 25. - -, δ_{99}; —, $\langle Y_y \rangle_e$ vs. $\langle Y_x \rangle_e$; ■, C. 67
3.5 Ensemble-averaged bubble and carrier-fluid velocities. —, $\langle v_x \rangle_e$; - - -, $\langle v_y \rangle_e$; ■, $\langle u_x \rangle_e$; -···-, $\langle u_y \rangle_e$. 67
3.6 Ensemble-averaged position fluctuations. —, $\langle Y'_x Y'_x \rangle_e$; - -, $\langle Y'_y Y'_y \rangle_e$; -···-, $\langle Y'_x Y'_y \rangle_e$. 68
3.7 Ensemble-averaged velocity fluctuations. —, $\langle v'_x v'_x \rangle_e$; - -, $\langle v'_y v'_y \rangle_e$; -···-, $\langle v'_x v'_y \rangle_e$. 68
3.8 Ensemble-averaged bubble acceleration budget in the streamwise (x) direction. - -, $3\frac{Du_x}{Dt}$; □, Drag_x; -···-, Lift_x; —, Total_x. 70
3.9 Ensemble-averaged bubble acceleration budget in the wall-normal (y) direction. (a) Normal view showing all terms individually. - -, Drag_y; -···-, $3\frac{Du_y}{Dt}$; □, Lift_y; · · ·, $-2g$; —, Total_y. (b) Zoomed-in view with the drag and fluid acceleration terms summed together. -···-, $(\text{Drag}_y + 3\frac{Du_y}{Dt})$; □, Lift_y; · · ·, $-2g$; —, Total_y. 71
3.10 Comparison of drag acceleration in the wall-normal direction for the approximate equation and measured result. 72
3.11 Budget of fluid acceleration in the y-direction. 73
3.12 Budget of lift acceleration in the y-direction. 73
3.13 Bubble trajectory in the laminar boundary layer. 75
3.14 Bubble acceleration budget in the wall-normal (y) direction for the laminar boundary layer simulation. □, Drag_y; ▷, $-2g$; —, Total_y. 77
3.15 Bubble trajectories for 3 differently-sized bubbles in a turbulent boundary layer. - -, $R/\delta_{99,\text{inj}} = 0.0037$; —, $R/\delta_{99,\text{inj}} = 0.0064$; -···-, $R/\delta_{99,\text{inj}} = 0.0092$. 78
3.16 Bubble acceleration in the wall-normal direction for 3 differently-sized bubbles in a turbulent boundary layer, with (a) plotting the drag acceleration, (b) the fluid acceleration and (c) the lift acceleration. - -, $R/\delta_{99,\text{inj}} = 0.0037$; —, $R/\delta_{99,\text{inj}} = 0.0064$; -···-, $R/\delta_{99,\text{inj}} = 0.0092$. 79
3.17 Diffusion of a passive scalar and bubbles in a turbulent boundary layer. . 80
3.18 Concentration profiles for a passive scalar and bubbles in the intermediate zone of a turbulent boundary layer, with the inset figure plotting a near-wall close-up view. $x/\text{L}_{\text{ref}} = (7.5, 9.4, 11.2, 13.1, 15.0) = (\square, \diamond, \triangleleft, \triangleright, \text{x})$. —, Poreh and Cermak [30] intermediate zone. 81

3.19 Concentration profiles for a passive scalar and bubbles in the transition zone of a turbulent boundary layer. Figure (a) shows results for scaling using λ, with the inset figure plotting a near-wall close-up view. $x/\mathrm{L_{ref}}$ = (17.5, 22.5, 27.5, 32.5, 37.5) = (□, ◇, ▷, ◁, x). —, Poreh and Cermak [30] intermediate zone. Figure (b) shows scaling with δ_{99}, with the inset figure plotting a near-wall close-up view. $x/\mathrm{L_{ref}}$ = (17.5, 22.5, 27.5, 32.5, 37.5) = (□, ◇, ▷, ◁, x). —, Poreh and Cermak [30] final zone. 83

4.1 (a) Cross-sectional mesh of turbulent pipe. (b) Time-averaged streamwise carrier-fluid velocity as a function of distance from the wall, as compared to experiment. —, DNS; □, Lawn [78]. 90

4.2 Time-averaged turbulent fluctuations versus distance from the center of the pipe. (a) RMS fluctuations as compared to experiment. —, $(u'_{x,\mathrm{rms}})^+$ DNS; - -, $(u'_{r,\mathrm{rms}})^+$ DNS; □, $(u'_{x,\mathrm{rms}})^+$ Lawn [78]; △, $(u'_{r,\mathrm{rms}})^+$ Lawn [78]. (b) Reynolds shear stress. —, $\langle u'_x u'_r \rangle^+$ DNS; □, $\langle u'_x u'_r \rangle^+$ Lawn [78]. . . . 92

4.3 Inflow and outflow bins for measurement of bubble properties. The length of the inflow/outflow bins is $L_2 = 10D$. The distance between the inflow and outflow bins is L_1. The total distance to the end of the last measurement section is $2L_2 + L_1 = 70D$. 92

4.4 Streamwise bins for measurement of bubble properties. Each bin ($i = 1, 2, 3, ...$) samples data from bubbles that reside within its streamwise domain ($x_i - \Delta x_i/2 \leq x \leq x_i + \Delta x_i/2$). 93

4.5 Comparison of probability distribution function of bubble size from simulation to Colin et al. [1] experiment. Inflow distribution is sampled over $0 \leq x/D \leq 10$ and outflow distribution is sampled over $60 \leq x/D \leq 70$. Solid lines represent simulation results and bars represent results from Colin et al. [1]. 93

4.6 Instantaneous position of bubbles in turbulent pipe flow, with coalescence. Bubbles are proportional to actual size. Flow is from left to right. View is looking through the pipe, perpendicular to the pipe flow, with the top and bottom boundaries of each figure at $r/D = 0.5$. (a) Near inflow ($4 \leq x/D \leq 6$). (b) Near outflow ($68 \leq x/D \leq 70$). 94

4.7 (a) Streamwise evolution of total number of collisions N_c. (b) Streamwise evolution of mean probability of coalescence $\overline{P_\mathrm{c}}$. 99

4.8 Number of collisions $N_\mathrm{c}(x, d_1, d_2)$ vs. d_1, d_2 for (a) $0 \leq x/D \leq 10$, (b) $10 \leq x/D \leq 20$, (c) $20 \leq x/D \leq 30$, (d) $45 \leq x/D \leq 55$, including coalescence. 100

4.9 Probability of coalescence $\overline{P_\mathrm{c}}(x, d_1, d_2)$ vs. d_1, d_2 for (a) $0 \leq x/D \leq 10$, (b) $10 \leq x/D \leq 20$, (c) $20 \leq x/D \leq 30$, (d) $45 \leq x/D \leq 55$, including coalescence. 101

4.10 (a) Streamwise evolution of t_d/t_i. (b) PDF of t_d/t_i for four streamwise locations: —, $0 \leq x/D \leq 10$; - -, $20 \leq x/D \leq 30$; -···-, $45 \leq x/D \leq 55$; $\cdots$, $70 \leq x/D \leq 80$ 102

4.11 Ratio of coalescence timescales $\overline{t_d/t_i}(x, d_1, d_2)$ vs. d_1, d_2 for (a) $0 \leq x/D \leq 10$, (b) $10 \leq x/D \leq 20$, (c) $20 \leq x/D \leq 30$, (d) $45 \leq x/D \leq 55$, including coalescence. 102

4.12 (a) Streamwise evolution of the magnitude of the relative velocity V_o between colliding bubbles. (b) PDF of R_c for four streamwise locations: —, $0 \leq x/D \leq 10$; - -, $20 \leq x/D \leq 30$; -···-, $45 \leq x/D \leq 55$; · · ·, $70 \leq x/D \leq 80$ 103
4.13 Relative velocity of collision $\overline{V_o}(x, d_1, d_2)$ vs d_1, d_2 for (a) $0 \leq x/D \leq 10$, (b) $10 \leq x/D \leq 20$, (c) $20 \leq x/D \leq 30$, (d) $45 \leq x/D \leq 55$, including coalescence. 103
4.14 (a) Streamwise evolution of $\overline{\mathrm{Re}_{\mathrm{eq}}}$. (b) PDF of $\mathrm{Re}_{\mathrm{eq}}$ for four streamwise locations: —, $0 \leq x/D \leq 10$; - -, $20 \leq x/D \leq 30$; -···-, $45 \leq x/D \leq 55$; · · ·, $70 \leq x/D \leq 80$ 104
4.15 Collision Reynolds number $\overline{\mathrm{Re}_{\mathrm{eq}}}(x, d_1, d_2)$ vs. d_1, d_2 for (a) $0 \leq x/D \leq 10$, (b) $10 \leq x/D \leq 20$, (c) $20 \leq x/D \leq 30$, (d) $45 \leq x/D \leq 55$, including coalescence. 104
4.16 (a) Streamwise evolution of $\overline{d_{\mathrm{eq}}}$. (b) PDF of d_{eq} for four streamwise locations: —, $0 \leq x/D \leq 10$; - -, $20 \leq x/D \leq 30$; -···-, $45 \leq x/D \leq 55$; · · ·, $70 \leq x/D \leq 80$ 105
4.17 (a) Streamwise evolution of $\overline{\mathrm{We}_{\mathrm{eq}}}$. (b) PDF of $\mathrm{We}_{\mathrm{eq}}$ for four streamwise locations: —, $0 \leq x/D \leq 10$; - -, $20 \leq x/D \leq 30$; -···-, $45 \leq x/D \leq 55$; · · ·, $70 \leq x/D \leq 80$ 105
4.18 (a) Streamwise evolution of θ_c. (b) PDF of θ_c for four streamwise locations: —, $0 \leq x/D \leq 10$; - -, $20 \leq x/D \leq 30$; -···-, $45 \leq x/D \leq 55$; · · ·, $70 \leq x/D \leq 80$ 106
4.19 (a) Streamwise evolution of R_c. (b) PDF of R_c for four streamwise locations: —, $0 \leq x/D \leq 10$; - -, $20 \leq x/D \leq 30$; -···-, $45 \leq x/D \leq 55$; · · ·, $70 \leq x/D \leq 80$ 106

5.1 Domain of the cavity simulation. 109
5.2 Computational mesh near the trailing edge for the low Reynolds-number simulation. 111
5.3 Mean streamwise velocity $\overline{u_x}$ near trailing edge. 112
5.4 Mean streamwise velocity $\overline{u_y}$ near trailing edge, along with mean fluid streamlines. 112
5.5 Mean pressure coefficient $\overline{C_p}$ near trailing edge. 113
5.6 Pressure coefficient rms value $C_{p,\mathrm{rms}}$ near trailing edge. 113
5.7 Instantaneous pressure coefficient C_p. 114
5.8 Instantaneous plots of bubble size and position near the cavity trailing edge. Figures (a)-(d) are sequential in time, with individual vortices denoted by v_a, v_b and v_c. 116
5.9 Computational mesh for the high Reynolds-number simulation, focused on the trailing edge. 117
5.10 Comparison of mean velocities and streamlines between simulation and the Liu and Katz [3] experiment. (a) Plot of $\overline{u_x}$ from LES simulation (b) Plot of $\overline{u_y}$ from simulation, along with velocity streamlines. (c) Plot of $\overline{u_x}$ from Liu and Katz [3]. (d) Plot of $\overline{u_y}$ from Liu and Katz [3], along with velocity streamlines. 121

5.11 Comparison of mean pressure coefficient $\overline{C_p}$ between simulation and the Liu and Katz [3] experiment. (a) Plot of $\overline{C_p}$ from LES simulation (b) Plot of $\overline{C_p}$ from Liu and Katz [3]. 122
5.12 Comparison of mean pressure coefficient $C_{p,\mathrm{rms}}$ between simulation and the Liu and Katz [3] experiment. (a) Plot of $C_{p,\mathrm{rms}}$ from LES simulation (b) Plot of $C_{p,\mathrm{rms}}$ from Liu and Katz [3]. 123
5.13 Plots of bubble instantaneous position at $t = 0.02L_{\mathrm{ref}}/U_{\mathrm{ref}}$ near the cavity trailing edge. Color contours plot the instantaneous radial acceleration for each bubble. (a) $x-y$ plane for $R_o = 20$ μm. (b) $x-z$ plane for $R_o = 20$ μm. (c) $x-y$ plane for $R_o = 25$ μm. (d) $x-z$ plane for $R_o = 25$ μm. (e) $x-y$ plane for $R_o = 30$ μm. (f) $x-z$ plane for $R_o = 30$ μm. 124

List of Tables

2.1 Experimental values 23
2.2 Domain parameters 23
2.3 Non-dimensional parameters 23
2.4 Parameters for Runge-Kutta integrator 36

3.1 Simulation Parameters 64

Abbreviations

BDR	**B**ubble-induced **D**rag **R**eduction
DNS	**D**irect **N**umerical **S**imulation
EL	**E**uler-**L**agrangian
FCM	**F**orce **C**oupling **M**ethod
LBL	**L**aminar **B**oundary **L**ayer
LES	**L**arge-**E**ddy **S**imulation
RANS	**R**eynolds-**A**veraged **N**avier-**S**tokes
RP	**R**ayleigh-**P**lesset
RK	**R**unge-**K**utta
TBL	**T**urbulent **B**oundary **L**ayer

Physical Constants

Surface tension of water	σ	=	7.34×10^{-2} N/m
Density of water	ρ_{f}	=	1.00×10^{3} kg/m^3
Density of air (standard cond.)	ρ_{g}	=	1.00×10^{0} kg/m^3
Kinematic viscosity of water	ν_{f}	=	1.12×10^{-6} m^2/s
Dynamic viscosity of water	μ_{f}	=	1.0×10^{-3} N s/m^2
Specific heat ratio (air)	γ	=	1.4

Symbols

x, y, z	Coordinate axes, coordinates	m
Re	Reynolds number	
Fr	Froude number	
We	Weber number	
$\vec{g}$	Gravitational vector	$\mathrm{m/s^2}$
$\vec{x}$	Eulerian position vector	m
$R(t)$	Bubble radius	m
$d(t)$	Bubble diameter	m
$\vec{Y}(t)$	Bubble position vector	m
$\vec{u}(\vec{x},t)$	Fluid velocity vector	m/s
$\vec{v}(t)$	Bubble velocity vector	m/s
$p(\vec{x},t)$	Pressure	Pa
m	Mass occupied by bubble	kg
C_{D}	Drag coefficient	
C_{L}	Drag coefficient	
C_{M}	Added-mass coefficient	
C_p	Pressure coefficient	
A_{b}	Bubble area	$\mathrm{m^2}$
U	Reference velocity	m/s
Δt	Timestep	s
ρ	Density	$\mathrm{kg/m^2}$
μ	Dynamic viscosity	$\mathrm{N{\cdot}s/m^2}$

ν	Kinematic viscosity	m^2/s
$\vec{\omega}(\vec{x}, t)$	Vorticity vector	$1/s$
σ	Surface tension	N/m
σ_v	Cavitation index	
σ_i	Cavitation inception index	

Chapter 1

Introduction

1.1 Motivation and background

Bubbly flows are important for a wide range of practical applications. For example, bubbles are used in industry to enhance mixing through the effect of buoyancy, such as in air-sparged reactors. Distillation towers are used to separate crude oil into useful forms, where the oil is heated until gas bubbles form. The hydrocarbons can then be separated out by density, as heavier products liquefying and are siphoned off and progressively lighter petroleum products rising towards the top. Bubbles are also critical in many heat transfer problems where liquid water contacting a hot surface boils and the resulting vapor bubbles remove heat through phase change then carry away the the heat. Bubbles are also frequently observed in marine flows, where bubbles can be found in bow waves of ships. The presence of bubbles have been shown to drastically modify the speed of sound in the bubbly mixture, which has implications for marine acoustic signatures and detection. Since the work of McCormick and Bhattacharyya [4], bubbles have also been used in attempts to reduce viscous drag on marine vehicles, though the application of micro-bubble drag reduction is limited [5].

Bubbles are sensitive to pressure variations in the flow, responding by contracting or expanding in size. If the local pressure is low enough, bubbles can grow explosively. This process of rapid growth (and subsequent violent collapse) is the definition of cavitation.

Cavitation is a common and complex engineering problem. In any device with fluid flow, cavitation may occur, leading to deleterious behavior such as large power surges in turbo-machinery and unsteady loading on hydrofoil surfaces. Cavitation also has been put to many practical uses, such as ultrasonic cleaning of surfaces and targeted removal of kidney stones. Recently is has been used in decontamination of liquids [6]. Two practical questions are *When will cavitation occur?* and *How does cavitation affect the flow?* A fundamental parameter is the cavitation index

$$\sigma_v = \frac{p_o - p_v}{1/2\rho_{\mathrm{f}} U_o^2}, \tag{1.1}$$

where $p_o, p_v, \rho_{\mathrm{f}}$, and U_o are the reference (far-field) fluid pressure, vapor pressure, fluid density and reference velocity, respectively. Generally, when σ_v is above some critical value σ_c, cavitation effects on the flow are negligible. One critical value definition is the incipient cavitation number (σ_i), which is normally determined in water-tunnel testing by slowly lowering the tunnel pressure until cavitation is first observed. It is generally believed that cavitation begins from the growth of tiny gas nuclei that are always present in the flow, an idea first proposed by Harvey et al. [7]. In steady flow, the minimum pressure coefficient is

$$C_{p_{\min}} = \frac{p_{\min} - p_o}{1/2\rho_{\mathrm{f}} U_o^2}, \tag{1.2}$$

where $p_{\min}$ is the minimum pressure in the flow. If $p_{\min} = p_v$ then the incipient value σ_i is

$$\sigma_i = -C_{p_{\min}}. \tag{1.3}$$

However, in unsteady flows, cavitation inception becomes much more complicated and difficult to predict. For $\sigma_v < C_{p_{\min}}$, a gas nucleus present at the location of minimum pressure experiences $p < p_v$ for a finite time, though this amount of time may not be long enough for the nuclei to respond. Also, $C_{p_{\min}}$ is generally measured from a *mean* quantity and pressures lower than the minimum mean pressure can be obtained in unsteady and turbulent flows (e.g. in vortex cores). A recent comprehensive review investigating cavitation in vortical flows is Arndt [8]. Other important parameters are

FIGURE 1.1: Cavitation damage to a Francis turbine, with large sections of the blades completely worn away [10].

Reynolds number (Re), liquid temperature (T_∞), number and nature of the free-stream nuclei, amount of dissolved gas and quality of the solid surfaces [9].

Once inception has occurred, cavitation can drastically affect the performance of devices with liquid flow. For example, the pressure drag on underwater vehicles may be increased due to flow separation, the performance of propulsion devices such as propellers and impellers can be reduced and intense vibrations and noise can occur [11]. Noise created by cavitation is a particular problem for military submarines, since the increased noise that is generated enables enemy detection of the submarine through passive sonar. Also, the violent collapse of the cavitation bubbles creates an intense pressure wave that can damage nearby surfaces. Pitting and erosion by cavitation can lead to complete failure of the device. For example, Figure 1.1 shows the extensive cavitation damage on a Francis turbine, with the erosion of the turbine blades clearly evident.

The complexity of the flow is show by an important flow regime of sheet-to-cloud cavitation (SCC). Experiments performed by Callenaere et al. [12] highlight the unsteady flow structures of SCC, which is characterized by unstable regions of vapor bubbles that suddenly appear near the leading edge of a hydrofoil (See Figure 1.2). These bubble

"clouds" violently collapse as the free-stream pressure increases downstream of inception. This collapse leads to unsteady loading of the hydrofoil and emanates intense acoustic waves.

1.2 Numerical challenges

1.2.1 Bubble physics and modeling

Understanding the behavior of the gas nuclei and the turbulent flow is critical to the design process of devices with fluid flow. Experimental measurements of bubble properties are also made difficult due to the opacity of the multi-phase flow, making computational modeling a critical tool for understanding the physics of bubbly flows. Numerical simulations play a critical and expanding role as computational resources and methods become more powerful and robust. In devices with complex geometries, it is difficult to predict cavitation inception because the nature of the turbulence may not be known during the design process, and therefore computational modeling can be a critical and useful tool.

However, there are many challenges to simulating these flows. Large numbers of gas nuclei in the flow make simulations of large-scale applications difficult due to limitations on computational resources. In flows with a void fraction of 10^{-5} (above which two-way coupling effects become important [13]) the bubbly flow is dilute, and assuming gas nuclei with diameters of 50μm there are $\sim$ 15 bubbles per cm^3. As void fraction increases, bubble-bubble interactions (e.g. collisions and coalescence) become more important. When the void fraction increases to 10^{-1}, which is observed in many cavitating flows, the total number of bubbles increases to $\sim 1.5 \times 10^6$ per cm^3.

Bubble physics observed in bubbly flows is rich and complex, including (but not limited to) surface deformation and breakup, collisions and coalescence with other bubbles, and bubble growth and collapse. Contamination of the bubble surface by surfactants also affects bubble behavior through immobilization of (at least part of) the bubble surface and changing the zero-stress boundary condition at the bubble surface to a no-slip condition

[14]. The sum of contributions of small-scale physics at the bubble and sub-bubble level ultimately determines the behavior of bubbly flow. For example, in SCC interactions between the bubble cloud and the surrounding flow leads to a periodic attachment and detachment of the bubble cloud to the hydrofoil surface [12]. Resolving the detailed interaction of the small-scale flow with the bubble interface requires excessively fine grids, which when taken together with solving problems with large numbers of bubbles, is impractical and therefore must be modeled. The challenge is to develop robust, yet efficient and practical, numerical models of the complicated bubble physics to accurately predict these flows in full-scale applications.

Parallel processing has become an important method of reducing computational workload and runtime. By breaking the spatial domain of the simulation into N processors, the computational runtime can be reduced by a factor of $\sim N$. However, since the domain is now broken into discrete and separate elements, complications emerge that must be addressed. If bubbles are modeled as discrete elements (as in a Lagrangian approach), practical difficulties include inter-processor passing of the bubble from one processor's domain to another and calculating bubble-bubble collision partners. The unstructured nature of the grid increases the difficulty of these problems since finding which control volume and processor the bubble lies on is not easily known from bubble position. The Lagrangian numerical methods proposed in this thesis are generalized for parallel, unstructured grids, allowing efficient grid generation and simulation of large-scale bubbly flows in complex geometries.

1.2.2 Turbulence modeling and simulations

The carrier fluid surrounding the bubbles is described by the Navier-Stokes equations. Various methods may be used to solve the incompressible Navier-Stokes equations, with varying degrees of accuracy and efficiency. Popular methods such as the $k-\epsilon$, $k-\omega$ and Spalart-Almaras models solve the Reynolds-Averaged Navier-Stokes (RANS) equations. These methods remove the requirement to directly resolve all turbulent length-scales in the flow through modeling the Reynolds shear stress, greatly decreasing the computational requirements (i.e. reduced number of total control volumes and less-stringent grid

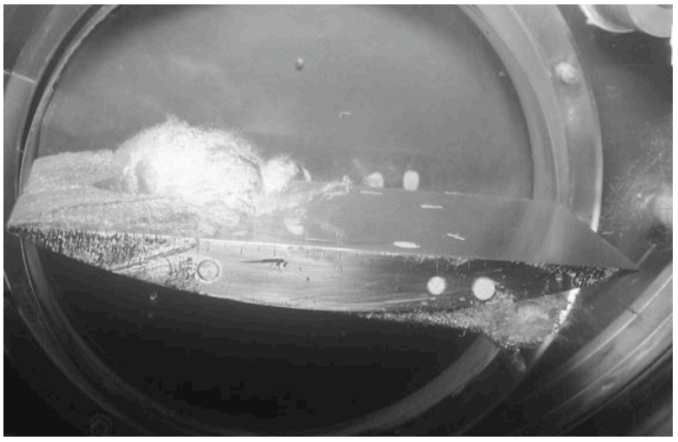

FIGURE 1.2: Transition from sheet-to-cloud cavitation (Callenaere et al. [12]). Flow is from left to right.

resolution) necessary to resolve the flow, but are generally not accurate in separated or complex flows [15]. Another approach is large-eddy simulation (LES), where the filtered Navier-Stokes equations are solved. The large scales (that contain a majority of the kinetic energy) are resolved and the sub-grid turbulent scales are modeled. This increases the accuracy for separated or complex flows [15]. Direct numerical simulation (DNS) requires full resolution of all turbulent scales and hence no turbulent models are required. However, because DNS requires full resolution of all scales, very large computational grids are required an therefore is currently impractical for many engineering problems.

Numerical methods used to simulate the RANS equations are not directly applicable to LES and DNS. Up-winding schemes are used for many RANS schemes, which increases numerical robustness. However, when applied to DNS and LES calculations, up-winding results in numerical dissipation which compromises accuracy [16]. As Reynolds number increases, not using up-winding (such as in a straight-forward non-dissipative central-difference scheme) can lead to numerical instabilities.

Simulating high Reynolds-number flows using LES and DNS requires conservation of not just first-order quantities but also of the kinetic energy. Discrete energy conservation ensures that the flux of kinetic energy ($\sum_{\text{cvs}} u_j \partial(u_i u_j)/\partial x_j$) only has contributions from the boundaries, giving robustness without resorting to up-winding. For *structured* grids, the Harlow-Welch algorithm [17] ensures kinetic energy conservation. A numerical

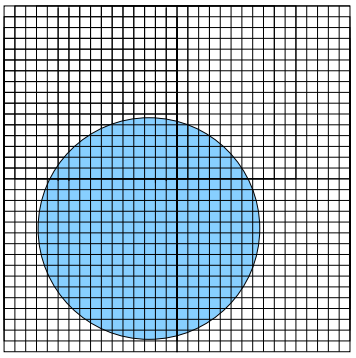

FIGURE 1.3: Schematic of the computational grid of a free-surface DNS simulation. The small flow scales around the bubble (blue) and the bubble surface are fully resolved.

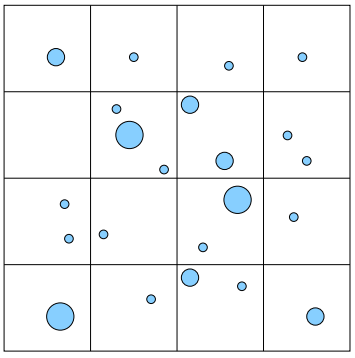

FIGURE 1.4: Schematic of the computational grid of an Euler-Lagrangian simulation, with the bubbles (blue) smaller than the computational mesh.

method that ensures kinetic energy conservation on *unstructured* grids is beneficial since meshes for complex geometries are more easily obtained than when using structured grids and can be created with fewer mesh elements, reducing the overall computational cost while retaining numerical accuracy. The numerical method developed by Mahesh et al. [18] conserves kinetic energy on unstructured grids and is used in the computational models described in this thesis. This work presents three numerical formulations to simulate bubbly flow, including an axisymmetric free-surface algorithm, the force coupling method, and a one-way coupled Euler-Lagrangian approach. The numerical details and validation of these approaches is included, though the focus of this work is the Euler-Lagrangian approach since it is most easily extended to large-scale problems with large numbers of bubbles.

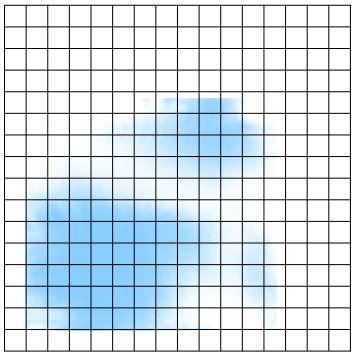

FIGURE 1.5: Schematic of the computational grid of an Euler-Euler simulation, with the bubble phase (blue) and carrier-phase (white) both described by continuum equations.

1.3 Review of past work

There have been many attempts to perform simulations of bubbly flows, ranging from *DNS with front-tracking*, where the bubble surface is described by marker points and an interpolated surface connecting the marker points (Fig. 1.3), *Euler-Lagrangian*, where bubbles are modeled as individual, spherical particles with bubble transport solved from a bubble equation of motion (Fig. 1.4) and *Euler-Euler*, where the multiple phases are modeled as a continuum (Fig. 1.5). The emphasis of this work is on high-fidelity numerical methods that simulate physics down to the bubble level and in-depth review of Euler-Euler approaches will not be addressed.

Performing DNS of the flow field such that all details, including the flow around the bubble and also the bubble surface, are resolved is advantageous in that minimal assumptions of the flow are required. Various methods using front-tracking DNS of the bubble and surrounding fluid have been proposed [19–23]. Recently, Lu et al. [24] performed DNS simulations of 16 bubbles in a turbulent channel at a Reynolds number of $\mathrm{Re}_\tau = 135$, with bubbles that are 54 wall units in diameter. All flow scales including the bubbles and the surrounding flow were resolved. Methods that perform DNS of the entire bubble and surrounding flow are important for discovering the detailed physics at the bubble level, however large-scale simulations of bubbly flows with thousands or

millions of bubbles are impractical using this approach due to the large computational requirements.

Performing RANS simulations of bubbly and cavitating flows has limitations, due to two factors. First, Lagrangian particles traveling in a time-averaged flow (such as that generated by a RANS solution) will not follow the same path as if they followed a path determined by the instantaneous field. Therefore, using a RANS flow field for Lagrangian simulations is not desirable. Another issue comes from the nature of coherent fluid structures. The meandering of a vortex element will contribute to the velocity fluctuations when the flow field is broken into the RANS formulation $u_i = \langle u_i \rangle + u_i'$. In a typical RANS formulation, this contributes to the turbulent kinetic energy fluctuations and will artificially increase the dissipation through turbulent viscosity, leading to an erroneous flow field. Over-dissipation in the tip-vortex region was observed in RANS simulations of propulsors [25, 26]. However, with increased resolution and by turning off the turbulence models, Dacles-Mariani et al. [25] were able to match experimental measurements in the wake region of the propulsor. In an attempt to remedy this problem, Hsiao and Chahine [27] and Hsiao and Chahine [28] performed RANS simulations with a small section of the domain downstream of the blade tips resolved using a finer mesh without turbulence models. This improved resolution of the tip vortex and improved prediction of cavitation inception index and inception location. With the improvement of LES formulations, it is more desirable to resolve the entire flow using LES so the unsteadiness of the flow field, along with resolution of unsteady, coherent structures is obtained, thus improving reliability of Lagrangian simulations of bubbly and cavitating flows.

Recently, Shams et al. [29] developed a two-way coupled Euler-Lagrange approach to simulate cavitating flows using DNS/LES on unstructured grids. The Rayleigh-Plesset (RP) equation was used to determine the behavior of the bubble radius, but did not account for bubble coalescence or breakup. Shams et al. [29] performed a simulation of turbulent flow over a cavity, with conditions similar to the experiment by Liu and Katz [3]. In the simulations, cavitation was observed near the trailing edge of the cavity, where cavitation was first observed in the Liu and Katz [3] experiment. Direct comparison of results is limited due to the qualitative results of bubble data provided by Liu and

Katz [3], but the Euler-Lagrange approach is promising since qualitative agreement was observed between simulation and experiment.

1.4 Overview

The primary objective of this work is to provide direct numerical simulation (DNS) and large-eddy simulation (LES) of cavitating bubbly flow. The following are the principal contributions of this work:

- A one-way coupled Euler-Lagrange approach has been developed for unstructured grids using parallel processing to enable large-scale simulations of flows with complex geometries.
  - The Rayleigh-Plesset (RP) equation is solved for the bubble radius over time, providing the coupling of the bubble size with the pressure field of the carrier fluid. Adaptive time-stepping is used to accurately and efficiently solve the RP equation over time.
  - Bubble collisions and coalescence are accounted for without resorting to RANS-type turbulence models or stochastic approximations for bubble-bubble collisions. Bubble-bubble collisions are computed directly using hard-sphere approach. A bubble coalescence model is developed that determines the probability of coalescence stochastically, with bubble-bubble collisions and the relative velocity between colliding bubbles computed directly.
- The Euler-Lagrangian approach has been applied to three problems: i) bubble migration in a turbulent boundary layer, ii) bubble coalescence in a turbulent pipe flow and iii) turbulent cavitating flow over a cavity.
  - Bubble migration in a turbulent boundary layer
    - After injection, bubbles move away from the wall as they travel downstream with the flow. The mechanism for the bubble dispersion was determined to be due to the fluid-acceleration term in the bubble equation of motion.

  - The mean bubble diffusion is compared to Sanders et al. [2] and the passive scalar diffusion results given by Poreh and Cermak [30]. The mean diffusion profiles are found to be similar between bubbles and a passive scalar, except near injection.
  - Bubble concentration profiles are compared to scalar concentration profiles of Poreh and Cermak [30]. Except very near the wall, the concentration profiles are similar to that of a passive scalar.

- Bubble coalescence in a turbulent pipe flow in microgravity
  - The downstream evolution of the PDF of bubble size was determined to be accurately predicted using the hard-sphere collision model and proposed coalescence model when compared to Colin et al. [1].
  - Statistics of collision parameters were obtained. Number density and number of collisions greatly decreases with downstream distance due to coalescence. The average probability of coalescence (once a collision occurs) decreases with downstream distance due to an increase in bubble size.

- Turbulent cavitating flow over a cavity
  - At a Reynolds numbers an order of magnitude lower than Liu and Katz [3], cavitation inception was inhibited as compared to experiment. However, as the cavitation number is decreased, cavitation was first observed at the cavity trailing edge and subsequently in the vortex cores as the cavitation index was lowered.
  - LES at the experimental Reynolds number of the Liu and Katz [3] was performed. Cavitation was observed for cavitation numbers similar to experiment. Decreasing the size of gas nuclei in the flow reduced the prevalence of cavitation.

Chapter 2

Numerical Methods

In this chapter, three different numerical methods that have been developed and implemented over the course of this work are described and validated. These include i) an axisymmetric Navier-Stokes solver with a free surface, ii) the force coupling method and iii) the one-way coupled Euler-Lagrangian approach. The free surface method resolves the flow near the bubble and also the bubble surface, allowing simulation of complex bubble deformation. However this method is very expensive computationally. The force-coupling method approximately resolves the flow around each bubble, which are treated as discrete Lagrangian elements. For flows with large numbers of bubbles, this method is also expensive since $\sim 4-6$ grid points are required to resolve the bubble diameter. The one-way coupled Euler-Lagrangian approach is much more computationally efficient per bubble, since there is no requirement for grid resolution as long as the turbulent carrier-phase is resolved. For the simulations of turbulent flow with large numbers of bubbles described in later in this thesis (Chapters 4-**??**), the one-way coupled Euler-Lagrangian approach has been used because of its computational efficiency.

2.1 Free-surface axisymmetric Navier-Stokes approach

An axisymmetric Navier-Stokes solver with a free-surface algorithm has been developed, based on the numerical method by Popinet and Zaleski [23]. The bubble interface is

represented by a cubic spline interpolated between marker cells, giving the capability to accurately solve for bubble surface deformation over time.

In this approach, the Navier-Stokes simulations are solved along with free-surface boundary conditions. This approach has been adapted from the method proposed by Popinet and Zaleski [23]. This method is simple, yet powerful enough to simulate bubble collapse near a wall, which cannot be accurately modeled without explicitly modeling the deformation of the interface. The Navier-Stokes equations are simplified by assuming an axisymmetric flow and solved on a staggered (MAC), $i-j$ ordered grid (See Figure 2.1).

2.1.1 Numerical details

The incompressible, axisymmetric Navier-Stokes equations are given by

$$\frac{1}{r}\frac{\partial(ru_r)}{\partial r} + \frac{\partial u_z}{\partial z} = 0, \tag{2.1}$$

$$\frac{\partial u_r}{\partial t} + \frac{1}{r}\frac{\partial(ru_r^2)}{\partial r} + \frac{\partial(u_r u_z)}{\partial z} = -\frac{\partial \phi}{\partial r} + \frac{1}{r}\frac{\partial(rS_{rr})}{\partial r} + \frac{\partial S_{zr}}{\partial z} - \frac{S_{\theta\theta}}{r}, \tag{2.2}$$

$$\frac{\partial u_z}{\partial t} + \frac{1}{r}\frac{\partial(ru_r u_z)}{\partial r} + \frac{\partial(u_z^2)}{\partial z} = -\frac{\partial \phi}{\partial z} + \frac{1}{r}\frac{\partial(rS_{zr})}{\partial r} + \frac{\partial S_{zz}}{\partial z}, \tag{2.3}$$

where $\phi = p/\rho_\mathrm{f}$ and the components of the stress tensor S are defined as

$$S_{rr} = 2\nu_\mathrm{f}\frac{\partial u_r}{\partial r}, \tag{2.4}$$

$$S_{\theta\theta} = 2\nu_\mathrm{f}\frac{u_r}{r}, \tag{2.5}$$

$$S_{zz} = 2\nu_\mathrm{f}\frac{\partial u_z}{\partial z}, \tag{2.6}$$

$$S_{zr} = S_{rz} = \nu_\mathrm{f}\left(\frac{\partial u_z}{\partial r} + \frac{\partial u_r}{\partial z}\right), \tag{2.7}$$

where ν_f is the kinematic viscosity of the fluid.

The axisymmetric Navier-Stokes equations are integrated using a finite-volume formulation over a moving domain. The domain (portion of the control volume occupied by the fluid) is defined as Ω and the boundary of this domain is $\partial\Omega$. The velocity of the

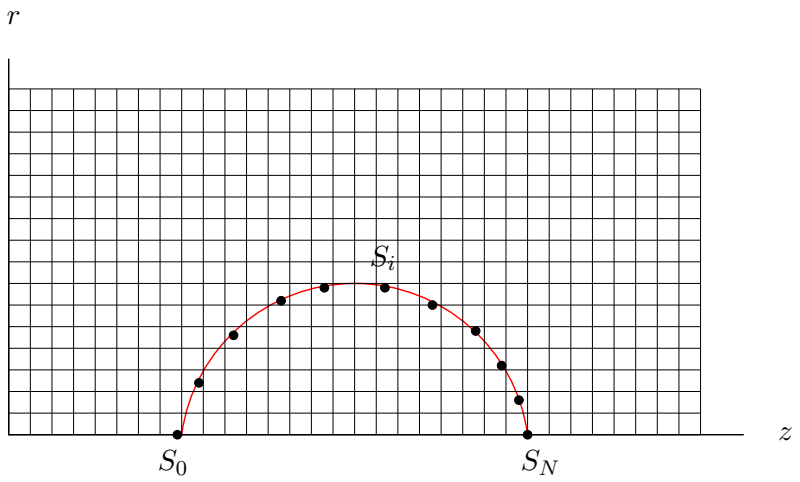

FIGURE 2.1: Schematic of grid and bubble interface of the axisymmetric Navier-Stokes solver. The bubble interface is described by N marker points located at position S_i.

boundary $\partial\Omega$ is defined as $\hat{u}_i$. Integrating over Ω gives the integral equations

$$\frac{\partial}{\partial t}\int_\Omega r \,\mathrm{d}r\,\mathrm{d}z + \int_{\partial\Omega} r(u_z - \hat{u}_z)\,\mathrm{d}r - \int_{\partial\Omega} r(u_r - \hat{u}_r)\,\mathrm{d}z = 0 \tag{2.8}$$

$$\begin{aligned}\frac{\partial}{\partial t}\int_\Omega u_r r \,\mathrm{d}r\,\mathrm{d}z + \int_{\partial\Omega} r u_r(u_z - \hat{u}_z)\,\mathrm{d}r - \int_{\partial\Omega} r u_r(u_r - \hat{u}_r)\,\mathrm{d}z = \\ \int_{\partial\Omega}\phi r\,\mathrm{d}z + \int_\Omega \phi\,\mathrm{d}r\,\mathrm{d}z + \int_{\partial\Omega} r S_{zr}\,\mathrm{d}r - \int_{\partial\Omega} r S_{rr}\,\mathrm{d}z - \int_\Omega S_{\theta\theta}\,\mathrm{d}r\,\mathrm{d}z,\end{aligned} \tag{2.9}$$

$$\begin{aligned}\frac{\partial}{\partial t}\int_\Omega u_z r \,\mathrm{d}r\,\mathrm{d}z + \int_{\partial\Omega} r u_z(u_z - \hat{u}_z)\,\mathrm{d}r - \int_{\partial\Omega} r u_z(u_r - \hat{u}_r)\,\mathrm{d}z = \\ \int_{\partial\Omega}\phi r\,\mathrm{d}r + \int_{\partial\Omega} r S_{zz}\,\mathrm{d}r - \int_{\partial\Omega} r S_{zr}\,\mathrm{d}z.\end{aligned} \tag{2.10}$$

The grid is staggered and in a structured format (i, j ordered). Let us consider a control volume with the free-surface interface $\partial\Omega$ intersecting with a control volume of u_r. The domain of integration Ω is the portion of the control volume occupied by the fluid, bounded by $ABCDEA$ (Figure 2.2). The velocity $\hat{u}_i$ is 0 on $AB \cup BC \cup DE \cup EA$ and equal to the fluid velocity u_i on CD. Using this formulation, Eqn. 2.9 can then be

written as

$$\begin{aligned}\frac{\partial}{\partial t}\int_\Omega u_r r \,\mathrm{d}r\,\mathrm{d}z + \int_{BC\cup EA} r u_r u_z \,\mathrm{d}r - \int_{AB\cup DE} r u_r^2 \,\mathrm{d}z \\ = \int_{AB\cup DE} \phi r \,\mathrm{d}z + \int_{CD} \phi r \,\mathrm{d}z + \int_\Omega \phi \,\mathrm{d}r\,\mathrm{d}z \\ + \int_{BC\cup EA} r S_{zr} \,\mathrm{d}r + \int_{CD} r S_{zr} \,\mathrm{d}r \\ - \int_{AB\cup DE} r S_{rr} \,\mathrm{d}z - \int_{CD} r S_{rr} \,\mathrm{d}z - \int_\Omega S_{\theta\theta} \,\mathrm{d}r\,\mathrm{d}z. \end{aligned} \tag{2.11}$$

A similar discretization is used for the formulation of Eqn. 2.10. If the control volume is not cut by the interface, the equations reduce to the single-phase discretization. A projection method is used to advance the equations in time through enforcing incompressibility. The equations are first advanced without the pressure terms (though the integral contribution of pressure along the interface is included). Since the velocity field at the next timestep $(k+1)$ is incompressible, the Poisson-like equation for pressure can then be solved using a Gauss-Seidel relaxation approach.

The interface is discretized using a set of marker points connected by a cubic spline. Since the location of the interface is explicitly known, all information about the local curvature is known and the surface integral terms in Eqns. 2.9 and 2.10 are explicitly defined. The pressure on the fluid side of the interface is defined by the stress boundary condition

$$p = p_b + \sigma\kappa + \mu_\mathrm{f}\, \vec{n} \cdot \vec{\vec{D}} \cdot \vec{n}, \tag{2.12}$$

where p_b is the pressure inside the bubble, σ is the surface tension coefficient, $\vec{n}$ is the interface normal vector, κ is the curvature of the interface, μ_f is the fluid dynamic viscosity and $\vec{\vec{D}}$ is the deviatory part of the stress tensor.

Velocities inside the interface must be interpolated in order to obtain velocity values at the interface. The velocity field on the interface must also satisfy the zero-tangential stress condition

$$\vec{t} \cdot \vec{\vec{D}} \cdot \vec{n}, \tag{2.13}$$

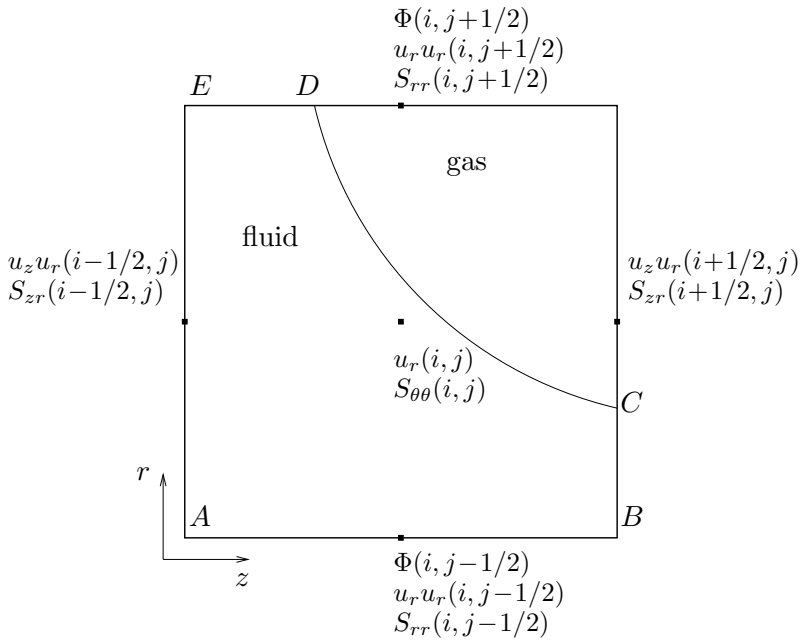

FIGURE 2.2: Control volume discretization of free-surface Navier-Stokes equations for u_r.

where $\vec{t}$ is the tangential vector to the surface. The velocity field at some point P on the interface can be described as $\vec{v} = \vec{v}_o + \vec{\vec{A}} \cdot \vec{x}$ where $\vec{x}$ is the position vector, $\vec{\vec{A}}$ is a 2×2 matrix and $\vec{u}_o$ a yet-to-be-determined velocity. With this definition of velocity on the surface, Eqn. 2.13 can be written as $e_{ij} t_i n_j = 0$ with

$$e_{ij} \equiv \frac{\partial u_i}{\partial x_j} + \frac{\partial u_j}{\partial x_i} = A_{ij} + A_{ji}. \tag{2.14}$$

With an N number of points about point P, the vector $\vec{u}_o$ and matrix A_{ij} can be obtained through minimizing the function

$$F = \sum_{n=1}^{N} \left(\vec{u}_o + \vec{\vec{A}} \cdot \vec{x}_n - \vec{u}_n \right)^2 - \lambda e_{ij} t_i n_j, \tag{2.15}$$

where λ is a Lagrange multiplier. The marker points on the interface are advanced using bilinear interpolation for the velocity field every timestep. The average distribution of marker points is on the order of the grid size. Marker points terminating the interface

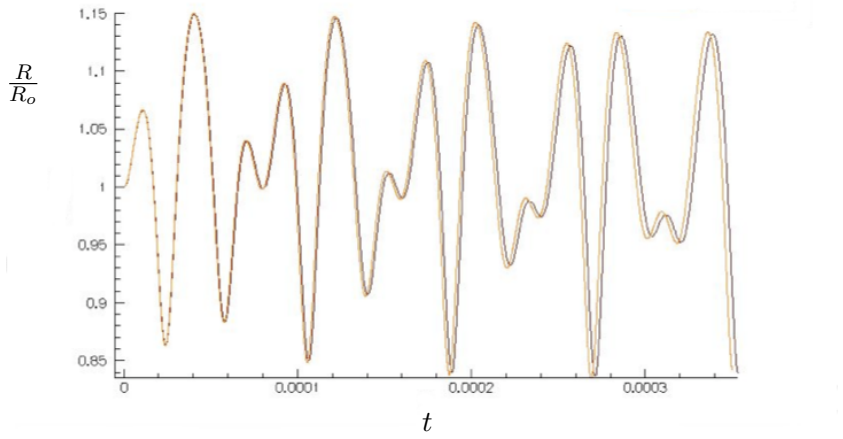

FIGURE 2.3: Bubble oscillation (R/R_o versus t) in a sinusoidally-varying pressure field. —, free-surface Navier-Stokes; —, Rayleigh-Plesset.

are placed on the $r = 0$ axis and are only able to move in the z-direction. The pressure inside the bubble is obtained using a poly-tropic relation

$$p_b(R) = p_\infty \left(\frac{R_o}{R}\right)^{3\gamma}, \tag{2.16}$$

where R is the equivalent radius of the bubble (or radius of a sphere that has an equal volume), p_∞ is the far-field pressure, γ is the ideal gas constant ($\gamma = 1.4$) for air and R_o is the equilibrium radius.

2.1.2 Validation

2.1.2.1 Bubble oscillation in a sinusoidal acoustic field

The free-surface axisymmetric Navier-Stokes solver is used to perform a simulation of a forced oscillation of a gas bubble in water with a far-field sinusoidal pressure variation. The initial bubble radius radius $R_o = 89$ μm and the bubble is initialized at equilibrium, with an initial far-field pressure of $P_\infty = 101.3$kPa. The surface tension coefficient

$\sigma = 0.07$ N/m. The initial bubble pressure $p_\mathrm{b} = p_\infty + 2\sigma/R_o = 102.9$ kPa. The fluid density $\rho_\mathrm{f} = 1000$ kg/m^3 and the fluid dynamic viscosity $\mu_\mathrm{f} = 0.001$ N $\cdot$ s/m^3.

The confinement ratio C is the ratio of the domain size to the diameter of the bubble. The confinement ratio is equal to 12.5, with the domain length in the z-direction equal to twice the length in the r-direction. The center of the bubble is initialized at $z = L_z/2$ and $r = 0$. A uniform grid spacing is used with number of grid points in the z and r directions equal to 1024 and 512 respectively for a total of $524,288$ control volumes.

A sinusoidal pressure variation is applied at the domain boundaries, with the mean pressure equal to P_∞ and an amplitude of $P_\mathrm{amp} = 21.3$kPa. The frequency of pressure variation is 24.2kHz. The bubble behaves erratically, due to the non-linearity of the bubble physics. The bubble remains spherical because the surrounding pressure field is uniform. Figure 2.3 plots variation of bubble radius over time. Good agreement with the Rayleigh-Plesset equation is obtained.

2.1.2.2 Bubble collapse near wall

When a bubble collapses near a wall, the symmetry of the flow around the bubble is broken and the bubble no longer retains a spherical shape throughout collapse and rebound. The constriction of the flow causes a jet to form on the top side (opposite to the wall) of the bubble that may penetrate the bubble and create a high-pressure impact at the wall. The axisymmetric free-surface Navier-Stokes solver is used to simulate this problem and results are compared to simulations by Popinet and Zaleski [23].

The ratio of initial bubble radius to equilibrium bubble radius is defined as $\alpha = R_o/R_\mathrm{eq}$. The Reynolds number is defined as $\mathrm{Re} = \frac{1}{\nu^*}$, with $\nu^* = \frac{\nu_\mathrm{f}}{R_o}\sqrt{\frac{\rho_\mathrm{f}}{p_\infty}}$. The relative distance of the bubble center from the wall is defined by the parameter $\beta = H/R_o$, where H is the initial height of the bubble centroid from the wall. The effect of surface tension is ignored ($\sigma = 0$), where for a 5 μm bubble in pure water the non-dimensional surface tension parameter $\sigma^* = \sigma/(R_o p_\infty) \sim 0.014$, which is very small. For this simulation, $\alpha = 2.023, \mathrm{Re} = 18.4$ and $\beta = 2.625$. The initial bubble radius $R_o = 10$ μm. The

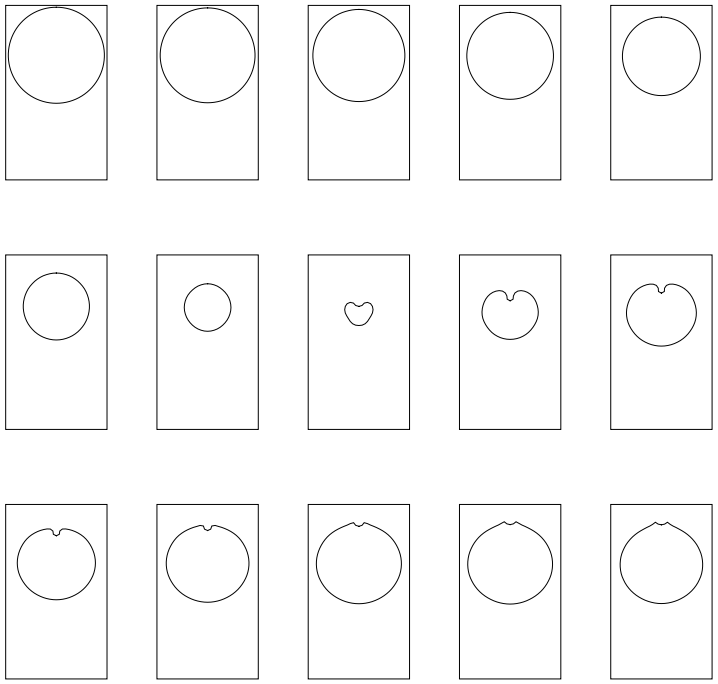

FIGURE 2.4: Evolution of bubble collapsing near a wall at Re = 18.4. Wall is along the bottom of each box. Time between each frame is 0.634 non-dimensional units of time, based on a timescale of $\sqrt{\rho_f R_o^2/p_\infty}$.

confinement ratio $C = 10$, with a uniform grid of $N_z = N_r = 130$. The boundary pressure $p_\infty = 3390.4$ Pa.

Figure 2.4 plots the evolution of the bubble surface over time. The wall is given by the bottom of each frame. As the bubble collapses, a fluid jet forms which penetrates the top of the bubble. As the bubble expands after collapse, the jet recedes from the interface. Good agreement is obtained with simulation results by Popinet and Zaleski [23], whose results are shown in Figure 2.5.

2.1.3 Comments

Using this approach, an axisymmetric solution to the Navier-Stokes equations with a free-surface is obtained over time for a single bubble. However, since the entire flow surrounding the bubble along with complete resolution of the free-surface is required, simulations using this approach are relatively expensive. Therefore, this approach cannot be

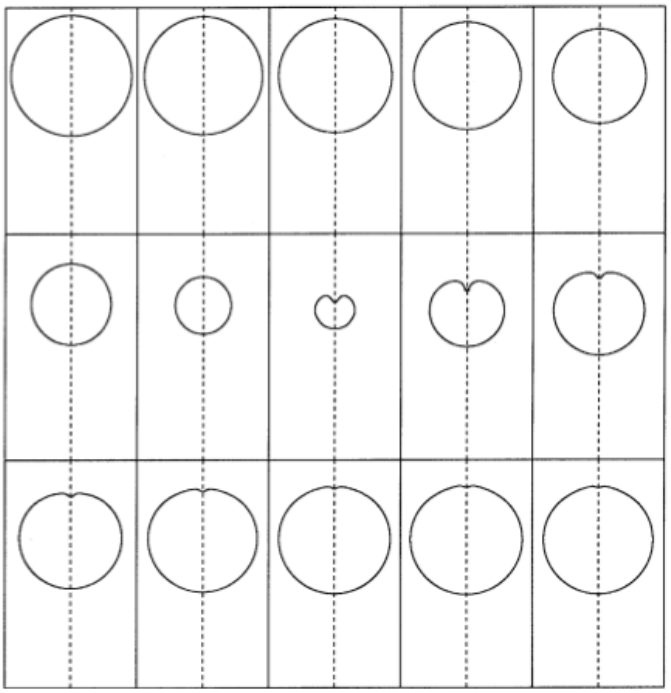

FIGURE 2.5: Evolution of bubble collapsing near a wall at Re = 18.4 for the Popinet and Zaleski [23] simulation. Wall is along the bottom of each box.

used for simulations with large numbers of bubbles with today's available computational resources. Other, less expensive approaches must be used.

2.2 Force coupling method

2.2.1 Numerical approach

An alternative to the Navier-stokes solver with free-surface conditions and the one-way coupled Euler-Lagrangian approach is the approximate force coupling method (FCM). The approach is an Euler-Lagrangian formulation that includes two-way coupling without resolving the smallest scales of the flow near the bubbles, as required in the above free-surface approach and has been developed and tested recently [31–35]. Resolving the bubble interface becomes computationally expensive as the number of bubbles simulated increases and is currently not feasible with current computational resources. The

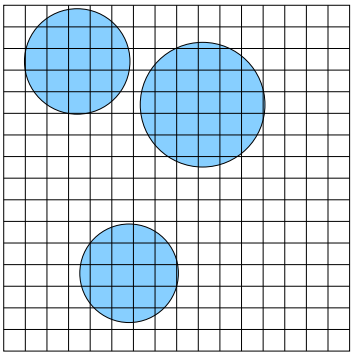

FIGURE 2.6: Schematic of the computational grid of an FCM simulation, with each bubble represented by a discrete Lagrangian element that is resolved by ~ 5 grid points across the diameter.

FCM approach requires only about 4-6 grid points per bubble diameter on a uniform grid [35], though the bubble radius is assumed constant. The bubbly flow is modeled as a dispersed phase, with individual bubbles treated as point particles governed by an equation for bubble motion, combined with a continuous carrier phase described by DNS / LES Navier-Stokes equations. To solve the Navier-Stokes equations for the continuous phase, the finite-volume approach by Mahesh et al. [18] is used. The discretization of this approach is described in Chapter 2.3.1. Each bubble is tracked individually and is characterized by its instantaneous position, velocity and size.

Considering N spherical particles, the coupling is implemented as a source term in the momentum equation. The force and/or torque exerted by each bubble on the carrier phase can be described by a force mono-pole (F_i) and a force dipole (F_{ij}) and act as an equal and opposite force and/or torque on the bubble itself. The entire domain, including the volume occupied by the particles, is considered an incompressible fluid governed by

$$\frac{\partial u_i}{\partial x_i} = 0, \tag{2.17}$$

$$\rho_\mathrm{f}\left(\frac{\partial u_i}{\partial t} + u_j\frac{\partial u_i}{\partial x_j}\right) = \frac{\partial p}{\partial x_i} + \mu_\mathrm{f}\frac{\partial^2 u_i}{\partial x_j \partial x_j} + \sum_{n=1}^{N}\left[F_i^n \Delta_m(\vec{x}-\vec{Y}^n) + F_{ij}^n\frac{\partial \Delta_d(\vec{x}-\vec{Y}^n)}{\partial x_i}\right]. \tag{2.18}$$

The fluid velocity is denoted by $\vec{u}$, fluid density ρ_{f}, fluid pressure p and fluid dynamic viscosity by μ_{f}. The summation term is the force on the fluid due to each bubble n over for N total bubbles, written as a force mono-pole and dipole. As a first approximation, fluid torque and strain acting from the fluid on the bubble are ignored and the force dipole term is neglected. The force mono-pole term is integrated over the entire domain over N bubbles and normalized by the Gaussian envelope function for bubble n:

$$\Delta_m(\vec{x} - \vec{Y}^n) = \frac{1}{(2\pi\sigma_{\mathrm{m}}^2)^{3/2}} \times \exp\left(-\frac{(x_i - Y_i^n)(x_i - Y_i^n)}{2\sigma_{\mathrm{m}}^2}\right), \tag{2.19}$$

which decreases exponentially as the distance from the bubble centroid $\left|\vec{x} - \vec{Y}^n\right|$ increases. The Gaussian term (σ_{m}) is related to the bubble radius by

$$\sigma_{\mathrm{m}} = \frac{R}{\sqrt{\pi}} \approx \frac{R}{1.77}. \tag{2.20}$$

The force mono-pole is equal and opposite to the body force from the fluid applied to the bubble. In general, this force is

$$F_i^n = V_b(\rho_b - \rho_f)\left(g_i - \frac{\mathrm{d}V_i^n}{\mathrm{d}t}\right), \tag{2.21}$$

where V_b is the bubble volume, ρ_b the bubble density, ρ_f the fluid-phase density and $\vec{g}$ the gravitational acceleration. For this paper, it is assumed that buoyancy dominates the inertial forces and only the gravity term is included. The bubble velocity $\vec{V}^n$ is obtained through localized averaging of the fluid velocity and given by

$$V_i^n(t) = \int u_i(\vec{x}, t)\,\Delta\left(\vec{x} - \vec{Y}^n\right) d^3\vec{x}. \tag{2.22}$$

The formulation for the length scale σ_m (Eqn. 2.20) is obtained by matching the terminal rise velocity of a bubble from simulation with the steady-state Stokes result. For both the bubble velocities and force mono-pole, the Gaussian envelope function is integrated over the entire domain. The fluid equations are advanced in time as described by Chap. 2.3.1. A 2nd-order Adams-Bashforth time integrator is used to advance the bubble position in time. The bubble position is integrated every fluid timestep.

TABLE 2.1: Experimental values

Case	ρ_f(g/cm^3)	ρ_p(g/cm^3)	$\theta(^\circ)$	ν(mm^2/s)
1	1.115	1.081	8.23	3.125

TABLE 2.2: Domain parameters

Case	$L_x \times L_y \times L_z$	$N_x \times N_y \times N_z$
1	$10 \times 1 \times 4$	$512 \times 48 \times 96$

TABLE 2.3: Non-dimensional parameters

Case	$\mathrm{Re}_f = L_y U_o/\nu$	$\mathrm{Fr} = \lvert g \rvert L_y/{U_o}^2$	Re_p^S
1	32.0	982.0	13.6

2.2.2 Validation: Single sphere rising in an inclined channel

The force coupling method is validated with the simulation of a single solid sphere rising in an inclined channel. A corresponding experiment was performed by Lomholt et al. [35], with a setup composed of a rectangular channel with height $L_x = 150$ mm, width $L_y = 10$ mm and depth $L_z = 100$ mm. A single particle is released near the center of the channel. The channel is rotated from vertical (about the z-axis) by an angle θ. A mixture of glycerol and water was used for the fluid to achieve the desired fluid properties. The particles were polyamide spheres with a uniform density and size. The particle has a constant radius $R/L_y = 0.1$. Tables 2.1, 2.2 and 2.3 show the physical and computational parameters used.

The computational grid is uniform and has N_x, N_y and N_z control volumes in each respective spatial dimension. The grid is periodic in the spanwise and streamwise directions. Increasing mesh resolution or reducing timestep was observed to have no effect on the simulation results. The Reynolds number scaling based on the Stokes setting velocity W is defined as

$$\mathrm{Re}_p^S = \frac{2RW}{\nu} = \frac{2R}{\nu}\left|\frac{2R^2}{9\mu}\left(\rho_p - \rho_f\right)g\right| = \frac{4R^3}{9\nu^2}\left|\frac{\rho_p}{\rho_f} - 1\right| g.$$

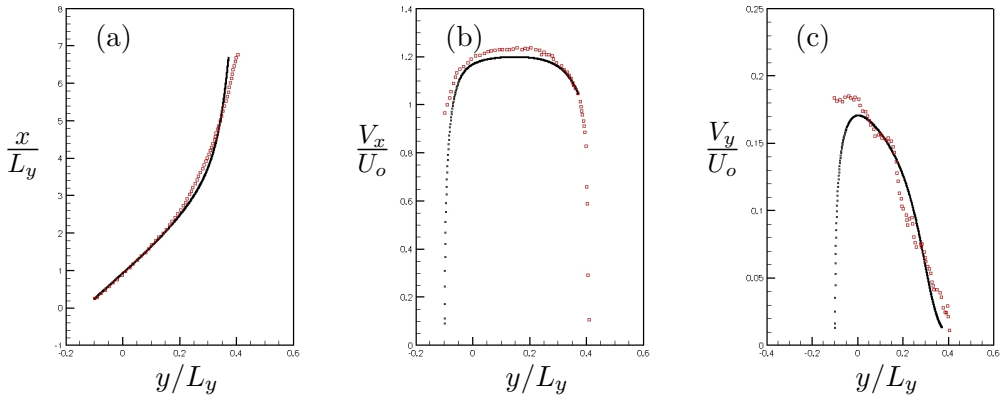

FIGURE 2.7: Comparison of bubble trajectories and velocities with experiment. The simulation quantities are represented by small black squares (■) and experimental quantities are represented by red squares (□). Figure (a) plots the advance of the particle position, while figures (b) and (c) plot the particle streamwise and stream-normal velocities vs. y-position, respectively.

Figure 2.7 compares the computational results to experiment. Computational results are depicted with small black squares and experimental results with red squares. Figure 2.7a plots the streamwise particle position versus wall-normal position, while Figures 2.7b and 2.7c plot the streamwise and wall-normal particle velocities, respectively.

The experimental and computational results show fair agreement. Due to buoyancy, the particle initially ($y/L_y < 0.2$) moves in the direction of the gravitational acceleration. For $y/L_y < 0.2$, the computed particle follows the experimental trajectory, although the streamwise velocity is somewhat lower. As the particle approaches the wall, the rise velocity decreases. Here the computed wall-normal velocity is first higher, then lower, than the experimental values. This results in the slight trajectory differences. As the particle continues to approach the wall ($y/L_y > 0.2$), both the streamwise and wall-normal velocities decrease. Eventually, the particle comes to rest as it contacts the wall. Including dipole forces in the force coupling method formulation would better resolve the fluid stresses as the particle nears the wall and lead to more accurate results[35]. As a first approximation, the mono-pole force coupling method is reasonably accurate.

2.2.3 Comments

The force coupling method efficiently models the two-way coupling between the bubble and the fluid. Since only $\sim 4-6$ grid points are required in the region of the bubble, the FCM approach is more effective in simulating large numbers of bubbles than the free-surface Navier-Stokes approach. However, more computational resources are required for FCM as compared to the one-way coupled Euler-Lagrangian method, since the flow around the bubble still must be approximately resolved, which is not required in the one-way coupled formulation. For example, for a simulation of $\sim$ 3000 bubbles in a turbulent channel flow ($\mathrm{Re}_\tau = 180$) on a grid with 3.5×10^6 control volumes performed $\sim$ 500 time-steps per hour on 256 processors [36]. Conversely, the Euler-Lagrangian code is more efficient per bubble injected, where for a simulation of $\sim 33,000$ bubbles in a turbulent boundary layer [37] on a large grid of 53×10^6 control volumes was able to simulate $\sim$ 350 time-steps per hour on 992 processors of similar speed as the FCM simulation.

2.3 One-way coupled Euler-Lagrangian approach

In the one-way coupled Euler-Lagrangian framework, the bubbles are modeled as a dispersed phase, with individual bubbles treated as point-particles governed by an equation for bubble motion, combined with a continuous carrier phase described by the DNS / LES Navier-Stokes equations (See Figure 2.8). To solve the Navier-Stokes equations for the continuous phase, a finite-volume approach for unstructured grids [18] is used. The following section describes the algorithm details of Mahesh et al. [18] to solve the Navier-Stokes equations on unstructured grids.

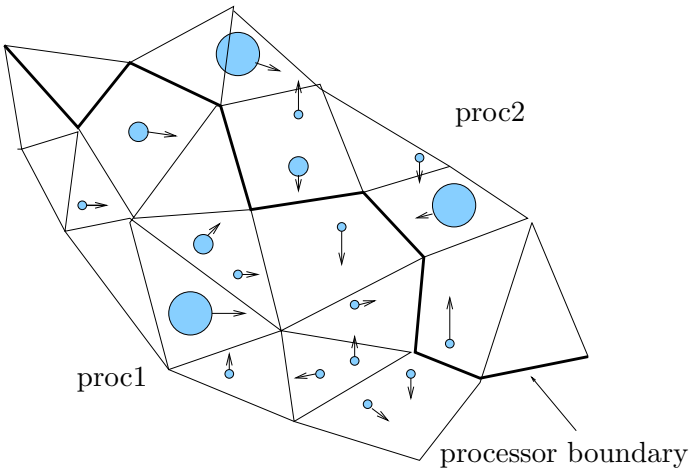

FIGURE 2.8: Schematic of Lagrangian bubbles (blue spheres) distributed throughout the unstructured domain between two processors on a two-dimensional grid. Vectors denote instantaneous velocity of discrete bubble. The thick line represents the inter-processor boundary of processors 1 and 2.

2.3.1 Carrier-phase solver

The continuum of fluid surrounding the bubbles is described by the single-phase, incompressible Navier-Stokes equations:

$$\frac{\partial u_i}{\partial x_i} = 0, \tag{2.23}$$

$$\frac{\partial u_i}{\partial t} + \frac{\partial u_i u_j}{\partial x_j} = -\frac{\partial p}{\partial x_j} + \nu_\mathrm{f} \frac{\partial^2 u_i}{\partial x_j x_j}, \tag{2.24}$$

where u_i is the Cartesian fluid velocity at the control volume centers, p is the fluid pressure and ν_f the fluid viscosity. The density of the fluid (ρ_f) is assumed constant and is absorbed into the pressure variable.

This algorithm assumes constant density of the carrier phase and solves the incompressible Navier-Stokes equations using a predictor-corrector approach. The predictor velocities are obtained by advancing the solution without the pressure terms

$$\frac{\hat{u}_i - u_i^k}{\Delta t} = \frac{1}{2}\left(3(\mathrm{NL} + \mathrm{VISC})^k - (\mathrm{NL} - \mathrm{VISC})^{k-1}\right], \tag{2.25}$$

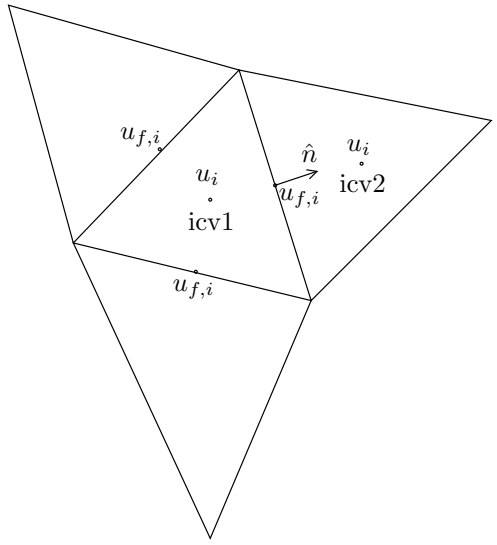

FIGURE 2.9: Discretization of control volume and face-normal velocities (u_i and $u_{f,i}$, respectively). u_i is located at the control volume centroid and $u_{f,i}$ is located at the face centroid. The face-normal vector $\hat{n}$ points from icv1 to icv2.

where NL and VISC denote the non-linear and viscous terms, respectively. The predicted values of velocity are used to obtain the predicted face-normal velocities,

$$\hat{u}_{f,i} = \left(\frac{\hat{u}_i^{\text{icv1}} + \hat{u}_i^{\text{icv2}}}{2} \right) n_i, \tag{2.26}$$

where n_i is the face-normal vector and therefor $u_{f,i}$ points from icv1 to icv2 (See Figure 2.9). The predicted face-normal velocities are obtained by projecting with the face-normal pressure-gradient included,

$$\frac{u_{f,i} - \hat{u}_{f,i}}{\Delta t} = \frac{\partial p}{\partial n}. \tag{2.27}$$

The face-normal pressure gradient is obtained so that the face-normal velocity field $u_{f,i}(\vec{x})$ is divergence-free to satisfy incompressibility. Once the face-normal pressure gradient is obtained, the control volume velocities are obtained by

$$\frac{u_i^{k+1} - \hat{u}_i}{\Delta t} = \frac{\partial p}{\partial x_i}. \tag{2.28}$$

However, the pressure gradient that is obtained should also discretely conserve kinetic energy, meaning that

$$\sum_{\text{faces of cv}} \left(\left.\frac{\partial p}{\partial x_i}\right|_{\text{icv}} - \left.\frac{\partial p}{\partial n}\right|_{\text{face}} \right) A_f \tag{2.29}$$

should be minimized to make the pressure-gradient term as energy-conserving as possible, where A_f is the area of the face.

2.3.2 Equations of bubble motion - constant bubble radius

Individual bubbles are modeled as point particles, with each bubble tracked individually and characterized by its position, velocity and size. Forces from the carrier fluid act upon the bubble and are applied to each bubble's center of mass. The bubble is assumed to be much smaller than the length scales of motion in the carrier phase and the bubbles are modeled as spherical nuclei. Assuming small bubble size and a dilute bubble concentration, the bubbles exert a negligible force on the carrier fluid or other bubbles. This is the one-way coupling regime. The bubble acceleration is equal to sum of the forces on the bubble. Assuming the bubble radius is constant over time, these forces are the drag, lift, fluid acceleration, buoyancy and added-mass forces, yielding [38–40]

$$m_{\text{b}} \frac{d\vec{v}}{dt} = \sum \vec{F} = \vec{F}_{\text{D}} + \vec{F}_{\text{L}} + \vec{F}_{\text{F}} + \vec{F}_{\text{B}} + \vec{F}_{\text{AM}}, \tag{2.30}$$

with m_{b} defined as the mass of the bubble and $\vec{v}$ as the bubble velocity. The forces on the bubble are described by the following equations:

$$\begin{aligned}
\vec{F}_{\text{D}} &= \frac{1}{2}\rho_{\text{f}} A_{\text{b}} C_{\text{D}} \left|\vec{u} - \vec{v}\right| (\vec{u} - \vec{v}) \\
\vec{F}_{\text{L}} &= m_{\text{f}} C_{\text{L}} (\vec{u} - \vec{v}) \times \vec{\omega} \\
\vec{F}_{\text{F}} &= m_{\text{f}} \frac{D\vec{u}}{Dt} \\
\vec{F}_{\text{B}} &= (m_{\text{b}} - m_{\text{f}})\, \vec{g} \\
\vec{F}_{\text{AM}} &= m_{\text{f}} C_{\text{M}} \left(\frac{D\vec{u}}{Dt} - \frac{d\vec{v}}{dt} \right),
\end{aligned}$$

where the carrier-phase velocity, $\vec{u}$, is interpolated to the bubble's instantaneous position and A_b is the area of a circle with radius R, the bubble radius. The carrier-phase density is ρ_f and the equivalent mass of a sphere with radius R and the density of the carrier-phase is m_f. Johnson and Hsieh [38] performed Lagrangian simulations of cavitating bubbles traveling around a blunt body and included the drag force with a drag coefficient determined by Haberman and Morton [41] and also the contribution of volume change of the bubble in time to the added mass force. Thomas et al. [39] included contributions due to lift, with a constant lift coefficient of 1/2. Auton et al. [40] showed that the constant lift coefficient of 1/2 is appropriate in the inviscid limit, and showed that for the forces due to added mass and fluid acceleration, the material derivative is the appropriate term for the fluid acceleration. A constant lift coefficient, C_L, of 1/2 and a constant added-mass coefficient, C_M, of 1/2 for a sphere are used [42, 43].

The material derivative of the fluid velocity, fluid velocity, pressure and fluid gradients are obtained at the bubble location ($\vec{Y}$) using a linear interpolation in space and time to the instantaneous bubble location. The expression for the coefficient of bubble drag, a function of bubble Reynolds number and determined experimentally by Haberman and Morton [41] is

$$C_\mathrm{D} = \frac{24}{\mathrm{Re}_\mathrm{b}}\left(1.0 + 0.197\mathrm{Re}_\mathrm{b}^{0.63} + 2.6\times10^{-4}\mathrm{Re}_\mathrm{b}^{1.38}\right), \tag{2.31}$$

where the bubble Reynolds number is defined as $\mathrm{Re}_\mathrm{b} = 2R\left|\vec{u}-\vec{v}\right|/\nu$. For small bubbles in water, the drag profile is similar to that of solid spheres ($C_\mathrm{D} \sim 24/\mathrm{Re}_\mathrm{b}$), due to the contamination by surfactants of the bubble surface.

Assuming that the density of gas is much less than that of water, the bubble mass m_b is much less than m_f and the sum of forces on a bubble is zero. After substituting the above expressions for bubble forces into Eqn. 2.30, the following expression is obtained for the time derivative of the bubble velocity:

$$\frac{d\vec{v}}{dt} = \underbrace{-2\vec{g}}_{\text{Buoyancy}} + \underbrace{3\frac{D\vec{u}}{Dt}}_{\text{Fluid material derivative}} + \underbrace{\frac{3}{4}\frac{C_\mathrm{D}}{R}\left|\vec{u}-\vec{v}\right|\left(\vec{u}-\vec{v}\right)}_{\text{Drag}} + \underbrace{2C_\mathrm{L}(\vec{u}-\vec{v})\times\vec{\omega}}_{\text{Lift}}. \tag{2.32}$$

2.3.3 Accounting for change in bubble size

Bubbles respond to pressure variations in the carrier flow by changing their size. In general, as the local pressure increases a bubble will shrink, and conversely, a bubble will grow as the pressure decreases. The physics of this growth are determined by the relative pressures inside and outside the bubble surface and surface tension. For small bubbles at small Weber numbers (We $\ll 1$), the bubbles will remain nearly spherical and an assumption of spherical bubbles is appropriate. A change of the bubble size will affect the bubble motion. The effects of an unsteady bubble radius on the drag and lift coefficients are not known. In this work, the effects of bubble size are determined simply by a change in bubble Reynolds number (though the drag and lift expressions remains constant), but an expression for the added-mass force can be generalized to account for a change of bubble size over time.

The added-mass force on a bubble is the time derivative of the fluid impulse [43], given by

$$\vec{F}_{\mathrm{AM}} = \frac{d}{dt}\left[\rho_{\mathrm{f}} C_{\mathrm{M}} V \left(\vec{u} - \vec{v}\right)\right], \tag{2.33}$$

and results in the form of the added-mass force in Eqn. 2.31 if the bubble volume V is equal to a constant of $4\pi R^3/3$. However, if the bubble volume is no longer constant, the added-mass force is due to a change in volume and in velocity over time (assuming density and added-mass coefficient remain constant). After applying the chain rule, we obtain

$$\vec{F}_{\mathrm{AM}} = \rho_{\mathrm{f}} C_{\mathrm{M}} V \frac{d}{dt}\left(\vec{u} - \vec{v}\right) + \rho_{\mathrm{f}} C_{\mathrm{M}} \left(\vec{u} - \vec{v}\right) \frac{dV}{dt}. \tag{2.34}$$

Assuming the bubble is spherical, the time derivative of bubble volume is a function of R and the above equation can be simplified to

$$\vec{F}_{\mathrm{AM}} = m_{\mathrm{f}} C_{\mathrm{M}} \left(\frac{d\vec{u}}{dt} - \frac{d\vec{v}}{dt}\right) + \frac{3 m_{\mathrm{f}} C_{\mathrm{M}}}{R} \left(\vec{u} - \vec{v}\right) \frac{dR}{dt}, \tag{2.35}$$

Auton et al. [40] showed that it is more physical for the derivative of the fluid velocity u to be written as the material derivative

$$\frac{D}{Dt} = \frac{\partial}{\partial t} + u_j \frac{\partial}{\partial x_j}, \tag{2.36}$$

instead of a Lagrangian derivative where

$$\frac{d}{dt} = \frac{\partial}{\partial t} + v_j \frac{\partial}{\partial x_j}. \tag{2.37}$$

The resulting equation for the added-mass force is then is then

$$\vec{F}_{\mathrm{AM}} = m_{\mathrm{f}} C_{\mathrm{M}} \left(\frac{D\vec{u}}{Dt} - \frac{d\vec{v}}{dt} \right) + \frac{3 m_{\mathrm{f}} C_{\mathrm{M}}}{R} \left(\vec{u} - \vec{v} \right) \frac{dR}{dt}, \tag{2.38}$$

which is the equation for the added-mass force found in Johnson and Hsieh [38]. Accounting for change in the bubble size in the added-mass term, the equation for the acceleration of a spherical, massless bubble is

$$\frac{d\vec{v}}{dt} = -2\vec{g} + 3\frac{D\vec{u}}{Dt} + \frac{3}{4}\frac{C_{\mathrm{D}}}{R} \left| \vec{u} - \vec{v} \right| \left(\vec{u} - \vec{v} \right) + 2C_{\mathrm{L}} (\vec{u} - \vec{v}) \times \vec{\omega} + \frac{3}{R} \left(\vec{u} - \vec{v} \right) \frac{dR}{dt}. \tag{2.39}$$

For a single spherical bubble in an infinite medium, the bubble response to pressure variation over time is given by the Rayleigh-Plesset (RP) equation:

$$\rho_{\mathrm{f}} \left[R\frac{d^2 R}{dt^2} + \frac{3}{2} \left(\frac{dR}{dt} \right)^2 \right] = P_B - P_\infty - \frac{2\sigma}{R} - \frac{4\mu_{\mathrm{f}}}{R}\frac{dR}{dt}. \tag{2.40}$$

The relevant variables are the bubble radius $R(t)$, fluid dynamic viscosity μ_{f}, fluid density ρ_{f}, surface tension σ, far-field carrier fluid pressure P_∞ and bubble pressure P_B. The pressure P_{G0} is the partial pressure of gas inside the bubble at reference condition, where bubble radius $R = R_0$ and bubble gas temperature $T_B = T_\infty$,

$$P_{G0} = P_{\infty,0} - P_{\mathrm{v}}(T_\infty) - \frac{2\sigma}{R_0} \tag{2.41}$$

The bubble pressure P_B is assumed to be a poly-tropic function of the ratio of the instantaneous bubble radius R to the initial bubble radius R_0:

$$P_B = P_{\mathrm{v}}(T_B) + P_{G0} \left(\frac{R_0}{R} \right)^{3k}, \tag{2.42}$$

where if $k = 1$ then this expression assumes constant temperature inside the bubble, and $k = \gamma$ assumes an adiabatic behavior, where γ is the ratio of specific heats for air as an

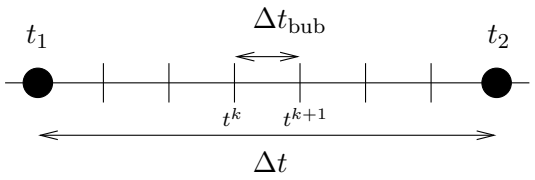

FIGURE 2.10: Discretization of fluid timestep Δt and bubble timestep Δt_{bub} from time t_1 to t_2.

ideal gas [44]. For this work, $k = \gamma$ and the bubble is assumed to be inertially controlled so changes in temperature are not driving the bubble behavior over time. With these assumptions, the equation for the bubble oscillation then becomes

$$R\frac{d^2R}{dt^2} + \frac{3}{2}\left(\frac{dR}{dt}\right)^2 = \frac{P_{\text{v}}(T_\infty) - P_\infty(t)}{\rho_{\text{f}}} + \frac{P_{G0}}{\rho_{\text{f}}}\left(\frac{R_0}{R}\right)^{3\gamma} - \frac{2\sigma}{\rho_{\text{f}}R} - \frac{4\nu_{\text{f}}}{R}\frac{dR}{dt}. \tag{2.43}$$

In the EL approach, the bubbles are assumed small with respect to the surrounding flow, and the pressure P_∞ is taken to be the local pressure at the bubble location. However, in an incompressible flow solver, the absolute value of pressure is not explicitely known - only pressure gradients are important. In order to solve the RP equation, a value for the magnitude of pressure must be obtained. To do this, a reference cavitation number σ_v is defined at some reference location $\vec{x}_\infty$, where

$$\sigma_v = \frac{P_\infty - P_{\text{v}}(T_\infty)}{1/2\rho_{\text{f}}U_\infty^2}. \tag{2.44}$$

It is assumed that σ_v and $P_{\text{v}}(T_\infty)$ are constant throughout the simulation and therefore P_∞ is always a constant. Therefore, once a value for the incompressible field is obtained, the "physical" pressure at each control volume can be found by offsetting the entire domain by $P(\vec{x},t) = P^*(\vec{x},t) - (P_\infty^* - P_\infty)$, where $P^*(\vec{x},t)$ is the instantaneous pressure obtained by the incompressible solver.

2.3.4 Bubble time integration

The bubble position and velocity over time is determined by integrating the bubble acceleration equation (Eqn. 2.32). This is done with a hybrid explicit-implicit approach.

The simulation is broken into two different timescales: the Eulerian fluid timestep Δt and the path integration timestep of the bubbles Δt_{bub}, where $\Delta t = t_2 - t_1$ and $\Delta t_{\text{bub}} = t^{k+1} - t^k$ (See Figure 2.10). The Eulerian fluid variables are known at $t = t_1$ and $t = t_2$ from the advancement of the Navier-Stokes equations.

From the point-particle approximation, each bubble is assigned to the control volume in which its centroid lies. When a bubble is first injected, a brute-force operation on all control volumes is used to find the "home" control volume and processor. On a multi-processor grid, the control volume determines the processor where the bubble data is stored since the carrier-fluid domain is broken into different processors. As a bubble travels throughout the domain, a nearest-neighbor search algorithm is used to find the home control volume. If the nearest-neighbor method should fail, a brute-force approach that searches all control volumes on the local processor is used. If the bubble centroid passes through an inter-processor boundary, the bubble data is then packaged and sent to the "new" bubble processor.

The Eulerian values in Eqn. 2.32 must be evaluated at time $t = t^k$ and at the bubble position $\vec{x} = \vec{Y}^k$ on unstructured grids. Spatial gradients of the carrier-phase parameters at the control volume centroids are obtained using a least-squares method. The fluid velocity at the bubble location $\vec{u}|_{x=Y^k}$ is interpolated from the values at the control volume centroid by

$$\vec{u}(t^k)|_{\vec{x}=\vec{Y}^k} = \vec{u}(t^k)|_{\vec{x}_{\text{cv}}} + \left[\left(\vec{Y}^k - \vec{x}_{\text{cv}}\right) \cdot \vec{\nabla}\right] \vec{u}(t^k)|_{\vec{x}_{\text{cv}}} \tag{2.45}$$

The spatial gradients $\partial u_i / \partial x_j$ are determined at the control volume centroids using a least-squares approach. To obtain the control volume values of velocity required in Eqn. 2.45 at time $t = t^k$, a linear time interpolation is performed using

$$u_i(t^k)\Big|_{\vec{x}_{\text{cv}}} = \frac{1}{\Delta t}\left[\left(t^k - t_1\right) u_i(t_2)|_{\vec{x}_{\text{cv}}} + \left(t_2 - t^k\right) u_i(t_1)|_{\vec{x}_{\text{cv}}}\right]. \tag{2.46}$$

It is assumed that time gradients between t_2 and t_1 are constant and that any $\partial / \partial x_j$ term is constant within the control volume. The vorticity vector at any point inside a

control volume is then

$$\vec{\omega}|^k_{\vec{x}=\vec{Y}^k} = \vec{\omega}|_{\vec{x}_{\rm cv}} = \vec{\nabla} \times \vec{u}|^k_{\vec{x}_{\rm cv}} \,. \tag{2.47}$$

The fluid material derivative at the bubble location at time $t = t^k$ is given by

$$\left.\frac{Du_i}{Dt}\right|^k_{\vec{x}=\vec{Y^k}} = \left.\left(\frac{\partial u_i}{\partial t} + u_j \frac{\partial u_i}{\partial x_j}\right)\right|^k_{\vec{x}=\vec{Y^k}} . \tag{2.48}$$

All values must be interpolated in time to $t = t^k$ and in space to the bubble location $\vec{x} = \vec{Y}^k$. The unsteady term is given by

$$\left.\frac{\partial u_i}{\partial t}\right|^k_{\vec{x}=\vec{Y^k}} = \left.\frac{\partial u_i}{\partial t}\right|^k_{\vec{x}_{\rm cv}} + L^k_j \frac{\partial}{\partial x_j}\left.\left(\frac{\partial u_i}{\partial t}\right)\right|^k_{\vec{x}_{\rm cv}} , \tag{2.49}$$

where the distance vector $\vec{L}$ is equal to the distance from the bubble position to the centroid, $\vec{L} = \vec{Y} - \vec{x}_{\rm cv}$. Assuming that the spatial gradients within a control volume are constant,

$$\left.\frac{\partial u_i}{\partial x_j}\right|^k_{\vec{x}=\vec{Y^k}} = \left.\frac{\partial u_i}{\partial x_j}\right|^k_{\vec{x}_{\rm cv}} , \tag{2.50}$$

and the convective term can be written as

$$\left.\left(u_j \frac{\partial u_i}{\partial x_j}\right)\right|^k_{\vec{x}=\vec{Y^k}} = (u_j)|^k_{\vec{x}=\vec{Y^k}} \left.\left(\frac{\partial u_i}{\partial x_j}\right)\right|^k_{\vec{x}_{\rm cv}} . \tag{2.51}$$

Using the interpolated values of $\vec{u}$ and $D\vec{u}/Dt$, the bubble acceleration $d\vec{v}/dt$ at time $t = t^k$ is known. The velocity at time $t = t^{k+1}$ is integrated using the Adams-Bashforth approach:

$$v_i^{k+1} = v_i^k + \Delta t_{\rm bub} \left(\frac{3}{2} \frac{\partial v_i}{\partial t}^k - \frac{1}{2} \frac{\partial v_i}{\partial t}^{k-1} \right) . \tag{2.52}$$

Once the bubble velocity has been integrated to $t = t^{k+1}$, the bubble position is integrated using the trapezoidal method:

$$Y_i^{k+1} = Y_i^k + \frac{\Delta t_{\rm bub}}{2} \left(v_i^{k+1} + v_i^k \right) . \tag{2.53}$$

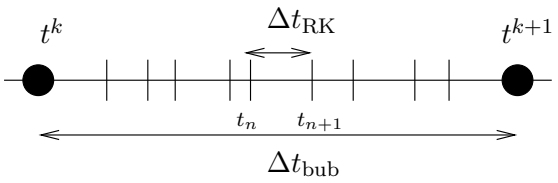

FIGURE 2.11: Discretization of bubble timestep Δt_{bub} and Runge-Kutta timestep Δt_{RK} from time t_k to t_{k+1}.

The bubble equations are advanced from $k, k+1, k+2$, etc. until $t = t_2$ is reached. Then the fluid equations are updated by Δt and the bubble integration process begins anew.

2.3.5 Time integration of bubble radius

Besides integrating the translation of a bubble, the radial variation must also be integrated. Since the behavior of a bubble can be extremely dynamic (especially in regions of collapse), the Rayleigh-Plesset equation is integrated using an adaptive time-stepping mechanism which makes frequent changes in the temporal step-size. The purpose of this adaptive control is to achieve accuracy to a predetermined limit while reducing computational overhead. In regions of large gradients small timesteps are prescribed, while in regions of low gradients larger timesteps are allowed to increase efficiency [45].

The timesteps of the RK integrator Δt_{RK} are generally smaller than that of the bubble translation timestep Δt_{bub}. Δt_{RK} will change over time because of the use of adaptive time-stepping. Figure 2.11 shows the discretization of the time integration using the adaptive RK approach. The bubble radius (and only the bubble radius) is integrated from time t^k to time t^{k+1} by repeatedly advancing the RK solver from t_n to t_{n+1} until $t_{n+1} = t^{k+1}$. The general form of the 4th-order accurate (in time) adaptive Runge-Kutta (RK) formula to solve for y_{n+1} is as follows [46]: First, six coefficients k_i ($i = 1, 2, \ldots, 6$) that represent changes of quantity y at intermediate time-steps must be

TABLE 2.4: Parameters for Runge-Kutta integrator

i	a_i	b_{ij}					c_i	c_i^*
1							$\frac{37}{378}$	$\frac{2825}{27648}$
2	$\frac{1}{5}$	$\frac{1}{5}$					0	0
3	$\frac{3}{10}$	$\frac{3}{40}$	$\frac{9}{40}$				$\frac{250}{621}$	$\frac{18575}{48384}$
4	$\frac{3}{5}$	$\frac{3}{10}$	$-\frac{9}{10}$	$\frac{6}{5}$			$\frac{125}{594}$	$\frac{13525}{55296}$
5	1	$-\frac{11}{54}$	$\frac{5}{2}$	$-\frac{70}{27}$	$\frac{35}{27}$		0	$\frac{277}{14336}$
6	$\frac{7}{8}$	$\frac{1631}{55296}$	$\frac{175}{512}$	$\frac{575}{13824}$	$\frac{44275}{110592}$	$\frac{253}{4096}$	$\frac{512}{1771}$	$\frac{1}{4}$
$j=$		1	2	3	4	5		

found. These are defined by

$$
\begin{aligned}
k_1 &= hf(x_n, y_n) \\
k_2 &= hf(x_n + a_2 h, y_n + b_{2,1} k_1) \\
k_3 &= hf(x_n + a_3 h, y_n + b_{3,1} k_1 + b_{3,2} k_2) \\
k_4 &= hf(x_n + a_4 h, y_n + b_{4,1} k_1 + b_{4,2} k_2 + b_{4,3} k_3) \\
k_5 &= hf(x_n + a_5 h, y_n + b_{5,1} k_1 + b_{5,2} k_2 + b_{5,3} k_3 + b_{5,4} k_4) \\
k_6 &= hf(x_n + a_6 h, y_n + b_{6,1} k_1 + b_{6,2} k_2 + b_{6,3} k_3 + b_{6,4} k_4 + b_{6,5} k_5),
\end{aligned}
$$

where h is the timestep being taken from y_n to y_{n+1} and $f(x_n, y_n) \equiv \partial y(x_n, y_n)/\partial t$. y_{n+1} is advanced in time by

$$y_{n+1} = y_n + c_1 k_1 + c_2 k_2 + c_3 k_3 + c_4 k_4 + c_5 k_5 + c_6 k_6 \tag{2.54}$$

and an embedded formula is

$$y^*_{n+1} = y_n + c^*_1 k_1 + c^*_2 k_2 + c^*_3 k_3 + c^*_4 k_4 + c^*_5 k_5 + c^*_6 k_6, \tag{2.55}$$

The coefficients a_i, b_{ij}, c_i, c_i^* are given in Table 2.4. An error estimate is given by the differences of Eqns. 2.54 and 2.55:

$$\Delta_1 = y_{n+1} - y_{n+1}^* = \sum_{i=1}^{6}(c_i - c_i^*)k_i. \tag{2.56}$$

The scale of the integration can be given by

$$\Delta_0 = \epsilon(|y_n| + \left|h\ \frac{dy}{dx}\right|), \tag{2.57}$$

where ϵ is a tolerance coefficient that is usually set to 1.0×10^{-7}, but can be changed to relax or tighten time-integration accuracy. An estimate for the next time-step of integration is obtained by

$$h_0 = h\left|\frac{\Delta_0}{\Delta_1}\right|^{0.2}. \tag{2.58}$$

If the ratio of relative error $\Delta_1 > \Delta_0$, then retry the present (failed) step with $h = h_0$. Otherwise set $\Delta t_{n+1} = h_0$ for the next step. The Rayleigh-Plesset equation is integrated first for $\dot{R}$ and then R, using the above method. This allows us to control the simulation error based on the change in radius over time of the bubble, $\dot{R} \equiv \partial R/\partial t$ and radial acceleration $\ddot{R} \equiv \partial^2 R/\partial t^2$. The coefficients of integration for $\dot{R}$ are

$$\begin{aligned}
k_{\dot{R}_1} &= f_{\dot{R}}(R_n, \dot{R}_n) \\
k_{\dot{R}_2} &= f_{\dot{R}}(R_1, \dot{R}_1) \\
k_{\dot{R}_3} &= f_{\dot{R}}(R_2, \dot{R}_2) \\
k_{\dot{R}_4} &= f_{\dot{R}}(R_3, \dot{R}_3) \\
k_{\dot{R}_5} &= f_{\dot{R}}(R_4, \dot{R}_4) \\
k_{\dot{R}_6} &= f_{\dot{R}}(R_5, \dot{R}_5).
\end{aligned}$$

The acceleration of the bubble radius over time is explicitly defined in the RP equation, and so the time derivatives are defined as:

$$f_{\dot{R}}(R, \dot{R}) = \ddot{R} = \frac{1}{R}\left[-\frac{3}{2}\dot{R}^2 + \frac{P_B - P_\infty}{\rho_\mathrm{f}} - \frac{2\sigma}{\rho_\mathrm{f} R} - \frac{4\nu_\mathrm{f}\dot{R}}{R}\right] \tag{2.59}$$

$$f_R(t, R) = \dot{R} \tag{2.60}$$

Since $\dot{R}$ is the time derivative of R, the derivative functions are found in the following form:

$$\begin{aligned}
\dot{R}_1 &= \dot{R}_n + \Delta t_n b_{2,1} k_{\dot{R}_1} \\
R_1 &= R_n + \Delta t_n b_{2,1} \dot{R}_n \\
\dot{R}_2 &= \dot{R}_1 + \Delta t_n (b_{3,1} k_{\dot{R}_1} + b_{3,2} k_{\dot{R}_2}) \\
R_2 &= R_1 + \Delta t_n (b_{3,1} \dot{R}_n + b_{3,2} \dot{R}_1) \\
\dot{R}_3 &= \dot{R}_2 + \Delta t_n (b_{4,1} k_{\dot{R}_3} + b_{4,2} k_{\dot{R}_3} + b_{4,3} k_{\dot{R}_3}) \\
R_3 &= R_2 + \Delta t_n (b_{4,1} \dot{R}_n + b_{4,2} \dot{R}_1 + b_{4,3} \dot{R}_2) \\
\dot{R}_4 &= \dot{R}_3 + \Delta t_n (b_{5,1} k_{\dot{R}_4} + b_{5,2} k_{\dot{R}_4} + b_{5,3} k_{\dot{R}_4} + b_{5,4} k_{\dot{R}_4}) \\
R_4 &= R_3 + \Delta t_n (b_{5,1} \dot{R}_n + b_{5,2} \dot{R}_1 + b_{5,3} \dot{R}_2 + b_{5,4} \dot{R}_3) \\
\dot{R}_5 &= \dot{R}_4 + \Delta t_n (b_{6,1} k_{\dot{R}_5} + b_{6,2} k_{\dot{R}_5} + b_{6,3} k_{\dot{R}_5} + b_{6,4} k_{\dot{R}_5} + b_{6,5} k_{\dot{R}_5}) \\
R_5 &= R_4 + \Delta t_n (b_{6,1} \dot{R}_n + b_{6,2} \dot{R}_1 + b_{6,3} \dot{R}_2 + b_{6,4} \dot{R}_3 + b_{6,5} \dot{R}_4).
\end{aligned}$$

The carrier-fluid pressure must be evaluated at the intermediate timesteps. To do this, the bubble position is assumed to vary linearly from $\vec{Y}^k$ to $\vec{Y}^{k+1}$ and

$$\vec{Y}(t_n) = \frac{1}{\Delta t_{\text{bub}}} \left[\left(t_n - t^k \right) \vec{Y}(t^{k+1}) + \left(t^{k+1} - t_n \right) \vec{Y}(t^k) \right]. \tag{2.61}$$

Once the location is known, the bubble pressure $P_n(\vec{x} = \vec{Y}_n)$ using a linear interpolation function similar to Eqn. 2.45

$$P_n(t_n)|_{\vec{x}=\vec{Y}(t_n)} = P(t_n)|_{\vec{x}_{\text{cv}}} + \left[\left(\vec{Y}(t_n) - \vec{x}_{\text{cv}} \right) \cdot \vec{\nabla} \right] P(t_n)|_{\vec{x}_{\text{cv}}} \tag{2.62}$$

and Eqn. 2.46

$$P(t_n)|_{\vec{x}_{\text{cv}}} = \frac{1}{\Delta t} \left[(t_n - t_1)\, P(t_2)|_{\vec{x}_{\text{cv}}} + (t_2 - t_n)\, P(t_1)|_{\vec{x}_{\text{cv}}} \right]. \tag{2.63}$$

The relative error terms are calculated as:

$$\Delta_0 = \epsilon(\left|\dot{R}_n\right| + \left|\Delta t_n k_{\dot{R}_1}\right|) \tag{2.64}$$

$$\Delta_1 = \Delta t_n((c_1 - c_1^*)\dot{R}_1 + (c_3 - c_3^*)\dot{R}_3 + (c_4 - c_4^*)\dot{R}_4 + (c_5 - c_5^*)\dot{R}_5 + (c_6 - c_6^*)\dot{R}_6) \tag{2.65}$$

If $\frac{\Delta_0}{\Delta_1} < 1$, the error is greater than the tolerance. Then find Δt_n^*, which is the timestep that the time integration should be re-run with if the error tolerance criterion is not met for timestep Δt_n, by

$$\Delta t_1 = S\Delta t_n \left|\frac{\Delta_0}{\Delta_1}\right|^{0.25}, \tag{2.66}$$

$$\Delta t_n^* = \text{MAX}\left(\Delta t_1, \frac{\Delta t_n}{10}, \right) \tag{2.67}$$

where S is a safety factor, chosen to be 0.9. If $\frac{\Delta_0}{\Delta_1} > 1$, the error is less than the tolerance. If $\frac{\Delta_0}{\Delta_1} > \epsilon_1$, where ϵ_1 is an arbitrary, small number ($\sim 10^{-4}$), then the time-step is increased for the next iteration by

$$\Delta t_{n+1} = S\Delta t_n \left|\frac{\Delta_0}{\Delta_1}\right|^{0.2}. \tag{2.68}$$

If $\frac{\Delta_0}{\Delta_1} > 1$ and $\frac{\Delta_0}{\Delta_1} < \epsilon_1$ then

$$\Delta t_{n+1} = 5\Delta t_n \tag{2.69}$$

so there is no more than a factor of five increase in the time-step. If $\frac{\Delta_0}{\Delta_1} > 1$ then the present (failed) timestep is recalculated using the updated timestep Δt_n^*. If $\frac{\Delta_0}{\Delta_1} < 1$ then the solution is updated using Δt_n and Δt_{n+1} is used for the next timestep. The solution for $\dot{R}$ and R is then updated for the next timestep using

$$\dot{R}_{n+1} = \dot{R}_n + \Delta t_n \left(c_1 k_{\dot{R}_1} + c_3 k_{\dot{R}_3} + c_4 k_{\dot{R}_4} + c_6 k_{\dot{R}_6}\right), \tag{2.70}$$

$$R_{n+1} = R_n + \Delta t_n \left(c_1 \dot{R}_n + c_3 \dot{R}_2 + c_4 \dot{R}_3 + c_6 \dot{R}_5\right). \tag{2.71}$$

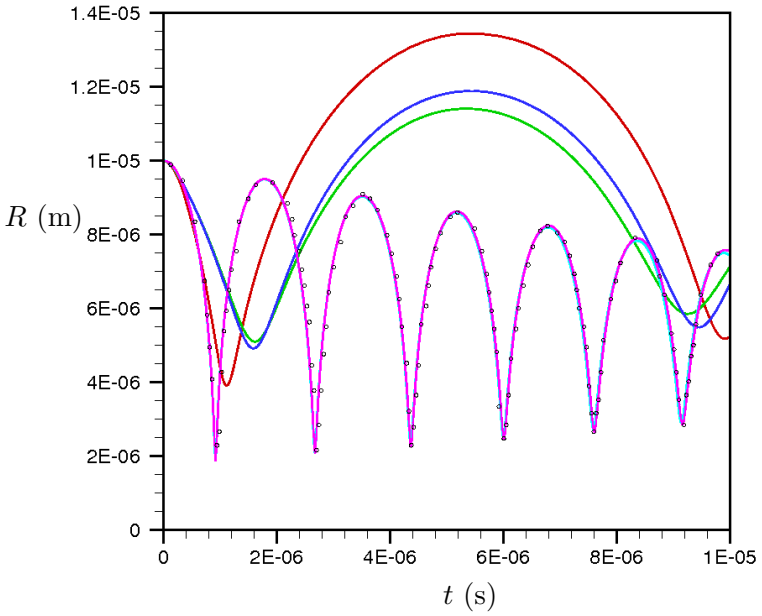

FIGURE 2.12: Convergence of bubble radius vs. time for different values of ϵ. — $\epsilon = 1 \times 10^{-3}$, — $\epsilon = 1 \times 10^{-4}$, — $\epsilon = 1 \times 10^{-5}$, — $\epsilon = 1 \times 10^{-6}$, — $\epsilon = 1 \times 10^{-7}$, ∘ Popinet and Zaleski [23]

2.3.6 RK4 validation: a single oscillating bubble

To test the adaptive-timestepping Rayleigh-Plesset integrator, a simple test case was compared to that documented by Popinet and Zaleski [23]. A single bubble is simulated in a domain of quiescent fluid. Since there is no relative motion with respect to the fluid flow, the only motion is the oscillation of the bubble. The bubble oscillates in a sequence of collapses and rebounds until equilibrium is reached. The physical parameters are as follows: surface tension coefficient $\sigma = 0.07$ N/m, $P_\infty = 10^5$ Pa, dynamic viscosity $\mu_\mathrm{f} = 0.001$ N $\cdot$ s/m^3, $\rho_\mathrm{f} = 1000$ kg/m^3.

In the RK4 integrator ϵ determines the tolerance to which the solution must converge to. Decreasing ϵ will reduce the timestep in regions of large gradients, increasing time accuracy. This also increases simulation runtime. The plot below shows the convergence results of R vs. t when ϵ is varied. For large ϵ, the solution is very poor. When ϵ is

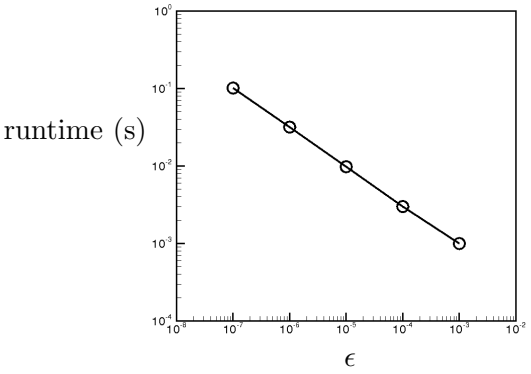

FIGURE 2.13: Relationship between ϵ and runtime.

decreased, the simulation reaches good agreement with the simulation by Popinet and Zaleski [23]. The RK4 ODE integrator compares well to the simulation by Popinet and Zaleski [23], as shown in Figure 2.12.

Increasing time accuracy does come at a price, and Figure 2.13 shows the increase in runtime as the tolerance is decreased. The runtime is calculated as the average time spent in the RK4 subroutine averaged over 5 runs. When running a simulation with a large amount of bubbles, a compromise between simulation runtime and time accuracy will have to be considered.

2.3.7 Validation: Gas nuclei trajectories over a blunt body

Johnson and Hsieh [38] numerically studied gas nuclei traversing a two-dimensional blunt body. Assuming potential flow for the fluid, Johnson and Hsieh [38] obtained an analytical solution for fluid velocity and pressure. A Lagrangian equation for bubble dynamics was derived and integrated with the fluid phase to obtain an ordinary differential equation for the bubble motion.

Using the Euler-Lagrangian model coupled with the single-phase Navier-Stokes solver, similar results are obtained while not assuming potential flow. The bubbles are assumed to be small and spherical and the change of bubble radius over time is governed by

the Rayleigh-Plesset equation. Bubbles are injected upstream of the blunt body, then travel downstream and around the obstacle in response to the pressure gradient and drag forces. In an Euler-Lagrangian framework, the bubble velocity is given in Johnson and Hsieh [38] as

$$\frac{dv_i}{dt} = -3\frac{\partial p}{\partial x_i} + \frac{3}{R}\left(u_i - v_i\right)\frac{dR}{dt} + \frac{18\mathrm{Re}_b}{R^2\mathrm{Re}_f}\frac{C_D}{24}\left(u_i - V_i\right). \tag{2.72}$$

The first term on the right hand side in Eqn. 2.72 is the pressure gradient term. The bubbles are repulsed from areas of increasing pressure and attracted by favorable pressure gradients. The second term includes volume variation effects. For this problem, the volume variation term is neglected, as in Johnson and Hsieh [38]. The last term includes the bubble drag. An empirical relation for the drag coefficient of small, spherical particles by Haberman and Morton [41] is used, where

$$C_D = \frac{24}{\mathrm{Re}_b}\left(1 + 0.197{\mathrm{Re}_b}^{0.63} + 2.6\times10^{-4}{\mathrm{Re}_b}^{1.38}\right). \tag{2.73}$$

Note that as $\mathrm{Re}_b \to 0$ then the drag relation approaches the Stokes limit of $C_D = 24/\mathrm{Re}_b$. The bubble Reynolds number (Re_b), fluid Reynolds number (Re_f), Weber number (We) and the vapor cavitation number (σ_v) are defined as

$$\mathrm{Re}_b = \frac{2R\left|u_i - V_i\right|}{\nu_\mathrm{f}}, \quad \mathrm{Re}_f = \frac{hU_o}{\nu_\mathrm{f}},$$

$$\mathrm{We} = \frac{\rho_f {U_o}^2 R_o}{S}, \quad \sigma_v = \frac{p_o - p_v}{1/2\rho_f {U_o}^2},$$

with h defined as the width of the blunt body, and U_o as the free-stream velocity value. Simulating the Reynolds number given by Johnson and Hsieh [38] (Re_f = 238,095) requires resolving the very thin laminar boundary layer. Outside the boundary layer, the Reynolds number does not affect the velocity field. As the bubbles remain outside the boundary layer for the entire simulation, sufficient accuracy for the velocity field can be obtained by solving the velocity field at a lower Reynolds number than specified by Johnson and Hsieh [38].

After progressively increasing the Reynolds number, results showed that a Reynolds

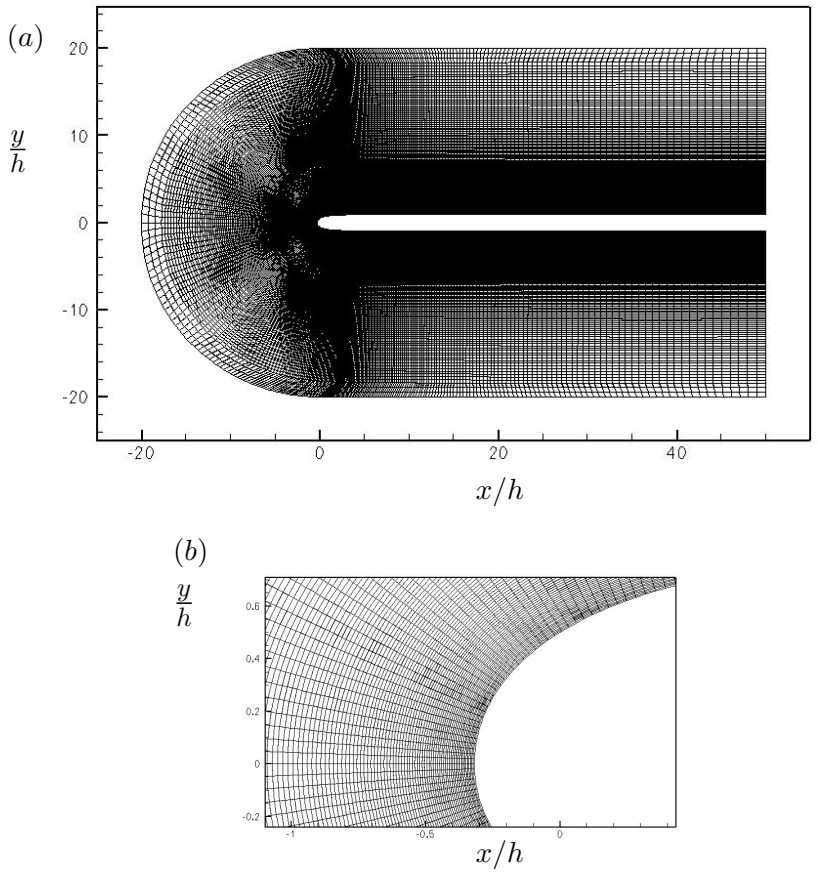

FIGURE 2.14: Unstructured mesh generated for simulation of gas nuclei flowing over a blunt body. (a) Full mesh. (b) Zoomed-in view near blunt body.

number of $\mathrm{Re}_f = 10^4$ provides good agreement for the velocity field. The bubble velocity equation and Re_b still retain the original value of viscosity (i.e. $\mathrm{Re}_b = 248,095$ though a change in ν_f for Re_b but not Re_f). Also, the vapor cavitation number (σ_v) is 0.4 and the Weber number is 976. The vapor pressure p_v is absorbed into the free-stream pressure, so the reference pressure term becomes $p_o = \sigma_v \rho_f {U_o}^2/2$.

The grid contains 261,600 hexagonal control volumes, with an initial wall-normal distance of $0.005h$. The grid extends from $-25 \leq x/h \leq 50$ and $-25 \leq y/h \leq 25$. Three control volumes resolve the space between the periodic faces (in the z-direction). Figure 2.14 depicts the resolution of the mesh. Figure 2.14a shows the grid in its entirety, while Figure 2.14b shows the boundary layer resolution.

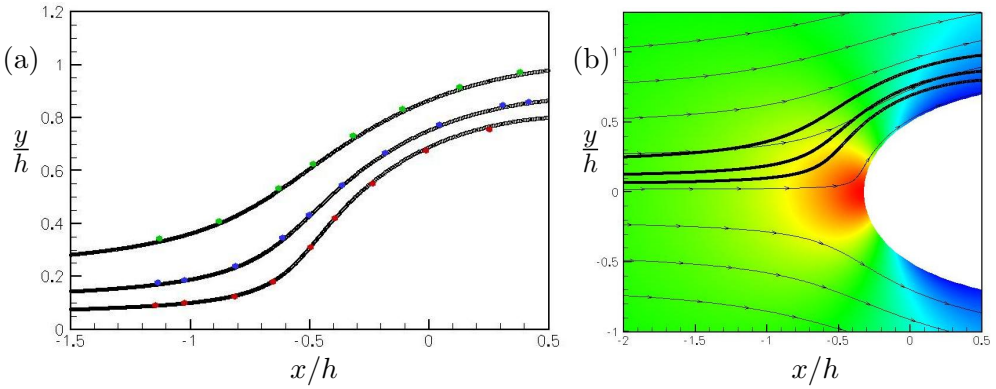

FIGURE 2.15: Comparison of bubble trajectories to Johnson and Hsieh [38], with $\sigma_v = 0.4$. The data by Johnson and Hsieh [38] is given in (a) by the filled circles, with $y_o/h = 0.05$ (●), $y_o/h = 0.1$ (●) and $y_o/h = 0.2$ (●). Figure (b) plots bubble trajectories along with pressure color contours and velocity streamlines. Red represents high pressure and blue low pressure.

Three bubbles are injected at a streamwise distance of $x_o/h = -10$ at three different vertical positions ($y_o/h = 0.2, 0.1$ and 0.05). The bubbles follow the streamlines until they approach the blunt body. The bubbles are then repelled from the blunt body by the adverse pressure gradient and no longer follow the fluid streamlines. Also, the bubble radii decrease in the high pressure regions as the bubble attempts to achieve pressure equilibrium. Eventually, the bubble trajectory brings it around the bluff body into the low-pressure region, where the bubble grows. Figure 2.15a plots the bubble trajectories and demonstrates good agreement between the Euler-Lagrangian simulation (black dots) and the Johnson and Hsieh [38] results (large colored dots). The colors represent the initial injection position, with red dots for $y_o/h = 0.05$, blue dots for $y_o/h = 0.1$ and green dots for $y_o/h = 0.2$. Fluid streamlines, pressure contours and bubble trajectories are plotted in Figure 2.15b. The color contour gives the relative pressure magnitude, over a scale from high (red) to low (blue). In comparing to the numerical investigation by Johnson and Hsieh [38], the Euler-Lagrangian method coupled with the Rayleigh-Plesset equation accurately reproduces results for the flow of gas nuclei about a blunt body.

2.3.8 Collision Model

2.3.8.1 Constant Radius

A collision model assuming binary, hard-sphere collisions [47] is used. The simulation is broken into two different timescales: the Eulerian fluid timestep Δt and the path integration timestep of the bubbles Δt_{bub}, where $\Delta t = t_2 - t_1$ and $\Delta t_{\text{bub}} = t^{k+1} - t^k$. The timestep Δt_{bub} is the timescale the bubbles will be integrated with if no collisions occur (See Figure 2.10).

The time it takes for bubble 1 to collide with bubble 2 is defined as $t_{1,2}$. At the moment of collision, bubbles 1 and 2 are touching, with zero distance between them. For bubbles with a constant radius and assuming constant bubble velocities between collisions, the equation for position at the moment of collision is

$$|\vec{r}_{1,2}(t + t_{1,2})| = |\vec{r}_{1,2}(t) - \vec{v}_{1,2}t_{1,2}| = R_1 + R_2, \tag{2.74}$$

where $\vec{r}_{1,2}$ is the relative position of two bubbles 1 and 2

$$\vec{r}_{1,2} = \vec{Y}_2 - \vec{Y}_1 \tag{2.75}$$

and $\vec{v}_{1,2}$ is the relative velocity between the two bubbles 1 and 2 (in the frame of reference of bubble 1), defined as

$$\vec{v}_{1,2} = \vec{v}_2 - \vec{v}_1. \tag{2.76}$$

Figure 2.16 is a schematic of a binary collision between bubbles 1 and 2.

The variable $b_{1,2}$ is defined by $b_{1,2} = \vec{r}_{1,2} \cdot \vec{v}_{1,2}$. Collision will only occur between bubbles 1 and 2 if $b_{1,2} < 0$, since if $\vec{r}_{1,2} \cdot \vec{v}_{1,2} > 0$, the bubbles are moving away from each other. The collision angle θ_{c} is given by

$$\theta_{\text{c}} = \cos^{-1}\left[\frac{\vec{r}_{1,2} \cdot \vec{v}_{1,2}}{|\vec{r}_{1,2}|\,|\vec{v}_{1,2}|}\right].$$

The variable σ_r is defined as the distance between the centers of bubbles 1 and 2. At the moment of collision, σ_r is equal to $R_1 + R_2$. Taking Eqn. 2.74 and squaring both

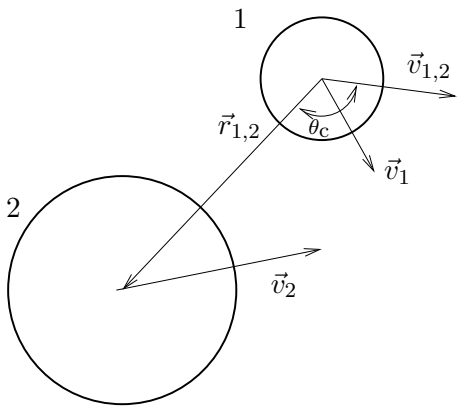

FIGURE 2.16: Schematic of parameters of collision between bubble 1 and bubble 2.

sides, we obtain

$$|\vec{r}_{1,2}(t) - \vec{v}_{1,2}t_{1,2}|\,|\vec{r}_{1,2}(t) - \vec{v}_{1,2}t_{1,2}| = \sigma_r^2, \tag{2.77}$$

which can be expanded to

$$|\vec{r}_{1,2}|^2 + 2b_{1,2}t_{1,2} + |\vec{v}_{1,2}|^2\, t_{1,2}^2 - \sigma_r^2 = 0. \tag{2.78}$$

This quadratic equation can be solved for $t_{i,j}$ to obtain

$$t_{1,2} = \frac{-b_{1,2} \pm \sqrt{b_{1,2}^2 - |\vec{v}_{1,2}|^2\,(|\vec{r}_{1,2}|^2 - \sigma_r^2)}}{|\vec{v}_{1,2}|^2}. \tag{2.79}$$

Taking the smallest root leaves the equation

$$t_{1,2} = \frac{-b_{1,2} - \sqrt{b_{1,2}^2 - |\vec{v}_{1,2}|^2\,(|\vec{r}_{1,2}|^2 - \sigma_r^2)}}{|\vec{v}_{1,2}|^2} \tag{2.80}$$

for the time to collision. Note that the only physical solution is one with a positive square-root term, so $b_{1,2}^2$ must be greater than $|\vec{v}_{1,2}|^2\,(|\vec{r}_{1,2}|^2 - \sigma_r^2)$.

The time to collision is found by obtaining the smallest real solution of Eqn. 2.78 for $t_{1,2}$.

2.3.8.2 Allowing for variable radius

The previous section calculates the time to collision for a pair of constant-radius particles. The equations can be generalized to account for a variation in bubble radius, allowing calculation of collision for particles that are changing radius over time more accurately.

The hard-sphere collision equation with a constant radius is given by Eqn. 2.74. Recall that $\sigma_r = R_1 + R_2$ and is a constant. This constraint can be relaxed to obtain

$$|\vec{r}_{1,2}(t + t_{1,2})| = |\vec{r}_{1,2}(t) - \vec{v}_{1,2}t_{1,2}| = \sigma_r(t + t_{1,2}), \tag{2.81}$$

which describes the location of the colliding particles at the time of collision, assuming constant relative velocities and spherical particles. A Taylor expansion can be obtained to find $\sigma_r(t + t_{1,2})$

$$\begin{aligned} \sigma_r(t + t_{1,2}) &= R_1(t) + R_2(t) + t_{1,2}\left(\dot{R}_1(t) + \dot{R}_2(t)\right) + \\ &\quad \frac{t_{1,2}^2}{2}\left(\ddot{R}_1(t) + \ddot{R}_2(t)\right) + O\left(t_{1,2}\right)^3, \end{aligned} \tag{2.82}$$

where $R(t)$, $\dot{R}(t)$ and $\ddot{R}(t)$ are all known from the RP equation (Eqn. 2.43). For simplicity, the change in radius is assumed to be constant ($\ddot{R} \approx 0$). Then, σ_r can be reduced to

$$\sigma_r(t + t_{1,2}) = R_1(t) + R_2(t) + t_{1,2}\left(\dot{R}_1(t) + \dot{R}_2(t)\right). \tag{2.83}$$

Taking Eqn. 2.81 and squaring both sides, we obtain

$$|\vec{r}_{1,2}(t) - \vec{v}_{1,2}t_{1,2}|\,|\vec{r}_{1,2}(t) - \vec{v}_{1,2}t_{1,2}| = \sigma_r^2, \tag{2.84}$$

which can be expanded to

$$|\vec{r}_{1,2}|^2 + 2b_{1,2}t_{1,2} + |\vec{v}_{1,2}|^2 t_{1,2}^2 - \sigma_r^2 = 0, \tag{2.85}$$

where σ_r^2 is now

$$\sigma_r^2 = \left(R_1 + R_2 + t_{1,2}\left(\dot{R}_1 + \dot{R}_2\right)\right)^2. \tag{2.86}$$

The variables $\sigma_a = R_1 + R_2$ and $\sigma_b = \dot{R}_1 + \dot{R}_2$ are defined and Eqn. 2.86 then can be expanded to

$$\sigma_r^2 = \sigma_a^2 + 2\sigma_a\sigma_b t_{1,2} + \sigma_b^2 t_{1,2}^2. \tag{2.87}$$

Substituting for σ_r^2 in Eqn. 2.85 gives

$$|\vec{r}_{1,2}|^2 + 2b_{1,2}t_{1,2} + |\vec{v}_{1,2}|^2 t_{1,2}^2 - \left(\sigma_a^2 + 2\sigma_a\sigma_b t_{1,2} + \sigma_b^2 t_{1,2}^2\right) = 0. \tag{2.88}$$

This is a quadratic equation, where a solutions exists that is of the form

$$t_{1,2} = \frac{B \pm \sqrt{B^2 - 4AC}}{2A}, \tag{2.89}$$

where

$$A = |\vec{v}_{1,2}|^2 - \sigma_b^2 \tag{2.90}$$

$$B = 2b_{1,2} - 2\sigma_a\sigma_b \tag{2.91}$$

$$C = |\vec{r}_{1,2}|^2 - \sigma_a^2. \tag{2.92}$$

Since the solution must be real, $B^2 > 4AC$. The smallest, positive solution of the quadratic equation for the time to collision $t_{1,2}$ is then

$$t_{1,2} = \frac{(\sigma_a\sigma_b - b_{1,2}) - \sqrt{(b_{1,2} - \sigma_a\sigma_b)^2 - (\left|\vec{V}_{1,2}\right|^2 - \sigma_b^2)(|\vec{r}_{1,2}|^2 - \sigma_a^2)}}{\left|\vec{V}_{1,2}\right|^2 - \sigma_b^2}, \tag{2.93}$$

when $\vec{r}_{1,2}\cdot\vec{v}_{1,2} - (R_1 + R_2)\left(\dot{R}_1 + \dot{R}_2\right) < 0$ and $\left|\vec{V}_{1,2}\right|^2 - \left(\dot{R}_1 + \dot{R}_2\right)^2 < 0$. This equation for the amount of time until the next bubble collision is used for bubbles that are traveling towards each other ($\vec{r}_{1,2}\cdot\vec{v}_{1,2} < 0$) and accounts for the 1st-order effects of change in bubble radius over time.

2.3.8.3 Collision list

Each processor has a list of bubbles located within the local control volumes of the carrier-phase fluid. The total number of bubbles on a local processor is defined as N_{sys}.

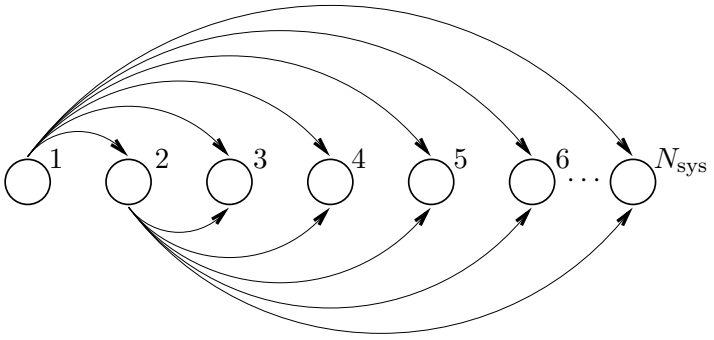

FIGURE 2.17: Schematic of collision partner calculations for bubbles 1 and 2. Arrows denote evaluation of collision timescale for bubble i with j.

The list contains all instantaneous bubble properties and is updated every Δt through inter-processor communication to account for bubbles crossing the inter-processor boundaries. Collision partners are systematically determined by looping over the collision lists to obtain the time to collision for each bubble $t_{1,2}$. After every N_{update} fluid timesteps, the collision partner p of each bubble is determined using an up-list approach (Figure 2.17). The up-list approach is performed as follows: for each bubble i, bubbles $j = i+1, i+2,\ \ldots\ , N_{\text{sys}}$ are used to calculate collision times between bubbles i and j

$$t_{1,2}(i) = \min\left[t_{1,2}(i,j)\right] \text{ for } j = i+1, N_{\text{sys}}, \tag{2.94}$$

and the collision partner p of bubble i is the index of bubble j which was used to obtain $t_{1,2}(i)$. The minimum time to collision t is obtained by finding the minimum collision time $t_{i,j}$ over all local bubbles

$$t_{\text{col}} = \min\left[t_{1,2}(i)\right] \text{ for } i = 1, N_{\text{sys}}. \tag{2.95}$$

The integration of the bubble position over Δt is performed as follows, starting from $t^k = t_1$:

(a) Looping over all particles, find collision partners by determining the minimum $t_{1,2}$ for each bubble pair.

(b) Determine the minimum collision time, t_{col} by finding the minimum $t_{1,2}$ over all collision pairs.

if $t_{\text{col}} < \Delta t_{\text{bub}}$

(c) Advance all bubbles by t_{col} and apply collision dynamics to the collision pair.

(d) Update collision partners of the bubbles that have just collided.

else

(c) Advance all bubbles by Δt_{bub}.

if $t > t_2$

Go back to (a).

else

Go back to (b).

This loop is performed until all bubbles have been integrated to t^{k+1}. The process is repeated until $t^{k+1} = t_2$, after which the Eulerian fluid equations are advanced and all bubble collision partners are recalculated if N_{update} is a factor of the total number of timesteps performed. Then the bubble position integration process begins anew.

When (d) is implemented, the collision partners and collision timescales of the bubbles i, j that have just collide are updated using a combination of up-list and down-listing (Figure 2.18). Both bubbles i and j loop over the entire collision list to determine their new collision partners and collision timescale.

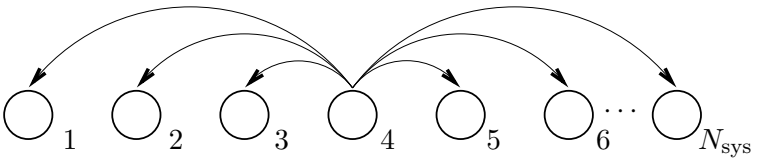

FIGURE 2.18: Schematic of collision partner calculations for bubble $i = 4$, which has just collided with another bubble and requires updating to find its new collision partner.

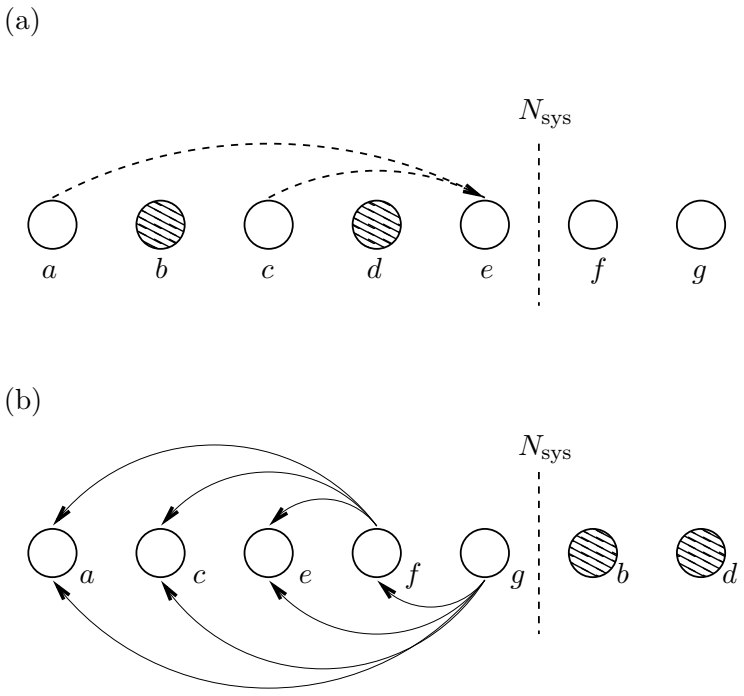

FIGURE 2.19: Update procedure for collision list when losing / gaining particles on processor after inter-processor communication or injection of bubbles. (a): Bubbles a and c have previously computed bubbles e as collision partner. Bubbles b and c have been moved to another processor. Bubbles f and g have been passed into the local processor from another processor or through bubble injection directly. (b): Packing procedure has been applied so that all local bubbles (from 1 to N_{sys}) are included in updated collision list. Collision partners updated for bubbles f and g through down-list procedure.

If $N_{\text{update}} > 1$ then bubbles that are introduced to the local processor through bubble injection and inter-processor communication must be accounted for. Also, bubbles that have left the local processor must be removed from the collision list. If the collision partner p of bubble i has left the local processor, then the up-list / down-list algorithm is applied to find a new collision partner. For bubbles that have just been put on the local processor, the down-list search algorithm is applied (Figure 2.19).

2.3.9 Coalescence Model

When two bubbles collide, a thin liquid film is sandwiched between two bubbles. The energy of collision leads to deformation of the bubble surface and the subsequent separation of the bubbles. Surface tension leads to thinning of the liquid film and coalescence occurs if the bubbles have not separated before the film ruptures. The ratio of two timescales, the film drainage timescale t_d and the bubble-bubble interaction timescale t_i, describes the likelihood of coalescence.

A method for determining the probability of coalescence at the moment of collision was developed using a DNS Euler-Lagrangian formulation. The probability of coalescence is determined stochastically as in Kamp et al. [48], with the probability of coalescence computed from a ratio of coalescence timescales. In the Euler-Lagrangian approach, the bubble velocities are directly determined from the instantaneous Eulerian flow field and bubble-bubble collisions are computed for each bubble as discrete events.

The Kamp et al. [48] model was derived under the assumption of large Reynolds numbers, with bubbles coming into contact due to turbulent fluctuations (ignoring mean gradients in the flow and buoyant effects) and the turbulent flow and bubble velocities were modeled using a RANS approach. However, RANS methodologies are generally not accurate when simulating separated flow or particle transport, due to regions of anisotropy in the turbulent fluctuations and the fact that path lines integrated on a mean field are inherently different than mean paths obtained from instantaneous path lines. Simulations of passive scalar transport using DNS [49] demonstrated the invalidity of the eddy-viscosity hypothesis to model scalar mixing. To predict particle or

bubble transport, it is important to have realistic velocity fields encountered along particle/bubble trajectories. With large-eddy simulation (LES), the large scales of the flow that contain a majority of the kinetic energy are resolved and the sub-grid turbulent scales are modeled, increasing the numerical accuracy.

The one-way coupled Euler-Lagrangian model solves for the individual motion of the bubbles coupled with the DNS/LES flow field and directly computes the bubble-bubble collisions as discrete events. Once a bubble-bubble collision has occurred, bubble coalescence is determined stochastically using and expression for the probability of coalescence [48]. The one-way coupled Euler-Lagrangian model was developed in the context of computing flow over complex geometries and can be easily extended to LES simulations, since the bubble velocities are directly determined without closure models for the turbulence and bubble-bubble collisions are computed for each bubble as discrete events.

2.3.10 Conservation of kinetic energy

Consider two spheres with radii R_1 and R_2 approaching each other along their line of centers with velocities U_1 and U_2. The velocities U_1 and U_2 are obtained by taking the component of the bubble velocities along the collision line-of-centers. The vector $\vec{r}_{1,2}$ pointing from the center of bubble 1 to the center of bubble 2 is $\vec{r}_{1,2} = \vec{Y}_2 - \vec{Y}_1$, where $\vec{Y}_1$ is the location of the center of bubble 1. The unit normal vector $\hat{n}_{1,2}$ pointing from bubble 1 to 2 is given by $\hat{n}_{1,2} = \vec{r}_{1,2}/|\vec{r}_{1,2}|$. The velocities normal and tangential to the line of centers are then

$$U_1 = v_{1,N} = \vec{u}_1 \cdot \hat{n}_{1,2}, \quad \vec{v}_{1,T} = \vec{v}_1 - u_{1,N}\hat{n}_{1,2}$$
$$U_2 = v_{2,N} = \vec{u}_2 \cdot \hat{n}_{1,2}, \quad \vec{v}_{2,T} = \vec{v}_2 - u_{2,N}\hat{n}_{1,2}$$

For surfactant-free surfaces, the shear stress at the bubble surface is zero, and a potential flow can be used to describe the flow field, in the limit of large Reynolds numbers. The kinetic energy due to the motion of the two spheres can then be expressed [50] by

$$E_k = \frac{1}{2}\left(LU_1^2 - 2MU_1U_2 + NU_2^2\right). \tag{2.96}$$

with the coefficients determined by

$$L = \frac{2}{3}\pi\rho_{\mathrm{f}}R_1^3\left(1 + \frac{3R_1^3R_2^3}{l^3f_1^3} + \frac{3R_1^6R_2^6}{l^3f_1^3\left(l-f_2\right)^3f_3^3} + ...\right) \tag{2.97}$$

$$M = 2\pi\rho_{\mathrm{f}}\frac{R_1^3R_2^3}{l^3}\left(1 + \frac{R_1^3R_2^3}{g_1^3\left(l-g_2\right)^3} + \frac{R_1^6R_2^6}{g_1^3g_3^3\left(l-g_2\right)^3\left(l-g_4\right)^3} + ...\right) \tag{2.98}$$

$$N = \frac{2}{3}\pi\rho_{\mathrm{f}}R_2^3\left(1 + \frac{3R_1^3R_2^3}{l^3g_1^3} + \frac{3R_1^6R_2^6}{l^3g_1^3\left(l-g_2\right)^3g_3^3} + ...\right), \tag{2.99}$$

with

$$f_1 = l - R_2^2/l, f_2 = R_1^2/f_1, f_3 = l - R_2^2/(l-f_2), f_4 = R_1^2/f_3, \tag{2.100}$$

$$g_1 = l - R_1^2/l, g_2 = R_2^2/g_1, g_3 = l - R_1^2/(l-g_2), g_4 = R_2^2/g_3, \tag{2.101}$$

where $l = |\vec{Y_2} - \vec{Y_1}|$. It is clear from these expressions that as two particles approach each other, the velocities will change to conserve the total kinetic energy. As the two bubbles approach each other, the coefficients L, M and N in Eqn. 2.96 approach the values L_0, M_0 and N_0 as $l \to R_1 + R_2$. At the moment of collision, the sum of the forces (positive in the direction from bubble 1 to bubble 2) can be calculated using Lagrange's equations

$$F_1 = \frac{\mathrm{d}}{\mathrm{d}t}\frac{\partial E_k}{\partial U_1} - \frac{\partial E_k}{\partial x_1}, F_2 = \frac{\mathrm{d}}{\mathrm{d}t}\frac{\partial E_k}{\partial U_2} - \frac{\partial E_k}{\partial x_2}.$$

The sum of forces is zero, and the spatial terms are exactly opposite (since $\partial x_1 = -\partial x_2$). The time derivative terms are

$$\frac{\partial E_k}{\partial U_1} = L_0U_1 - M_0U_2, \frac{\partial E_k}{\partial U_2} = N_0U_2 - M_0U_1,$$

and summing these terms results in

$$\frac{\mathrm{d}}{\mathrm{d}t}\left[\left(L_0 - M_0\right)U_1 + \left(N_0 - M_0\right)U_2\right] = 0. \tag{2.102}$$

Since these terms are only a function of time,

$$\left(L_0 - M_0\right)U_1 + \left(N_0 - M_0\right)U_2 = \text{constant}. \tag{2.103}$$

We can define terms $m_1 = L_0 - M_0$ and $m_2 = N_0 - M_0$ to define a composite average velocity U_0 as

$$U_0 = \frac{m_1 U_1 + m_2 U_2}{m_1 + m_2}, \tag{2.104}$$

and relative velocity $V = U_1 - U_2$. The composite velocity can be written as a function of relative velocity and composite velocity to obtain To obtain relations for U_0 and V to U_1, we start with the above momentum equation and add a $m_2 U_1$ term to both sides to obtain

$$(m_1 + m_2)\, U_1 + m_2 U_2 = m_2 U_1 + (m_1 + m_2)\, U_0, \tag{2.105}$$

which after grouping like terms becomes

$$(m_1 + m_2)\, U_1 = m_2\, (U_1 - U_2) + (m_1 + m_2)\, U_0, \tag{2.106}$$

and simplifies to

$$U_1 = U_0 + \frac{m_2}{m_1 + m_2} V = U_0 + \frac{N_0 - M_0}{L_0 - 2M_0 + N_0} V. \tag{2.107}$$

Similarly, we obtain

$$U_2 = U_0 - \frac{m_1}{m_1 + m_2} V = U_0 - \frac{L_0 - M_0}{L_0 - 2M_0 + N_0} V. \tag{2.108}$$

To substitute these expressions for U_1 and U_2 into the Eqn. 2.96, we begin with

$$\begin{aligned} 2E_k &= L_0 \left(U_0^2 + \frac{2 m_2 U_0 V}{m_1 + m_2} + \frac{m_2^2 V^2}{(m_1 + m_2)^2} \right) \\ &- 2M_0 \left(U_0^2 - \frac{m_1 U_0 V}{m_1 + m_2} + \frac{m_2 U_0 V}{m_1 + m_2} - \frac{m_1 m_2 V^2}{(m_1 + m_2)^2} \right) \\ &+ N_0 \left(U_0^2 - \frac{2 m_1 U_0 V}{m_1 + m_2} + \frac{m_1^2 V^2}{(m_1 + m_2)^2} \right), \end{aligned}$$

which can be factored into

$$\begin{aligned} 2E_k &= (L_0 - 2M_0 + N_0)\, U_0^2 \\ &+ 2\,(L_0 m_2 + M_0 m_1 - M_0 m_2 - N_0 m_1)\,\frac{U_0 V}{m_1 + m_2} \\ &+ \left(L_0 m_2^2 + 2M_0 m_1 m_2 + N_0 m_1^2\right)\frac{V^2}{(m_1 + m_2)^2}. \end{aligned}$$

Substituting $m_1 = L_0 - M_0$ and $m_2 = N_0 - M_0$, we obtain

$$\begin{aligned} 2E_k &= (L_0 - 2M_0 + N_0)\, U_0^2 \\ &+ 2(L_0(N_0 - M_0) + M_0(L_0 - M_0) - M_0(N_0 - M_0) \\ &- N_0(L_0 - M_0))\frac{U_0 V}{L_0 - 2M_0 + N_0} \\ &+ (L_0(N_0 - M_0)^2 + 2M_0(L_0 - M_0)(N_0 - M_0) \\ &+ N_0(L_0 - M_0)^2)\frac{V^2}{(L_0 - 2M_0 + N_0)^2}, \end{aligned}$$

which, since the product of the second term is zero, reduces to

$$2E_k = (L_0 - 2M_0 + N_0)\, U_0^2 + \frac{L_0 N_0 - M_0^2}{L_0 - 2M_0 + N_0} V^2. \tag{2.109}$$

The term associated with the composite average velocity U_0 will not contribute to coalescence. The kinetic energy that is relevant to coalescence is due to the energy associated with the relative velocity

$$(E_k)_{\text{coalescence}} = \frac{1}{2}\frac{L_0 N_0 - M_0^2}{L_0 - 2M_0 + N_0} V^2 = C_{\text{vm}} \left(\frac{\pi \rho_{\text{f}}}{6}\right) d_{\text{eq}}^3 \left(\frac{V}{2}\right)^2, \tag{2.110}$$

where C_{vm} is an added mass coefficient defined as

$$C_{\text{vm}} = \frac{12}{\pi \rho_{\text{f}} d_{\text{eq}}^3} \frac{L_0 N_0 - M_0^2}{L_0 - 2M_0 + N_0}, \tag{2.111}$$

where d_{eq} is the "equivalent" diameter defined as

$$d_{\text{eq}} = \frac{2 d_1 d_2}{d_1 + d_2}. \tag{2.112}$$

2.3.11 Interaction time

The expression for bubble-bubble interaction time is determined from energy conservation [48]. The energy conservation during collision includes the change in kinetic and surface energy of the bubbles is described by

$$E_{k,0} = E_k + \Delta F, \tag{2.113}$$

where $E_{k,0}$ is the kinetic energy when the bubbles first touch and the expression for ΔF, the change in surface energy, is

$$\Delta F = \sigma \Delta A \approx \pi \sigma \frac{z^2}{2} \tag{2.114}$$

for spherical particles, where z is the bubble deformation distance, with the distance between two bubble centers equal to $R_1 + R_2 - z$. Substituting for kinetic energy gives

$$C_{\mathrm{vm}} \left(\frac{\pi \rho_{\mathrm{f}}}{6}\right) d_{\mathrm{eq}}^3 \left(\frac{V_0}{2}\right)^2 = C_{\mathrm{vm}} \left(\frac{\pi \rho_{\mathrm{f}}}{6}\right) d_{\mathrm{eq}}^3 \left(\frac{V}{2}\right)^2 + \pi \sigma \frac{z^2}{2}, \tag{2.115}$$

where V_0 is the relative velocity V when the bubbles first touch. During collision it is assumed that $z \ll R_1 + R_2$ so that the added mass coefficient C_{vm} is constant during the collision process. With some algebra, the relative velocity during collision is

$$V = \frac{\mathrm{d}z}{\mathrm{d}t} = V_0 \sqrt{1 - \frac{12\ \sigma\ z^2}{C_{\mathrm{vm}}\ \rho_{\mathrm{f}}\ d_{\mathrm{eq}}^3 V_0^2}}. \tag{2.116}$$

This term can be integrated to obtain the interaction time t_i during the bubble-bubble collision. The interaction time is defined as the difference between the time the bubbles first touch ($z = 0$) to when they begin to separate ($\mathrm{d}z/\mathrm{d}t = 0$) [48]. By setting Eqn. 2.116 to zero, the distance z^* (where $\mathrm{d}z/\mathrm{d}t = 0$) can be obtained as

$$z^* = \sqrt{\frac{\rho_{\mathrm{f}}\ C_{\mathrm{vm}}\ d_{\mathrm{eq}}^3 V_0^2}{12\sigma}}. \tag{2.117}$$

We can rearrange the energy conservation equation into integral form to obtain

$$\int_0^{z^*} \frac{\mathrm{d}z}{V_0\sqrt{1-\frac{12\sigma z^2}{C_{\mathrm{vm}}\rho_{\mathrm{f}}d_{\mathrm{eq}}^3V_0^2}}} = \int_0^{t_i} \mathrm{d}t = t_i \tag{2.118}$$

The analytical solution for an integral of the form

$$\int_a^b \frac{1}{\sqrt{1-cz^2}}\mathrm{d}z = \left.\frac{\sin^{-1}\left(\sqrt{c}z\right)}{\sqrt{c}}\right|_a^b \tag{2.119}$$

Evaluating this expression gives

$$t_i = \frac{1}{V_0\sqrt{c}}\sin^{-1}(1), \tag{2.120}$$

where

$$c = \frac{12\ \sigma}{\rho_{\mathrm{f}}C_{\mathrm{vm}}\ d_{\mathrm{eq}}^3V_0^2}, a = 0, b = \sqrt{\frac{\rho_{\mathrm{f}}\ C_{\mathrm{vm}}\ d_{\mathrm{eq}}^3V_0^2}{12\ \sigma}} = \frac{1}{\sqrt{c}}, \tag{2.121}$$

which simplifies to

$$t_i = \frac{\pi}{4}\sqrt{\frac{\rho_{\mathrm{f}}\ C_{\mathrm{vm}}\ d_{\mathrm{eq}}^3}{3\sigma}}. \tag{2.122}$$

2.3.12 Drainage time

From Chesters [51], the drainage time is defined as the length of time from when the pressure at the film center between two bubbles equals $2\sigma/d_{\mathrm{eq}}$ until film rupture. The collision Weber number ($\mathrm{We}_{\mathrm{eq}}$) and Reynolds number ($\mathrm{Re}_{\mathrm{eq}}$) are defined as

$$\mathrm{We}_{\mathrm{eq}} \equiv \frac{\rho_{\mathrm{f}}V_0^2d_{\mathrm{eq}}}{2\sigma}, \quad \mathrm{Re}_{\mathrm{eq}} \equiv \frac{V_0d_{\mathrm{eq}}}{\nu_{\mathrm{f}}}.$$

Assuming $\mathrm{We}_{\mathrm{eq}} \ll 1$, the drainage time is then

$$t_d = \frac{\rho_{\mathrm{f}}V_0d_{\mathrm{eq}}^2}{8\sigma}. \tag{2.123}$$

Also, numerical results by Chesters and Hofman [52] showed that t_d varies as $\rho_{\mathrm{f}}V_0d_{\mathrm{eq}}^2/\sigma$ and t_i varies as $\sqrt{\rho_{\mathrm{f}}d_{\mathrm{eq}}^3}/\sigma$, therefore t_d/t_i varies as $\sqrt{\mathrm{We}_{\mathrm{eq}}}$. In combining the expressions

for t_i and t_d (Eqns. 2.122 and 2.123), we obtain

$$\frac{t_d}{t_i} \propto \frac{1}{2\pi}\sqrt{\frac{3\rho_{\mathrm{f}}V_0^2 d_{\mathrm{eq}}}{C_{\mathrm{vm}}\sigma}} = \frac{1}{2\pi}\sqrt{\frac{6\mathrm{We}_{\mathrm{eq}}}{C_{\mathrm{vm}}}}. \tag{2.124}$$

Since t_d/t_i was shown to vary with $\sqrt{\mathrm{We}_{\mathrm{eq}}}$, the coefficient k_1 is defined to give

$$\frac{t_d}{t_i} = \frac{k_1}{2\pi}\sqrt{\frac{6\mathrm{We}_{\mathrm{eq}}}{C_{\mathrm{vm}}}}. \tag{2.125}$$

The coefficient k_1 was found to be equal to 2.5 when comparing to experimental results of a single bubble coalescing with a free surface [53]. The theoretical coalescence probability of two bubbles traveling along their line of centers is then given by

$$P_{\mathrm{c}} = \begin{cases} 0 \text{ if } t_d < t_i \\ 1 \text{ if } t_d > t_i. \end{cases} \tag{2.126}$$

In practice, the collisions will not always be along line of centers and a smooth, semi-empirical function [54] is used to describe the coalescence probability

$$P_{\mathrm{c}} \approx \exp\left(-\frac{t_d}{t_i}\right). \tag{2.127}$$

Once a collision has been determined to occur, the coalescence probability is calculated and a random number x_{ran} (uniformly distributed from $[0-1]$) is generated. Whether or not coalescence has occurred for each collision is then given by

If $(x_{\mathrm{ran}} < P_{\mathrm{c}})$	$\rightarrow$	coalescence occurs
Else	$\rightarrow$	coalescence does not occur.

2.3.13 Collision, no coalescence

If it has been determined that the bubbles will collide but not coalesce, an instantaneous hard-sphere collision is assumed to have occurred (assuming that t_i is very small). With this assumption, the normal velocity after collision becomes $V = -V_0$ from conservation of kinetic energy. In the case of two bubbles moving along line of centers in a potential flow, this velocity would increase as the two bubbles move apart. However, we assume

that the external forces on the bubble due to the surrounding turbulent flow has a greater affect on bubble motion than the change in the effective coefficient of added mass. The bubble velocities immediately after collision are then

$$u_{1,N} = U_0 + \frac{N_0 - M_0}{L_0 - 2M_0 + N_0} V, \quad u_{2,N} = U_0 - \frac{L_0 - M_0}{L_0 - 2M_0 + N_0} V$$

and

$$\vec{u}_1 = \vec{u}_{1,T} + u_{1,N}\hat{n}_{1,2}, \quad \vec{u}_2 = \vec{u}_{2,T} + u_{2,N}\hat{n}_{1,2}.$$

2.3.14 Collision, with coalescence

If the binary collision results in coalescence, the two bubbles merge into one. Once this has been determined to happen, the parameters of the resulting bubble must be determined. The "new" bubble is now defined with subscript "3." The resulting bubble radius is obtained from mass conservation to be

$$R_3 = \left(R_1^3 + R_2^3\right)^{1/3}. \tag{2.128}$$

The total momentum is conserved from before and after coalescence. The bubble and the surrounding fluid around a bubble have momentum that is proportional to the bubble volume and velocity. Assuming that the momentum when the two bubbles are far apart is equal to the momentum when the two bubbles coalesce, the expression for the new bubble velocity is

$$\vec{v}_3 = \frac{\vec{v}_1 R_1^3 + \vec{v}_2 R_2^3}{R_3^2}. \tag{2.129}$$

Similarly, the bubble position is weighted by each bubble's volume at the moment of coalescence to obtain

$$\vec{Y}_3 = \frac{\vec{Y}_1 R_1^3 + \vec{Y}_2 R_2^3}{R_3^2}. \tag{2.130}$$

After these terms have been updated, the collision list is updated and the simulation advances as normal.

Chapter 3

Bubble migration in a turbulent boundary layer

3.1 Introduction

A canonical configuration to study micro-bubble viscous drag reduction (BDR) for marine applications involves the injection of air bubbles into a horizontal turbulent channel or flat-plate boundary layer. As the bubbles travel downstream, the bubbles in the near–wall region modify the near–wall momentum transport, and therefore drag. A comprehensive review of the earliest work has been compiled by Merkle and Deutsch [55] and a review of recent work on BDR and other forms of skin-friction drag reduction has been published by Ceccio [5]. BDR is measured by the ratio of skin-friction coefficient of the bubbly flow (C_f) to the skin-friction coefficient without bubbles ($C_{f,0}$). The mechanisms of BDR, though still not completely understood, are thought to be due to the modification of the near-wall density, viscosity and turbulent flow by the bubbles. Experiments by Madavan et al. [56] achieved values of BDR up to $\sim 80\%$ and found that BDR increased with increasing gas flow rates and decreasing free-stream flow rates. BDR was found to persist for as much as 70 boundary layer thicknesses downstream of injection. Gabillet et al. [57] found that the injection of bubbles increased the turbulent kinetic energy in the region of bubble injection and the void fraction profiles were nearly

self-similar. Recent work by Jacob et al. [58] obtained BDR using small bubbles and found that even for low bulk bubble concentrations ($C_{\text{bulk}} = 0.001$), modification of the turbulent flow by the bubbles was significant downstream of injection in the near-wall region. Sanders et al. [2] performed experiments investigating BDR in a high Reynolds number, spatially-evolving turbulent boundary layer on a large flat plate ($L = 12.9\text{m}$) in a plate-on-top configuration and found that BDR, though effective near the bubble injection location, lost its effectiveness far downstream from injection.

At large distances downstream from injection, the bubbles migrate away from the wall and drag reduction is lost [2], making BDR inefficient for large-scale vessels. A reduction of the effectiveness of BDR downstream of injections was also seen by Madavan et al. [56] though BDR was not completely lost due to the length of the test section. Examination of the bubble void fraction downstream of injection by Pal et al. [59] found that the bubble void fraction became more disperse with increasing distance, indicating that the bubbles tended to move away from the wall as they traveled downstream. This bubble migration away from the wall has been found to be the cause for loss of BDR [2]. Much of the work using DNS to simulate this flow has focused on the mechanisms of BDR [24, 60–62]. However, the mechanisms of bubble dispersion away from the wall are not sufficiently understood. The mechanisms of bubble dispersion have been recently investigated by Mattson and Mahesh [37] and Mattson and Mahesh [63], and this chapter summarizes their work.

Gabillet et al. [57] derived a model for bubble dispersion using a turbulent boundary layer profile, although the equations were laminar and assumed a fluid acceleration of zero. Sanders [64] also used a similar approach but included a laminar equation for the fluid acceleration in a turbulent boundary layer. Although these models gave the correct qualitative behavior of bubble diffusion away from the wall, accounting for the turbulent fluctuations on the bubble dispersion is important and, to our knowledge, this subject has not been directly addressed.

3.2 Computational and Physical Parameters

Sanders et al. [2] performed experiments investigating BDR in a high Reynolds number, spatially-evolving turbulent boundary layer on a large flat plate ($L = 12.9$m). These experiments were performed in the plate-on-top configuration, where the buoyancy force is acting to push the bubbles towards the wall. Figure 2 shows the typical bubble behavior in this experiment. Bubble size distributions and bubble-to-fluid area ratio were also measured at two downstream locations ($x = X_1, X_2$). Increasing the air flow-rate of injection, Q_a, and/or reducing free-stream velocity, U_e, increased BDR. For cases with the lowest free-stream velocity, the bubbles coalesced into a continuous layer of gas and drag reduction was maintained far downstream. For all other free-stream speeds and air-injection rates, the skin-friction drag was reduced downstream ($C_f/C_{f,0} < 1$) of the bubble injection location, but increased with downstream distance and approached single-phase levels ($C_f/C_{f,0} \to 1$). In these experiments, the near-wall bubble concentration became more dilute with downstream distance and eventually a bubble-free liquid layer formed near the wall.

For the low air-injection rate ($Q_\mathrm{a} = 0.05$ m^{3}s^{-1}) and high flow speed ($U_\mathrm{e} > 18$ ms^{-1}) in the Sanders et al. [2] experiments, the skin-friction reduction as compared to the single-phase case was very small ($C_f/C_{f,0} > 0.95$) for small distances downstream ($x < 2$ m) and approached single-phase results further downstream. This experiment will now be defined as case S1.

Due to the large Reynolds numbers in this turbulent boundary layer ($Re_\theta > 15,000$), providing sufficient resolution of the turbulent flow with DNS is prohibitively expensive. The Reynolds number of the boundary layer is reduced ($420 < Re_\theta < 1800$) in simulations while matching the ratio of mean bubble injection radius to boundary layer size at injection. For experiment S1, the mean bubble radius and boundary layer thickness were measured at downstream station X_1. The mean bubble diameter at $x = X_1$ was 230μm. Assuming a constant bubble radius and using a power law to estimate boundary layer thickness, the ratio of bubble size to boundary layer thickness at injection is obtained ($R_\mathrm{inj}/\delta_{99,\mathrm{inj}} \approx 0.0064$) and matched in the simulation. The Froude number based on the boundary layer thickness at injection ($\mathrm{Fr} = U_\mathrm{e}/\sqrt{g_y \delta_{99,\mathrm{inj}}}$) is 46. The distance between

TABLE 3.1: Simulation Parameters

Case	$L_x \times L_y \times L_z$	$N_x \times N_y \times N_z$
bubbly flow	$40 \times 3.12 \times 1.57$	$1600 \times 132 \times 256$
inflow gen.	$10 \times 3.12 \times 1.57$	$100 \times 45 \times 64$

X_1 and X_{inj}, non-dimensionalized by the boundary layer thickness (δ_{99}) at injection, is 35.6. The outflow of the bubble simulation is located at $(x - X_{\text{inj}})/\delta_{99,\text{inj}} = 67$. The bubble injection velocity is zero in the streamwise and spanwise directions and the wall normal injection velocity, v_y/U_{e}, is 0.55, as given in the Sanders [64] model of bubble diffusion in a turbulent boundary layer. The bubbles are modeled as massless spheres with a constant size.

A separate simulation is required to provide the necessary inflow turbulence for the spatially-evolving turbulent boundary layer simulation. The inflow-generation simulation applies rescaling to the streamwise boundary conditions [65] to obtain turbulent boundary layer flow in a reasonably-sized domain. A velocity plane from the inflow simulation is then interpolated to the inflow plane of the bubbly-flow simulation. The domain lengths (L) and number of control volumes (N) in the x (streamwise), y (wall-normal) and z (spanwise) directions are given in Table 1. The bulk Reynolds number, $\text{Re} = U_{\text{e}} L_{\text{ref}}/\nu$ is equal to 14000, with $U_{\text{e}} = U_{\text{ref}} = 1$ and $L_{\text{ref}} = \delta_{99,\text{inj}}/0.52 = 1$. At the inflow of the inflow generation simulation, the Reynolds number based on the momentum thickness (Re_θ) is 420, while at the inflow of the bubbly-flow domain, the Reynolds number $Re_\theta = 600$ and $Re_\theta = 1800$ at the outflow. The grid spacing is uniform in the streamwise and spanwise directions and non-uniform in the wall-normal direction. For the bubbly-flow domain, $\Delta y_{\text{min}} = 5.07 \times 10^{-4}$, with $\Delta y^+_{\text{min}} = 0.31$ and 13 control volumes are within $\Delta y^+ < 10$ at $(x - X_{\text{inj}})/\delta_{99,\text{inj}} = 45.4$. For the inflow-generation domain, $\Delta y_{\text{min}} = 1.96 \times 10^{-3}$, with $\Delta y^+_{\text{min}} = 1.38$ and 6 control volumes are within $\Delta y^+ < 10$ at $(x - X_{\text{inj}})/\delta_{99,\text{inj}} = -9.6$.

The inflow-generation simulation was initialized from a previous boundary layer simulation and run for $t^* = tU_{\text{e}}/L_{\text{ref}} = 420$ units of time to ensure removal of all transients, with a constant timestep of $\Delta t^* = 0.08$. Statistics were taken from $420 < t^* < 4400$, and the

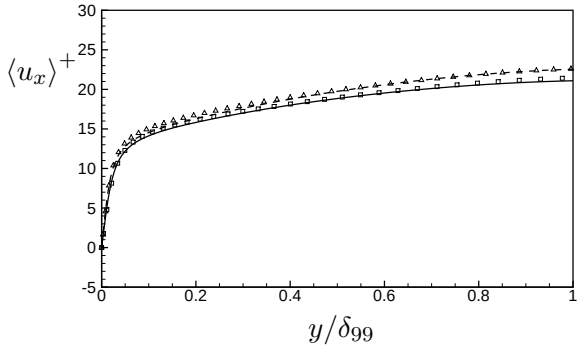

FIGURE 3.1: Comparison of mean streamwise velocity to results from the Simens et al. [66] simulation. —, DNS, ($\mathrm{Re}_\theta = 1100$); - -, DNS, ($\mathrm{Re}_\theta = 1551$); □, Simens, ($\mathrm{Re}_\theta = 1100$). △, Simens, ($\mathrm{Re}_\theta = 1551$).

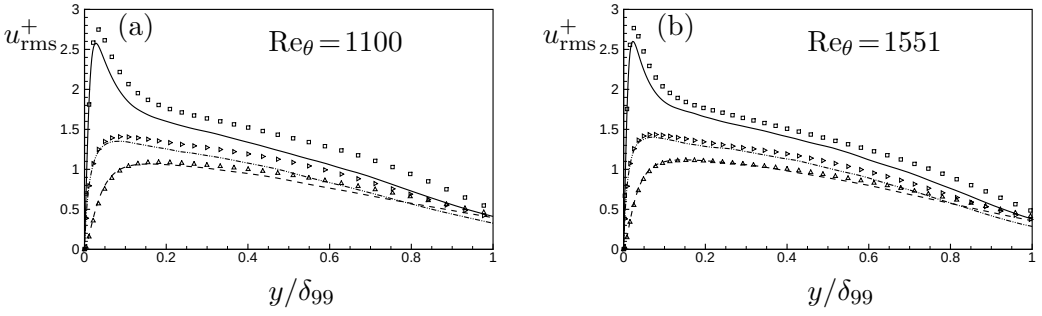

FIGURE 3.2: Comparison of turbulence intensities to results from the Simens et al. [66] simulation. (a) RMS of the turbulence intensities versus wall-normal distance for $\mathrm{Re}_\theta = 1100$. (b) RMS of the turbulence intensities versus wall-normal distance for $\mathrm{Re}_\theta = 1551$. —, $u^+_{x,\mathrm{rms}}$, DNS; - -, $u^+_{y,\mathrm{rms}}$, DNS; -···-, $u^+_{z,\mathrm{rms}}$, DNS; □, $u^+_{x,\mathrm{rms}}$, Simens; △, $u^+_{y,\mathrm{rms}}$, Simens; ▷, $u^+_{z,\mathrm{rms}}$, Simens.

velocity inflow plane and additional statistics were sampled from $4400 < t^* < 8900$. The bubbly-flow simulation was initialized from zero velocity and run for 1500 units of time to remove all transients, with $\Delta t^* = 0.015$. One-hundred bubbles were then injected every 10 fluid timesteps at a random spanwise location near the wall ($y_{\mathrm{inj}}/\delta_{99,\mathrm{inj}} = 2 \times 10^{-6}$). The bubble timestep $\Delta t^*_{\mathrm{bub}}$ was equal to 1.5×10^{-5}. Fluid statistics and bubble statistics were sampled from $1500 < t^* < 2100$ until convergence was achieved.

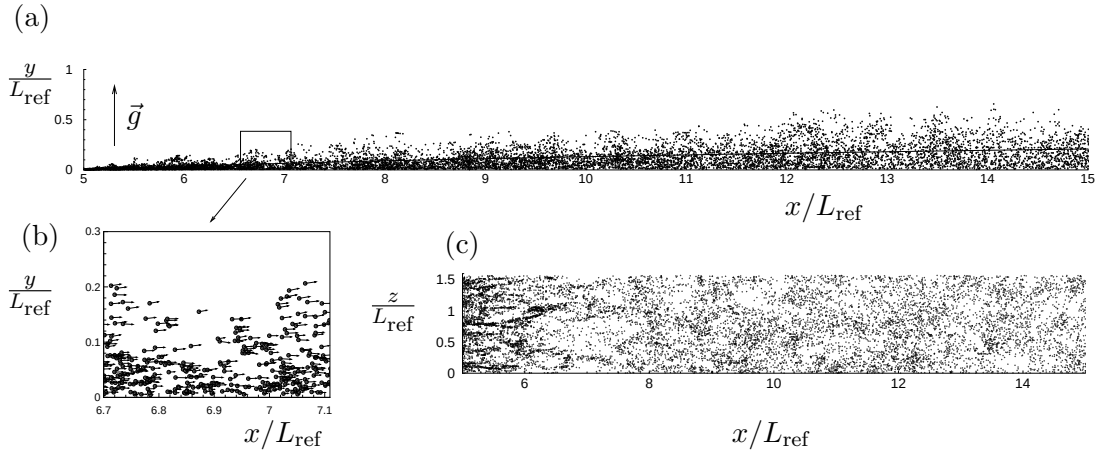

FIGURE 3.3: Instantaneous bubble position with only a part of the domain shown ($5 < x < 15$). (a) Bubble position in streamwise and wall-normal coordinates with ensemble-averaged position $\langle Y_y \rangle_{\mathrm{e}}$ vs. $\langle Y_x \rangle_{\mathrm{e}}$ shown by the black line. (b) Close-up view of (a) along with bubble velocity vectors (v_x, v_y). (c) Bubble position in streamwise and spanwise coordinates.

3.3 Results

3.3.1 Carrier-phase Turbulence

Results for the carrier-phase turbulent flow in the bubbly-flow simulation are given in Figures 3 and 4. The results shown are taken from two streamwise locations, one at $\mathrm{Re}_\theta = 1100$ and another at $\mathrm{Re}_\theta = 1551$. The wall-normal distance is non-dimensionalized by the boundary layer thickness, δ_{99}, at each streamwise location. The carrier flow shows good agreement with results from Simens et al. [66] for both the mean flow and turbulence intensities.

3.3.2 Bubble Trajectories

After injection, the bubbles tend to disperse and travel away from the wall, as shown in the instantaneous snapshots of bubble position in Figure 5. Note that near the injection, the bubbles are concentrated into filament-like structures that break down with increasing downstream distance. Through the force due to the fluid acceleration, bubbles are pushed toward the centers of vortex cores. This preferential concentration of bubbles

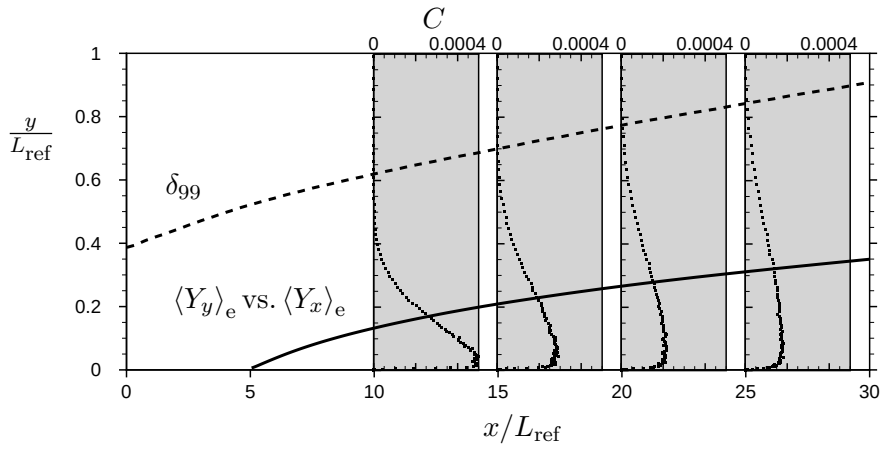

FIGURE 3.4: Ensemble-averaged bubble trajectory and evolution of boundary layer thickness, along with bubble concentration profiles. Bubble concentration C is plotted versus y/L_{ref} at $x/L_{\mathrm{ref}} = 10, 15, 20$ and 25. - -, δ_{99}; —, $\langle Y_y \rangle_{\mathrm{e}}$ vs. $\langle Y_x \rangle_{\mathrm{e}}$; ■, C.

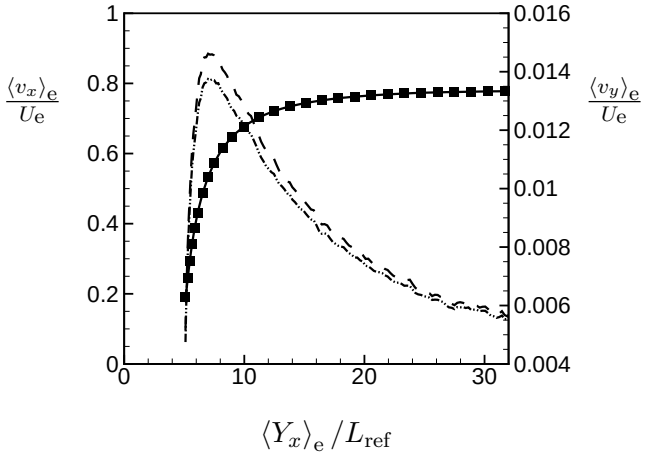

FIGURE 3.5: Ensemble-averaged bubble and carrier-fluid velocities. —, $\langle v_x \rangle_{\mathrm{e}}$; - - -, $\langle v_y \rangle_{\mathrm{e}}$; ■, $\langle u_x \rangle_{\mathrm{e}}$; -·-·-, $\langle u_y \rangle_{\mathrm{e}}$.

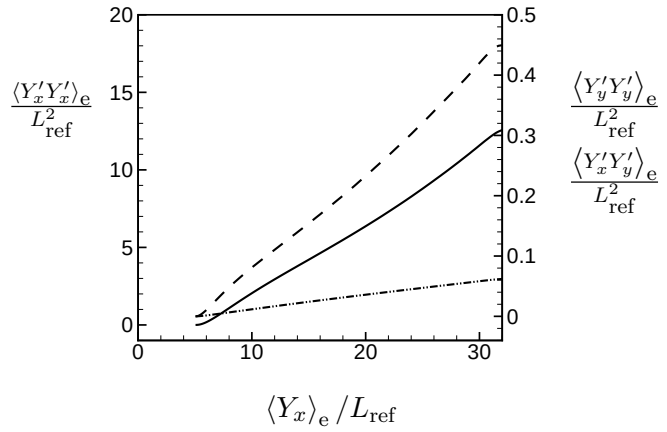

FIGURE 3.6: Ensemble-averaged position fluctuations. —, $\langle Y_x' Y_x' \rangle_e$; - -, $\langle Y_y' Y_y' \rangle_e$; -·-·-, $\langle Y_x' Y_y' \rangle_e$.

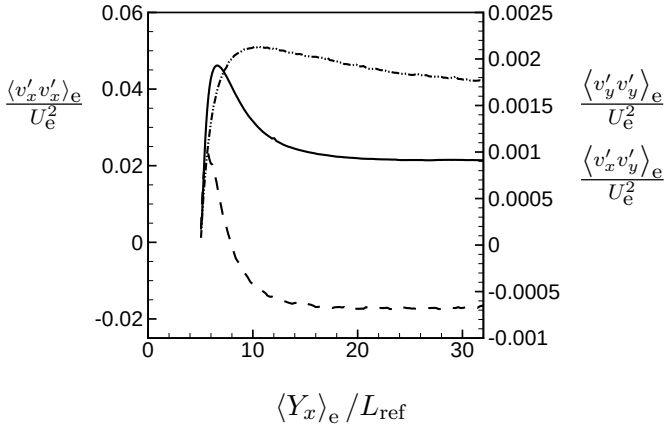

FIGURE 3.7: Ensemble-averaged velocity fluctuations. —, $\langle v_x' v_x' \rangle_e$; - -, $\langle v_y' v_y' \rangle_e$; -·-·-, $\langle v_x' v_y' \rangle_e$.

in vortex cores has been observed in previous simulations of bubbles in homogeneous, isotropic turbulence [67]. Near the wall in a turbulent boundary-layer flow, vortical structures that form the legs of hairpin structures are oriented in the streamwise direction [68]. The tendency of bubbles to form filament-like structures observed in Figure 5c is due to the attraction of the bubbles to the streamwise vortical structures. The bubbles tend to travel away from the wall as they move downstream, as observed in Sanders et al. [2].

An ensemble-average is obtained by a number average performed over all bubbles. The ensemble-average is a function of the residence time of a bubble in the flow after injection

($t_\mathrm{r} = t - t_\mathrm{inj}$). In this paper, ensemble-averaged bubble quantities are denoted by the subscript 'e'. The ensemble average of f at time t_r is given by

$$\langle f(t_\mathrm{r})\rangle_\mathrm{e} = \frac{1}{N}\sum_{i=1}^{N} f(t_\mathrm{r}), \tag{3.1}$$

where $\langle f(t_\mathrm{r})\rangle_\mathrm{e}$ is sampled over N number of bubbles. Sampling of quantities for the ensemble average were performed at discrete lengths of residence time after injection (i.e. $t_\mathrm{r} = n\Delta t_\mathrm{r}$ for $n = 1, 2, 3, ...$), where $\Delta t_\mathrm{r} = 120\Delta t$. This time interval Δt_r was chosen to obtain samples at a quick enough rate to resolve bubble behavior but not so often as to become unnecessarily expensive to compute.

Figure 6 shows the ensemble-averaged bubble trajectory, with the tendency of the bubbles to travel away from the wall clearly evident. Figure 7 plots the ensemble-averaged bubble velocities as a function of ensemble-averaged streamwise position. The wall-normal velocity is positive (away from the wall) and approaches a constant value with increasing downstream distance. As the bubbles travel downstream, the streamwise velocity increases, due to the bubbles accelerating along with the fluid as they enter the higher-momentum flow away from the wall. The ensemble-averaged fluctuations of bubble position and velocity are plotted in Figures 8 and 9. Streamwise fluctuations are large as compared to wall-normal position fluctuations, due to the large velocity fluctuations along the streamwise direction. The fluctuations in position increase with downstream distance due to dispersion. The bubble velocity fluctuations increase to a maximum value just downstream of injection then decrease and approach a constant value as the bubble travels downstream.

3.3.3 Budgets of Bubble Acceleration

The mean acceleration $\langle d\vec{v}/dt\rangle_\mathrm{e}$ can be integrated to obtain the mean velocity $\langle\vec{v}\rangle_\mathrm{e}$ and integrated once again to give the mean position $\left\langle\vec{Y}\right\rangle_\mathrm{e}$, so understanding the forces on the bubble provides insight that can be used to predict bubble dispersion. The drag, lift, fluid acceleration and buoyancy terms in Eqn. 2.32 can be ensemble-averaged to obtain a budget of mean bubble acceleration. The equation for ensemble-averaged bubble

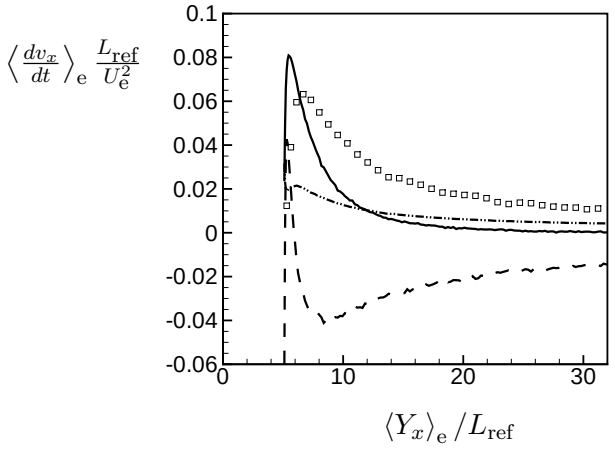

FIGURE 3.8: Ensemble-averaged bubble acceleration budget in the streamwise (x) direction. - -, $3\frac{Du_x}{Dt}$; □, Drag_x; -···-, Lift_x; —, Total_x.

acceleration is

$$\left\langle \frac{d\vec{v}}{dt} \right\rangle_e = \langle -2\vec{g} \rangle_e + \left\langle 3\frac{D\vec{u}}{Dt} \right\rangle_e + \left\langle \frac{3}{4}\frac{C_D}{R} |\vec{u} - \vec{v}| (\vec{u} - \vec{v}) \right\rangle_e + \langle 2C_L(\vec{u} - \vec{v}) \times \vec{\omega} \rangle_e . \quad (3.2)$$

Budgets of mean bubble acceleration as a function of distance downstream of injection for bubbles in the turbulent boundary layer are shown in Figures 10 and 11. Note that for the streamwise accelerations, the drag and lift contributions accelerate the bubble in the downstream direction while the fluid acceleration tends to slow the bubbles, except for a short period near injection where the fluid acceleration is positive. The drag acceleration is positive, therefore the difference in velocity in the streamwise direction, $\langle u_x \rangle_e - \langle v_x \rangle_e$, is greater than zero. The ensemble-averaged bubble acceleration is always positive and approaches zero for large distances downstream of injection.

Figure 11 plots the budgets of the ensemble-averaged accelerations in the wall-normal direction. From Figure 11a, it is clear the drag and fluid accelerations have the largest magnitudes. In the drag acceleration, the difference in velocity in the wall-normal direction, $\langle u_y \rangle_e - \langle v_y \rangle_e$, is less than zero, therefore the bubbles (in an ensemble-averaged sense) have a larger wall-normal velocity than the Eulerian fluid. Figure 11b plots the bubble acceleration in the wall-normal direction, with the drag and fluid acceleration

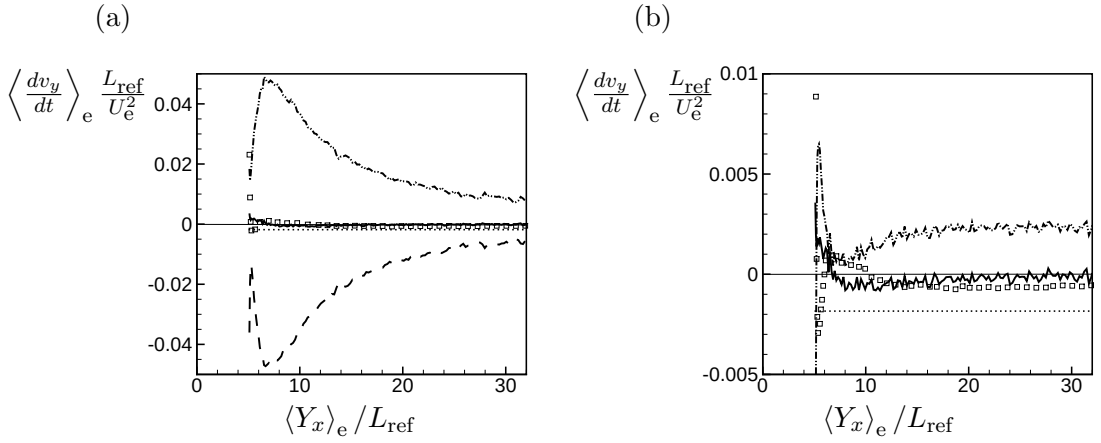

FIGURE 3.9: Ensemble-averaged bubble acceleration budget in the wall-normal (y) direction. (a) Normal view showing all terms individually. - -, Drag_y; -···-, $3\frac{Du_y}{Dt}$; □, Lift_y; · · ·, $-2g$; —, Total_y. (b) Zoomed-in view with the drag and fluid acceleration terms summed together. -···-, $(\text{Drag}_y + 3\frac{Du_y}{Dt})$; □, Lift_y; · · ·, $-2g$; —, Total_y.

terms summed together. The total sum of fluid and drag accelerations push the bubbles away from the wall. In Figure 11b, the bubble acceleration depends on distance from the injection location. Far downstream of injection, the lift acceleration and the sum of the fluid and drag acceleration is constant. The total bubble acceleration approaches zero. Near injection, the bubble acceleration terms vary with distance from injection location. The total acceleration is positive near injection and decreases with downstream distance, approaching zero for large downstream distances.

The ensemble-averaged terms of Eqn. 3.2 can be broken down into constituents of ensemble-averaged mean and fluctuating terms. For incompressible flow, the divergence of the fluid velocity is zero. It can be easily shown that when the carrier-phase velocity is broken into its mean and fluctuating terms, $u_i = \langle u_i \rangle_e + u_i^{'}$, the divergence of the mean and fluctuating terms are also zero.

Starting with the equation for the drag acceleration,

$$\left\langle \vec{A}_D \right\rangle_e = \left\langle \frac{3}{4} \frac{C_D}{R} \left| \vec{u} - \vec{v} \right| \left(\vec{u} - \vec{v} \right) \right\rangle_e , \tag{3.3}$$

the drag expression can be approximated by using only the 1st-order term for the drag coefficient, $C_D \sim 24/\text{Re}_b$, since $\text{Re}_b \sim 1$. This results in a simplification of the drag

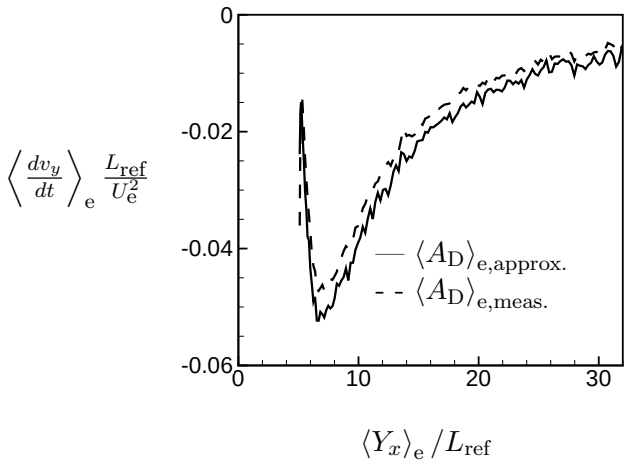

FIGURE 3.10: Comparison of drag acceleration in the wall-normal direction for the approximate equation and measured result.

acceleration to

$$A_{\mathrm{D},i} = \frac{9\nu}{R^2} \left(u_i - v_i \right). \tag{3.4}$$

If the bubble radius is constant, taking the ensemble average of the above expression results in

$$\left\langle \vec{A}_{\mathrm{D}} \right\rangle_{\mathrm{e,approx.}} = \frac{9\nu}{R^2} \left(\langle u_i \rangle_{\mathrm{e}} - \langle v_i \rangle_{\mathrm{e}} \right), \tag{3.5}$$

where only the mean quantities of velocity remain. Figure 12 plots the comparison of the results of Eqn. 3.5 to the measured ensemble-averaged acceleration in the y-direction. Good agreement between the approximate equation and measured quantities are obtained.

The ensemble-averaged fluid acceleration can be expanded to obtain

$$\langle A_{\mathrm{F},i} \rangle_{\mathrm{e}} = 3\frac{\partial \langle u_i \rangle_{\mathrm{e}}}{\partial t} + 3 \langle u_j \rangle_{\mathrm{e}} \frac{\partial \langle u_i \rangle_{\mathrm{e}}}{\partial x_j} + 3\frac{\partial}{\partial x_j} \left\langle u_i^{'} u_j^{'} \right\rangle_{\mathrm{e}}. \tag{3.6}$$

The contributions of the unsteady, mean and fluctuating terms in the fluid acceleration term are shown in Figure 13. The largest terms are the unsteady term $\partial \langle u_y \rangle_{\mathrm{e}} / \partial t$, which is positive, and the mean gradient term $\langle u_j \rangle_{\mathrm{e}} \partial \langle u_y \rangle_{\mathrm{e}} / \partial x_j$, though the fluctuating term also has a significant contribution. For the mean gradient, the $\langle u_x \rangle_{\mathrm{e}} \partial \langle u_y \rangle_{\mathrm{e}} / \partial x$

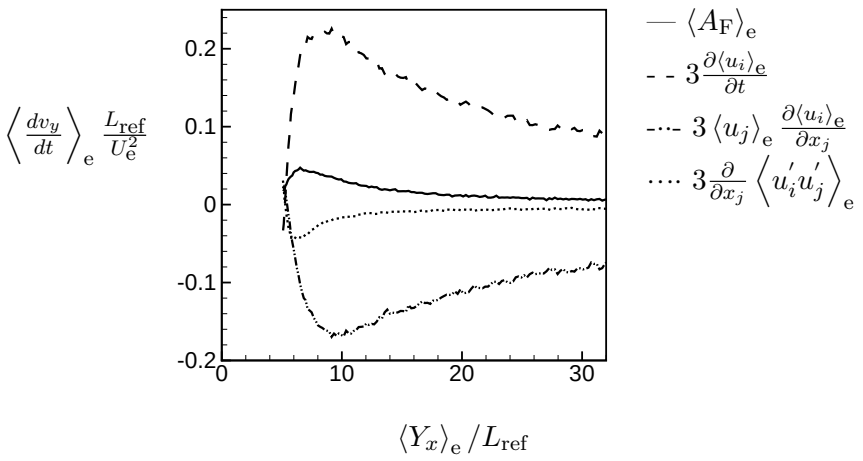

FIGURE 3.11: Budget of fluid acceleration in the y-direction.

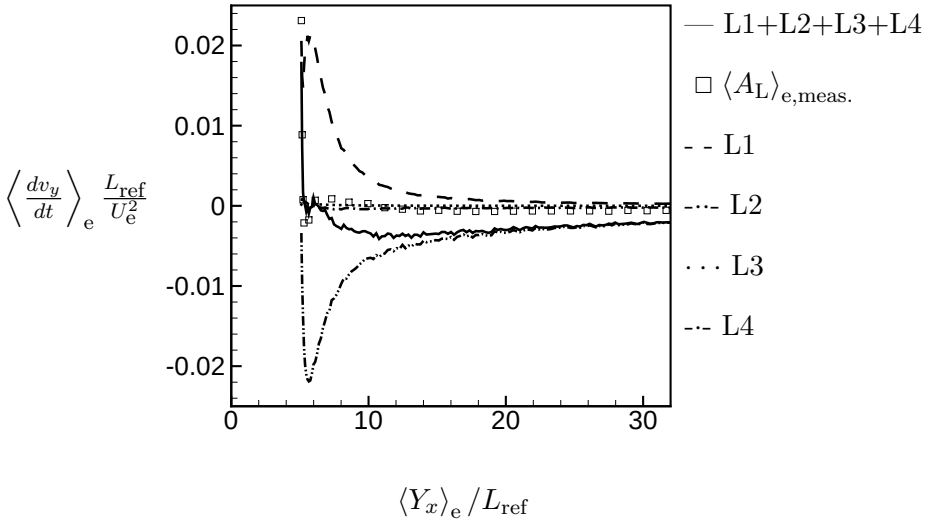

FIGURE 3.12: Budget of lift acceleration in the y-direction.

contribution is the largest and negative since $\partial \langle u_y \rangle_e / \partial x$ is negative due to boundary layer growth.

The lift acceleration is

$$\left\langle \vec{A}_L \right\rangle_e = \langle 2C_L(\vec{u} - \vec{v}) \times \vec{\omega} \rangle_e ,$$

and can also be factored into mean and fluctuating terms. The commutative property of the equation is applied to separate $\vec{u}$ and $\vec{v}$. By applying the vector cross product

identities

$$\begin{aligned}\vec{A}\times\left(\vec{\nabla}\times\vec{A}\right) &= \frac{1}{2}\vec{\nabla}\left(\vec{A}\cdot\vec{A}\right)-\left(\vec{A}\cdot\vec{\nabla}\right)\vec{A}\\ \vec{A}\times\left(\vec{\nabla}\times\vec{B}\right) &= \vec{\nabla}_B\left(\vec{A}\cdot\vec{B}\right)-\left(\vec{A}\cdot\vec{\nabla}\right)\vec{B},\end{aligned}$$

and taking the ensemble-average, the ensemble-averaged lift equation becomes

$$\begin{aligned}\frac{\left\langle\vec{A}_{\mathrm{L}}\right\rangle_{\mathrm{e}}}{\langle 2C_{\mathrm{L}}\rangle_{\mathrm{e}}} &= \frac{1}{2}\vec{\nabla}\left(\langle\vec{u}\rangle_{\mathrm{e}}\cdot\langle\vec{u}\rangle_{\mathrm{e}}\right)+\frac{1}{2}\vec{\nabla}\left(\left\langle\vec{u'}\cdot\vec{u'}\right\rangle_{\mathrm{e}}\right)-\left(\langle\vec{u}\rangle_{\mathrm{e}}\cdot\vec{\nabla}\right)\langle\vec{u}\rangle_{\mathrm{e}}-\left\langle\left(\vec{u'}\cdot\vec{\nabla}\right)\vec{u'}\right\rangle_{\mathrm{e}}\\ &- \vec{\nabla}_u\left(\langle\vec{v}\rangle_{\mathrm{e}}\cdot\langle\vec{u}\rangle_{\mathrm{e}}\right)-\vec{\nabla}_u\left(\left\langle\vec{v'}\cdot\vec{u'}\right\rangle_{\mathrm{e}}\right)+\left(\langle\vec{v}\rangle_{\mathrm{e}}\cdot\vec{\nabla}\right)\langle\vec{u}\rangle_{\mathrm{e}}+\left\langle\left(\vec{v'}\cdot\vec{\nabla}\right)\vec{u'}\right\rangle_{\mathrm{e}}.\end{aligned}$$

Assuming a constant lift coefficient of 1/2, this equation for lift can be simplified to give

$$\begin{aligned}\langle A_{\mathrm{L},i}\rangle_{\mathrm{e}} &= \langle u_j\rangle_{\mathrm{e}}\frac{\partial\langle u_j\rangle_{\mathrm{e}}}{\partial x_i}+\left\langle u_j^{'}\frac{\partial u_j^{'}}{\partial x_i}\right\rangle_{\mathrm{e}}-\langle u_j\rangle_{\mathrm{e}}\frac{\partial\langle u_i\rangle_{\mathrm{e}}}{\partial x_j}-\left\langle u_j^{'}\frac{\partial u_i^{'}}{\partial x_j}\right\rangle_{\mathrm{e}}\\ &- \langle v_j\rangle_{\mathrm{e}}\frac{\partial\langle u_j\rangle_{\mathrm{e}}}{\partial x_i}-\left\langle v_j^{'}\frac{\partial u_j^{'}}{\partial x_i}\right\rangle_{\mathrm{e}}+\langle v_j\rangle_{\mathrm{e}}\frac{\partial\langle u_i\rangle_{\mathrm{e}}}{\partial x_j}+\left\langle v_j^{'}\frac{\partial u_i^{'}}{\partial x_j}\right\rangle_{\mathrm{e}}.\end{aligned}\tag{3.7}$$

Taking the above equation, the last four terms are similar with respect to the first four, except for having a sign change and a substitution of the bubble velocity for the fluid velocity. These terms can be grouped together to more easily see the total contribution to the lift acceleration. The equation of the summed terms is now grouped into four terms:

$$\begin{aligned}\langle A_{\mathrm{L,i}}\rangle_{\mathrm{e}} &= \underbrace{\left(\langle u_j\rangle_{\mathrm{e}}-\langle v_j\rangle_{\mathrm{e}}\right)\frac{\partial\langle u_j\rangle_{\mathrm{e}}}{\partial x_i}}_{\mathrm{L1}}+\underbrace{\left\langle u_j^{'}\frac{\partial u_j^{'}}{\partial x_i}\right\rangle_{\mathrm{e}}-\left\langle v_j^{'}\frac{\partial u_j^{'}}{\partial x_i}\right\rangle_{\mathrm{e}}}_{\mathrm{L2}}\\ &+ \underbrace{\left(\langle v_j\rangle_{\mathrm{e}}-\langle u_j\rangle_{\mathrm{e}}\right)\frac{\partial\langle u_i\rangle_{\mathrm{e}}}{\partial x_j}}_{\mathrm{L3}}\underbrace{-\left\langle u_j^{'}\frac{\partial u_i^{'}}{\partial x_j}\right\rangle_{\mathrm{e}}+\left\langle v_j^{'}\frac{\partial u_i^{'}}{\partial x_j}\right\rangle_{\mathrm{e}}}_{\mathrm{L4}}.\end{aligned}\tag{3.8}$$

Figure 14 plots the summed contributions of each similar term to the total lift acceleration. The two largest terms are L1 and L2, with L3 and L4 being negligible. The sum of L1-L4 is given by the solid black line, and an independently measured ensemble-average

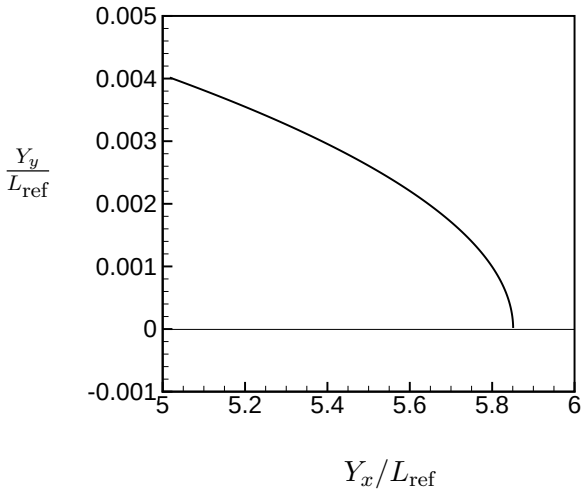

FIGURE 3.13: Bubble trajectory in the laminar boundary layer.

of the lift acceleration is given by open symbols. Even though there is some discrepancy in the lift acceleration budget to the total ensemble-averaged value of lift, it is clear that the terms L1 and L2 are the dominant contributors and Eqn. 3.7 can be reduced to

$$\langle A_{\mathrm{L,i}} \rangle_{\mathrm{e,\ approx.}} = \langle u_j \rangle_{\mathrm{e}} \frac{\partial \langle u_j \rangle_{\mathrm{e}}}{\partial x_i} + \left\langle u_j^{'} \frac{\partial u_j^{'}}{\partial x_i} \right\rangle_{\mathrm{e}} - \langle v_j \rangle_{\mathrm{e}} \frac{\partial \langle u_j \rangle_{\mathrm{e}}}{\partial x_i} - \left\langle v_j^{'} \frac{\partial u_j^{'}}{\partial x_i} \right\rangle_{\mathrm{e}} . \tag{3.9}$$

Through factoring out the mean and fluctuating terms in the ensemble-averaged accelerations and comparing budgets, the full equations can be reduced from their full form. For small Re_b, using only mean contributions to calculate the mean drag acceleration is appropriate. In the fluid acceleration term, the unsteady and mean convection terms are largest, though the fluctuating term is not negligible. The equation for lift can be simplified from the original eight terms to four. If the mean and fluctuating terms in the bubble acceleration equations can be modeled, the mean diffusion of the bubbles away from the wall can be determined over a range of Reynolds numbers.

3.3.4 Role of Turbulence: Bubbles in a Laminar Boundary Layer

Turbulence significantly affects bubble dispersion in a turbulent boundary layer. Without turbulence there is a lack of intermittency of the forces on the bubbles and no migration of bubbles away from the wall. To demonstrate this, a simulation with bubbles injected into a laminar boundary layer was performed. The outer scales were matched between the turbulent and laminar simulations at the injection location, with Re = 14000 and $R/\delta_{99,\mathrm{inj}} = 0.0064$. The bubble radius was kept constant throughout the simulation. A simulation domain of $L_x = 40, L_y = 3.12$ and $L_z = 1.57$ was used, with $N_x = 400, N_y = 45$ and $N_z = 64$. The grid was uniform in the streamwise and spanwise directions, but non-uniform in the wall-normal direction with the smallest wall-normal spacing near the wall. The simulation was initialized with the Blasius solution [69] and then advanced until the velocity field was converged. Good agreement between velocity field and Blasius solution was obtained.

In this laminar flow, the forces on the bubble are greatly simplified as compared to turbulent flow, with no fluctuating terms in the bubble acceleration equations. The bubble is injected with a positive wall-normal velocity and travels slightly into the boundary layer (Figure 15). The bubble penetrates only a small distance into the boundary layer due to drag and then travels towards the wall, opposite of what is seen in the turbulent case. Because the size of the bubble is on the same scale as the penetration distance, the simulation was allowed to continue to run without any particle-wall boundary conditions (such as bubble-wall collisions) until the bubble center reached the wall.

As seen in Figure 16, the forces on the bubble are constant throughout the bubble path, except very near injection where a large drag force quickly damps out the initial injection velocity of the bubble. This happens very quickly with respect to the other scales in the flow and is not shown in Figure 16 or the other figures of laminar flow. The lift force and fluid acceleration in the wall-normal direction are both zero and the drag exactly counterbalances the buoyancy force. The bubble has reached its terminal velocity according to the equation

$$\frac{dv_y}{dt} = -2g + \frac{3}{4}\frac{C_\mathrm{D}}{R}\left|\vec{u} - \vec{v}\right|\left(u_y - v_y\right), \tag{3.10}$$

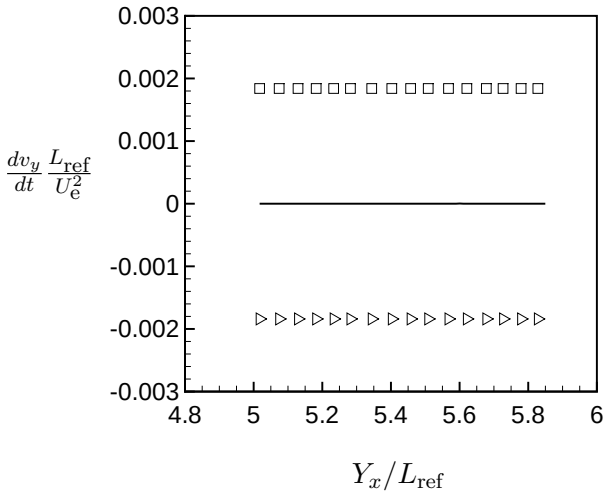

FIGURE 3.14: Bubble acceleration budget in the wall-normal (y) direction for the laminar boundary layer simulation. □, Drag_y; ▷, $-2g$; —, Total_y.

and since the terms on the right hand side balance each other at steady state and $C_{\rm D} \sim 24/\text{Re}_b$,

$$2g = \frac{9\nu}{R^2}\left(u_y - v_y\right), \tag{3.11}$$

and the bubble has a constant velocity in the wall normal direction of $v_y/U_{\rm e} = -3.1\times10^{-5}$, since $u_y \approx 0$ near the wall.

When comparing the turbulent and laminar boundary layer (LBL) simulations, there are large differences in the overall behavior of the bubbles. The mean trajectory of the LBL shows bubbles traveling towards the wall, while the turbulent boundary layer shows the bubbles dispersing away from the wall as they travel downstream. The influence of the injection velocity is weak in both simulations, as the drag force quickly damps out the initial injection velocity. At this Reynolds number, the injection velocity of the bubbles can be ruled out as a mechanism for bubble dispersion away from the wall.

The dispersion of bubbles away from the wall is directly dependent on the turbulence. In the LBL, the fluid acceleration in the wall-normal direction is zero, and the bubbles travel towards the wall due to buoyancy. In the TBL, the fluid acceleration is large and

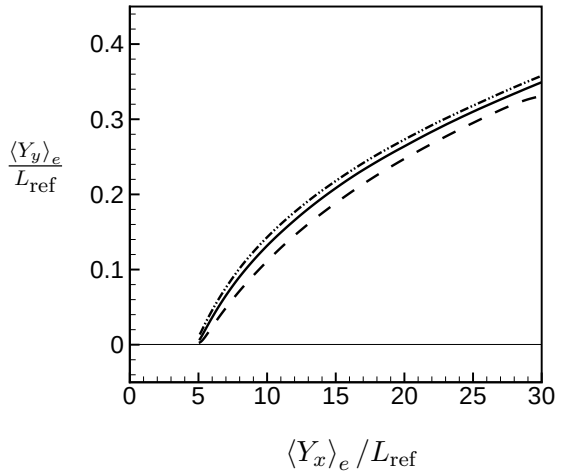

FIGURE 3.15: Bubble trajectories for 3 differently-sized bubbles in a turbulent boundary layer. - -, $R/\delta_{99,\text{inj}} = 0.0037$; —, $R/\delta_{99,\text{inj}} = 0.0064$; -···-, $R/\delta_{99,\text{inj}} = 0.0092$.

pushes the bubbles away from the wall. In comparing the TBL and LBL simulations, it is evident that the turbulent fluid acceleration is the mechanism for bubble diffusion.

3.3.5 Effect of Bubble Size

To determine the effect of bubble size, a simulation with 3 bubble sizes ($R = R_1, R_2, R_3$) was performed, with R_2 equal to the mean bubble radius in Sanders et al. [2] and R_1 and R_3 equal to $R_2 \pm \sigma_{\text{dev}}$, where σ_{dev} is the experimental standard deviation of bubble size measured at $x = \text{X}_1$. All other conditions were the same as the previous turbulent bubble simulation. The change in size is on the order of R_2, with $R_1/\delta_{\text{inj}} = 0.0037, R_2/\delta_{\text{inj}} = 0.0064$ and $R_3/\delta_{\text{inj}} = 0.0092$.

The trajectories of the bubbles are shown in Figure 17. The bubbles with the largest size penetrate farther into the turbulent boundary layer than smaller bubbles, due to an increased wall-normal velocity after injection. The mechanism for the enhanced movement away from the wall for larger bubbles is found by looking at the acceleration budget in the wall-normal direction. From the approximate drag equation (Eqn. 3.5), the drag acceleration is inversely proportional to R^2 and the larger bubbles initially have a reduced drag force and are less likely to follow the fluid flow. This leads to an increased

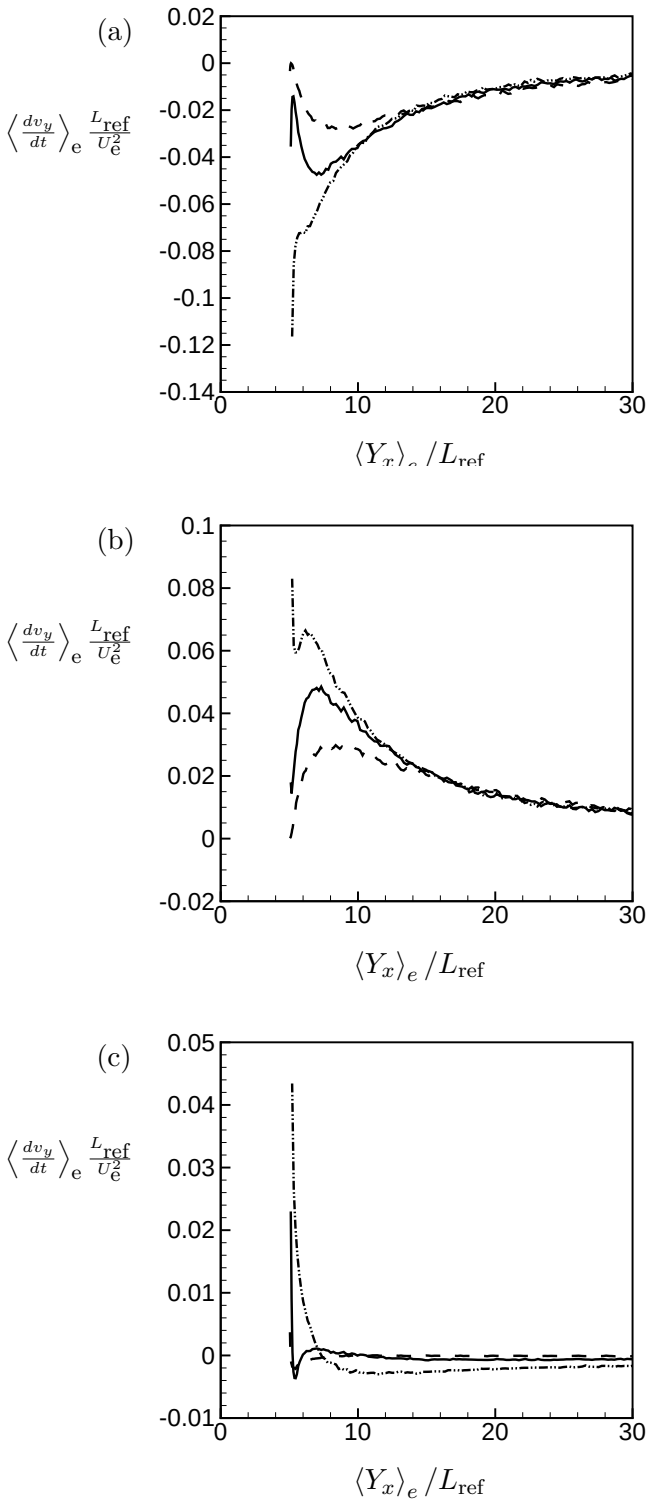

FIGURE 3.16: Bubble acceleration in the wall-normal direction for 3 differently-sized bubbles in a turbulent boundary layer, with (a) plotting the drag acceleration, (b) the fluid acceleration and (c) the lift acceleration. - -, $R/\delta_{99,\mathrm{inj}} = 0.0037$; —, $R/\delta_{99,\mathrm{inj}} = 0.0064$; -···-, $R/\delta_{99,\mathrm{inj}} = 0.0092$.

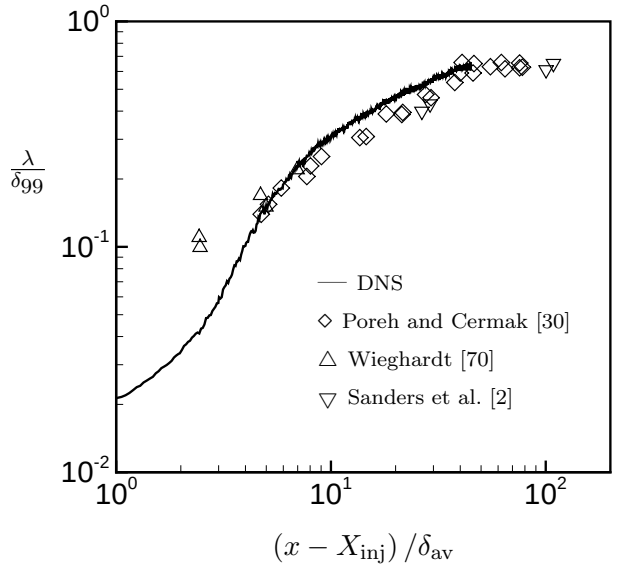

FIGURE 3.17: Diffusion of a passive scalar and bubbles in a turbulent boundary layer.

relative velocity, which increases the lift and drag accelerations overall (Figures 18a and 18c). The fluid acceleration also increases for larger bubbles, due to an increase in the unsteady velocity contribution (Figure 18b). The larger bubbles are moving upward into higher-momentum flow more quickly than smaller bubbles, therefore $\partial \langle u_y \rangle_e / \partial t$ is increased. Altogether, this leads to an ensemble-average path that is farther away from the wall for larger bubbles than smaller bubbles.

3.3.6 Comparison to a Passive Scalar

Poreh and Cermak [30] investigated the diffusion of a passive scalar by injecting ammonia gas into a turbulent boundary layer of air and then measuring the scalar concentration downstream of injection. As the gas traveled downstream with the flow, the mean concentration of ammonia decreased near the wall. Except very near the wall, this behavior is similar to what is seen for bubbles injected into a turbulent boundary layer, even though the bubbles are not passive scalars.

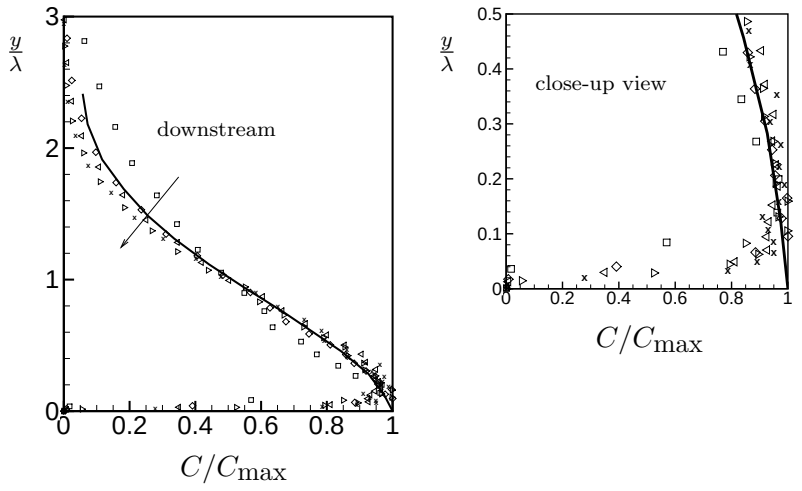

FIGURE 3.18: Concentration profiles for a passive scalar and bubbles in the intermediate zone of a turbulent boundary layer, with the inset figure plotting a near-wall close-up view. $x/\mathrm{L_{ref}} = (7.5, 9.4, 11.2, 13.1, 15.0) = (\square, \diamond, \triangleleft, \triangleright, \mathrm{x})$. —, Poreh and Cermak [30] intermediate zone.

Poreh and Cermak [30] defined two length scales, δ_{av} and λ, with δ_{av} based on the local boundary layer thickness and λ being the wall-normal position where the time-averaged concentration was equal to one half of the maximum concentration at that streamwise location, $C(\lambda) = 1/2\ C_{\mathrm{max}}$. The passive scalar data was found to behave differently in four zones that are defined as a function of $(x - X_{\mathrm{inj}})/\delta_{\mathrm{av}}$. The initial zone is near injection, $(x - X_{\mathrm{inj}})/\delta_{\mathrm{av}} \leq 2$. In this region, the physics of injection are likely to affect the diffusion behavior. The intermediate zone is defined as the region between $2 \leq (x - X_{\mathrm{inj}})/\delta_{\mathrm{av}} \leq 18$, the transition zone is defined as the region of $18 \leq (x - X_{\mathrm{inj}})/\delta_{\mathrm{av}} \leq 60$ and the final zone where $(x - X_{\mathrm{inj}})/\delta_{\mathrm{av}} > 18$.

Figure 19 shows the behavior of λ/δ_{99} versus $(x - X_{\mathrm{inj}})/\delta_{\mathrm{av}}$ for the Poreh and Cermak [30] results. Also included in this figure are diffusion profiles of temperature by Wieghardt [70], bubbles in a turbulent boundary layer by Sanders et al. [2] and the DNS data of bubble diffusion. The diffusion length scale λ increases as the scalar and bubbles move downstream. The near-wall concentration of passive scalar and bubbles decreases with downstream distance. For a passive scalar in the intermediate zone, λ/δ_{99} follows

a power law as a function of $(x - X_{\text{inj}})/\delta_{\text{av}}$. In the transition zone, λ/δ_{99} approaches 0.64, the value of λ/δ_{99} in the final zone.

In the intermediate zone, Poreh and Cermak [30] found that the wall-normal concentration profiles scaled with λ. Figure 20 plots y/λ versus concentration for the DNS and passive scalar results at different streamwise locations in the intermediate zone. The bubble data that is nearest injection does not collapse onto the same curve, but the results that are further downstream collapse to a curve very similar to that of the passive scalar results. However, very near the wall the bubble concentration approaches zero while the passive scalar concentration reaches a maximum value. In the transition zone, the scaling of wall-normal distance changes from λ, the scaling of the intermediate zone, to δ_{99}, the scaling of the final zone. Figure 21a plots y/λ versus concentration for the DNS and passive scalar results at different streamwise locations in the transition zone. The bubble data collapses on a curve very similar to that of the passive scalar results, except very near the wall where the bubble concentration approaches zero. When scaled with δ_{99} (Figure 21b), the bubble data begins to collapse, with the most downstream results most closely resembling the behavior of a passive scalar in the final zone.

3.4 Discussion

Experiments [2, 56, 59] have shown that in high Reynolds number, spatially-evolving turbulent boundary layers, microbubbles tend to migrate away from the wall as they travel downstream of injection and the skin-friction drag coefficient approaches that of a single-phase turbulent boundary layer. Simulations of bubbles injected into a spatially-evolving turbulent boundary layer were performed using a one-way coupled Euler-Lagrangian approach, with parameters of the simulation chosen to reproduce the low gas-flux, high flow-speed case in the Sanders et al. [2] experiments. Though the Reynolds number of the simulations was lower than the experiment, the bubbles moved away from the wall, which is consistent with the experimental results. In simulations where bubbles were injected into a laminar boundary layer, the bubbles traveled towards the wall, the opposite of what is found in the turbulent simulations and in the Sanders et al. [2] experiments.

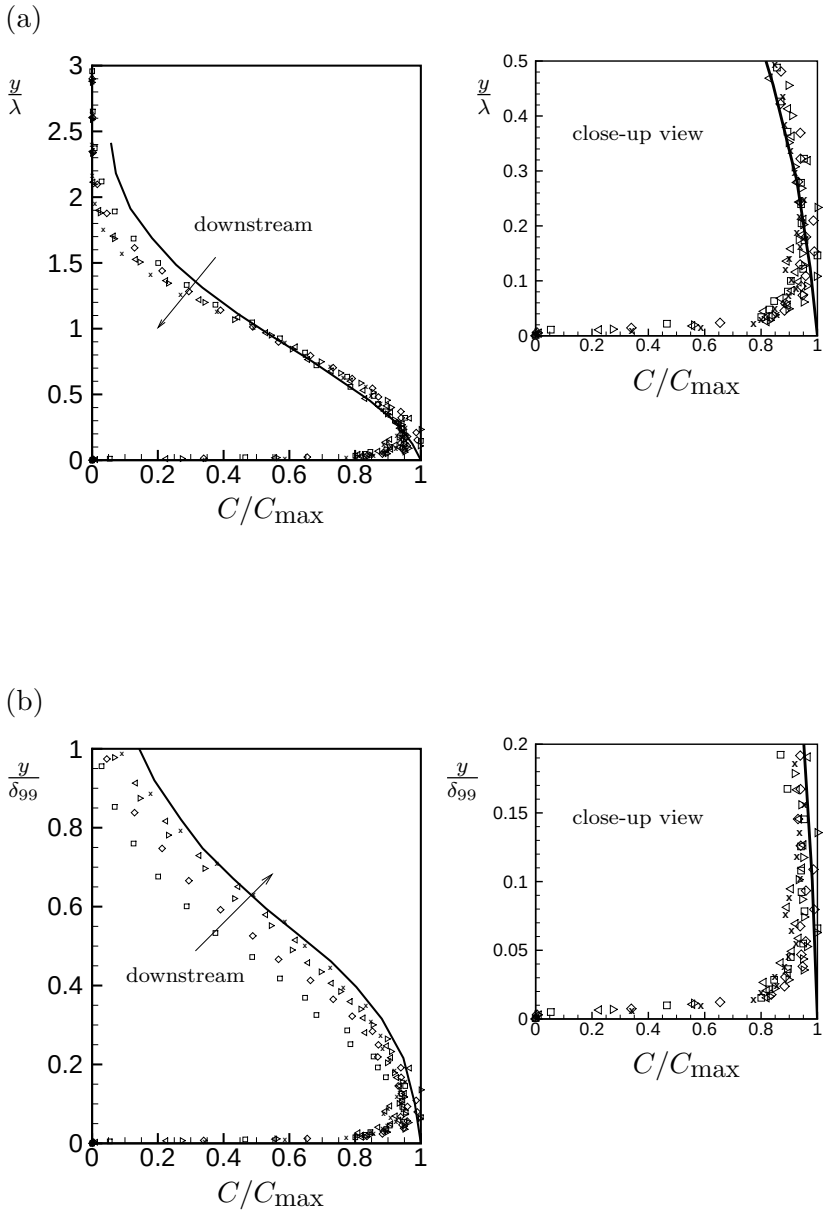

FIGURE 3.19: Concentration profiles for a passive scalar and bubbles in the transition zone of a turbulent boundary layer. Figure (a) shows results for scaling using λ, with the inset figure plotting a near-wall close-up view. $x/\mathrm{L_{ref}}$ = (17.5, 22.5, 27.5, 32.5, 37.5) = (□, ◇, ▷, ◁, x). —, Poreh and Cermak [30] intermediate zone. Figure (b) shows scaling with δ_{99}, with the inset figure plotting a near-wall close-up view. $x/\mathrm{L_{ref}}$ = (17.5, 22.5, 27.5, 32.5, 37.5) = (□, ◇, ▷, ◁, x). —, Poreh and Cermak [30] final zone.

Budgets of the ensemble-averaged bubble acceleration showed that the largest accelerations in the wall-normal direction were due to the drag and fluid acceleration terms. The drag acceleration and buoyancy acted to push the bubbles towards the wall. Downstream of injection, the lift acceleration pushed the bubbles towards the wall. The fluid acceleration was larger than other accelerations and pushed the bubbles away from the wall. The wall-normal bubble acceleration budget shows that the tendency for bubbles to move away from the wall is due to the fluid acceleration pushing the bubbles away from the wall. Investigation into the mean and fluctuating contributions into the bubble accelerations lead to a reduction of the full equations to approximate equations for the movement of bubbles away from the wall.

In this bubbly turbulent boundary layer flow, the behavior between bubbles and passive scalars is qualitatively similar, except very near the wall where the bubble concentration approaches zero. Bubble concentration profiles collapsed when normalizing results with length scales (such as boundary layer thickness δ_{99} and concentration height λ) that also collapsed passive scalar profiles in Poreh and Cermak [30]. For passive scalars in flows with moderate to large Reynolds numbers and large Schmidt numbers, the transport by the local fluid drives the diffusion. For bubble diffusion, the fluid acceleration is the dominant mechanism. The importance of the fluid transport in the diffusion of bubble and passive scalars explains the similar behavior of bubbles and a passive scalar in a turbulent boundary layer.

In the Sanders et al. [2] experiment, the bubble sizes are not monodisperse but have a distribution of sizes. For simplicity, a uniform bubble size equal to the mean was used in the simulation. To account for differences in bubble size, simulations with three different bubble sizes were performed. This range of bubble sizes accounts for 86% of the bubble sizes in the Sanders et al. [2] experiment. This simulation showed that the ensemble-averaged path of all bubble sizes moved away from the wall with increasing downstream distance. The larger bubbles ($R/\delta_{99,\text{inj}} = 0.0092$) have an ensemble-averaged path that is farther away from the wall than smaller bubbles ($R/\delta_{99,\text{inj}} = 0.0037, 0.0064$).

As local void fraction increases, two-way coupling effects are likely to become important. The two-way coupling effect of the bubbles on the turbulent flow has been demonstrated

in Jacob et al. [58]. In this experiment, the shear stress at the wall and Reynolds stress near the wall has been reduced downstream of injection as compared to the single-phase experiment, due to the presence of the bubbles. Though the near-wall turbulence has been modified, the profiles of the turbulent statistics of the fluid flow qualitatively resemble single-phase turbulent profiles near the wall and approach the values of single-phase turbulence away from the wall. Therefore, it is likely that the fluid acceleration will still be the mechanism for bubble dispersion away from the wall.

Chapter 4

Coalescence in a turbulent pipe flow

4.1 Introduction

Bubble coalescence is important for a wide range of practical applications. For example, the buoyancy of bubbles are used to enhance mixing in fluidized-bed reactors. Here, gas is introduced at the bottom of the tank through a porous plate and the rise of the gas through the column creates inhomogeneity in the flow, thus promoting mixing. In addition to gas-flow rate, the flow is affected by the bubble size distribution, which will change due to bubble coalescence. The behavior of these flows depends on the size distribution of the bubbles and void fraction profiles. The challenge is to develop robust, yet efficient and practical, numerical models of the complicated bubble physics to accurately predict these flows in full-scale applications.

A large amount of work has been performed to develop numerical approaches for simulating unsteady bubbly flow while accounting for the effect of bubble coalescence [71–76]. Most work uses either an Euler-Euler (two-fluid approach) or an Euler-Lagrangian approach, where the dispersed phase is modeled by Lagrangian particles. In the Euler-Euler approach, bubbles are not tracked individually but treated as a continuum and various closures for interaction of the bubble phase and the carrier phase along with stochastic

models for bubble-bubble collisions and coalescence must be included. For example, the work of Olmos et al. [71] coupled an Euler-Euler approach along with population balance equations to simulate the evolution of bubble size. A coalescence model by Prince and Blanch [77] was used, with a $k-\epsilon$ turbulence model for the liquid phase. This coalescence model assumes isotropic turbulence in its determination of bubble-bubble collisions. Chen et al. [73] performed Euler-Euler simulations using a bubble population balance equations and compared a variety of bubble breakup and coalescence models. The carrier-phase flow was also simulated with a $k-\epsilon$ turbulence model.

Euler-Lagrangian approaches require at least one less closure model since the locations of each individual bubble is known and bubble-bubble collisions can be computed directly. Darmana et al. [75] developed a coalescence model using the film-drainage timescale by Prince and Blanch [77] and the bubble-bubble interaction timescale by Sommerfeld et al. [72]. Bokkers et al. [76] performed Euler-Lagrangian simulations with a hard-sphere collision model, assuming all collisions lead to coalescence (until a maximum bubble size was reached).

The objective of this approach is to perform high Reynolds number simulations of bubbly flow and account for bubble coalescence without resorting to Reynolds-Averaged Navier-Stokes (RANS) turbulence models or stochastic approximations for bubble-bubble collisions. In flows with complex geometries, models of the collision and coalescence process assuming isotropy of the turbulence (such as Prince and Blanch [77]) will not be accurate in general, due to the influence of geometry on the turbulence. An Euler-Lagrangian methodology is used, and bubble-bubble collisions are computed directly using hard-sphere approach. The bubble coalescence model of Kamp et al. [48] is extended to unsteady flows where bubble-bubble collisions and the relative velocity between colliding bubbles are computed directly.

4.2 Model validation

Colin et al. [1] performed experiments of bubble coalescence in a turbulent pipe flow in both normal and microgravity conditions. The microgravity experiments were performed

on an aircraft that flew a parabolic trajectory to obtain microgravity conditions for $\sim$ 20-30 seconds for each experiment. The experimental setup composed of a long plexiglass tube, with a 4 cm diameter and length of 317 cm, broken into 5 sections. The central part of the pipe was $L_1 = 200$ cm $= 50D$ long, with visualizing test sections on both ends of the central section. The visualizing test sections were each $L_2 = 40.5$ cm $= 10.25D$ long. Void fractions probes were located near the ends of the pipe. Gas was injected and mixed with the fluid phase through a Venturi mixer at the inflow section. For low gas flow-rates and high fluid velocities, dispersed bubbles with a diameter on the order of a few millimeters were observed. As the bubbles traveled downstream, the bubbles grew larger due to coalescence. The void fraction of the microgravity experiment was 4.6% based on the empirical relation determined by Colin et al. [1] of $U_{\mathrm{G}} = 1.2U_{\mathrm{m}}$, where the gas velocity $U_{\mathrm{G}} = U_{\mathrm{GS}}/\epsilon$ and ϵ is the average void fraction and U_{GS} is the superficial gas flow rate. The bulk Reynolds number, based on the mixture velocity, $U_{\mathrm{m}} = U_{\mathrm{GS}} + U_{\mathrm{LS}}$, pipe diameter D and liquid viscosity ν_{L}, was 32,000. The Reynolds number based on the viscous scale velocity ($\mathrm{Re}_\tau \equiv Du_\tau/\nu$) is equal to 1750 in the microgravity experiment. Our simulation was performed at conditions similar to the Colin et al. [1] experiment with a superficial gas flow rate (U_{GS}) of 0.05m/s and a bulk liquid flow speed (U_{LS}) of 0.85 m/s in microgravity.

The simulation parameters were chosen to be similar to experimental conditions by matching the inflow size distribution of bubbles, average void fraction and domain length. The simulation domain consists of a pipe with diameter D and length $L = 81D$, similar in length and Reynolds number as the Colin et al. [1] experiment, whose length from the beginning of the first measurement section to the end of the last measurement section is $2L_2 + L_1 \approx 70D$. The simulation is periodic in the streamwise direction. Bubbles were injected at the inflow plane, traveling downstream with the flow until exiting at the outflow plane. The simulation inflow corresponds with the inflow of the first visualization section in the experiment and the simulation outflow extends $11D$ beyond the outflow of the outflow experimental visualization section.

However, since the Colin et al. [1] experiment did not provide details of the turbulent flow, a simulation of turbulent pipe flow with $Re_\tau = 1920$ was performed to validate mean flow and turbulent statistics with the experiment by Lawn [78]. In the simulation,

$U_{\text{ref}} = 2u_\tau = 1.0$ and a body force was applied to counterbalance the shear stress as the wall of the $\text{Re}_\tau = 1920$ pipe flow. Periodic boundary conditions were applied in the streamwise direction and a dynamic Smagorinsky LES model was used for the carrier phase turbulence.

An unstructured mesh with 12.5×10^6 control volumes was used. The cross-sectional area of the pipe was discretized using an unstructured hexahedral mesh, with the circumference of the pipe discretized into 128 nodes (See Figure 4.1a). In wall units, the azimuthal mesh spacing $D\Delta\theta^+/2 = 47$, where $r = \sqrt{y^2 + z^z}$ is the radial and θ is the azimuthal coordinate. Near the wall, a boundary layer with a minimum wall-normal spacing of $\Delta r/D = 0.002611$ was used and a boundary-layer mesh was grown for 34 rows from the pipe wall with a growth factor of 1.05. The minimum wall-normal spacing in wall units is 2.5. The cross-sectional mesh was extruded downstream with a uniform mesh in the streamwise direction. The grid spacing in the streamwise distance in wall units is $\Delta x^+ \equiv \Delta x \; u_\tau/\nu = 75.0$. The minimum wall-normal spacing Δr^+_{min} is about twice that of the LES simulation with van-Driest wall-damping performed by Rudman and Blackburn [79], though the azimuthal and streamwise mesh spacings are equal. A constant timestep of $\Delta t^+ = \Delta t \; u_\tau/D = 5 \times 10^{-5}$ was used. The timestep is smaller than that used in the DNS of turbulent pipe ($\text{Re}_\tau = 360$) by Eggels et al. [80].

The bubbles were injected in a random position within a circular plane with a diameter of $0.8D$ located at $x/D = 0.01$ and are injected with a constant mass-flux $\dot{m}$. Initially, the bubble velocity is initialized to the local fluid velocity. The mass-flux of bubbles given by $N_{\Delta T}$ bubbles over timescale ΔT is given by

$$\dot{m}_{\Delta T} = \frac{4\rho_{\text{b}}\pi}{3\Delta T} \sum_{i=1}^{N_{\Delta T}} R_i^3, \tag{4.1}$$

where ρ_{b} is the density of the gas inside the bubbles. The timescale ΔT can be broken into n equal parts of the carrier-fluid timestep Δt (i.e. $\Delta T = n\Delta t$). In these simulations, n was chosen to be 240 so that $\dot{m}_{\Delta T} \approx \dot{m}$. The bubble radius R_{mean} is the mean bubble radius of the inflow size distribution. The number of bubbles with size R_{mean} that it

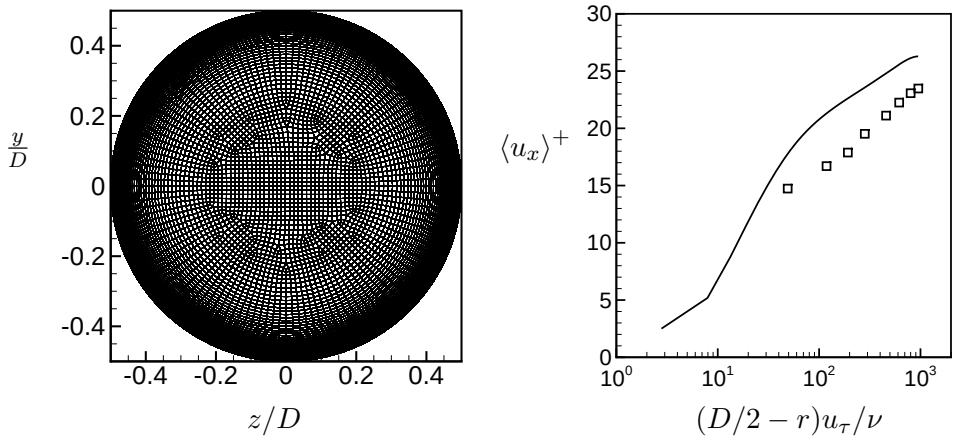

FIGURE 4.1: (a) Cross-sectional mesh of turbulent pipe. (b) Time-averaged streamwise carrier-fluid velocity as a function of distance from the wall, as compared to experiment. —, DNS; □, Lawn [78].

takes to obtain the mass-flow rate is

$$N_{\text{mean}} = \frac{3}{4} \frac{\dot{m} \Delta T}{\rho_{\text{b}} \pi R_{\text{mean}}^3}, \tag{4.2}$$

where ρ_{b} is the density of the gas inside the bubbles, with $\rho_{\text{b}} = \rho_{\text{f}}/1000$. The probability of a bubble being injected into the flow during timestep Δt is given by

$$P_{\text{inj}} = \min\left(1, \frac{N_{\text{mean}}}{n}\right) \cdot \exp\left(-\frac{4\rho_{\text{b}}\pi}{3\Delta t\ \dot{m}} \sum_{i=1}^{N_{\text{inj}}} R_i^3\right), \tag{4.3}$$

where $0 \leq P_{\text{inj}} \leq 1$. Bubbles are injected until the probability P_{inj} is greater than that of a random number x_{ran}, with N_{inj} incremented with every bubble injected during timestep Δt. The random number x_{ran} is generated for each bubble injection and has a uniform distribution between 0 and 1.

The inflow size distribution in the simulation was taken directly from inflow distribution of the Colin et al. [1] experiment and the bubbles are assumed to be massless spheres with a constant size throughout the simulation. Once the bubbles are injected, coalescence is

not allowed to occur until the bubbles reach a downstream distance of $x/D = 10$. This allows the bubbles to equilibrate in the flow after injection.

4.3 Results

4.3.1 Single-Phase Turbulence

Results for the carrier-phase turbulent flow in the bubbly-flow simulation are given in Figures 4.1b and 4.2. Streamwise fluctuations are given by the variable u'_x and the wall-normal fluctuations are given by u'_r. The data was averaged in the streamwise and the azimuthal directions. Single-phase statistics were averaged over 2.8 flow-through timescales (based on a mean velocity of $U_{\text{bulk}}/(2u_\tau) = 11.2$ and a domain length of $81D$).

The simulation over-predicts the streamwise mean velocity, due to a lack of resolution near the wall. In a wall-bounded flow, the shear stress at the wall directly determines the mass flow rate for a given mean pressure gradient. Since the shear is under-resolved, the mass-flux though the pipe is increased to balance the reduced wall shear. This leads to over-predicting the mean streamwise velocity $\langle u_x \rangle$ and $u'_{x,\text{rms}}$. Without near-wall models for LES, the over-prediction of $\langle u_x \rangle$ and $u'_{x,\text{rms}}$ prediction is expected, though good agreement for the turbulence intensities is obtained for $u'_{x,\text{rms}}$ and $u'_{r,\text{rms}}$ away from the wall and $\langle u'_x u'_r \rangle$ in general when compared to results from Lawn [78].

4.3.2 Effect of coalescence

In the simulation, bubble size distributions were obtained as a function of streamwise distance. The size distributions were averaged over 3.9 flow-through timescales (based on a mean velocity of $U_{\text{bulk}}/(2u_\tau) = 11.2$ and a domain length of $81D$). The simulation domain was broken into 15 discrete, equally-sized sections in the streamwise direction, with a $\Delta x_{\text{bin}} = 10D$. The first measurement bin begins from the inflow plane ($x = 0D$) and ends at $x/D = 10$. Corresponding with the experimental location (outflow measurement), the last measurement section samples bubble data from $60 \leq x/D \leq 70$.

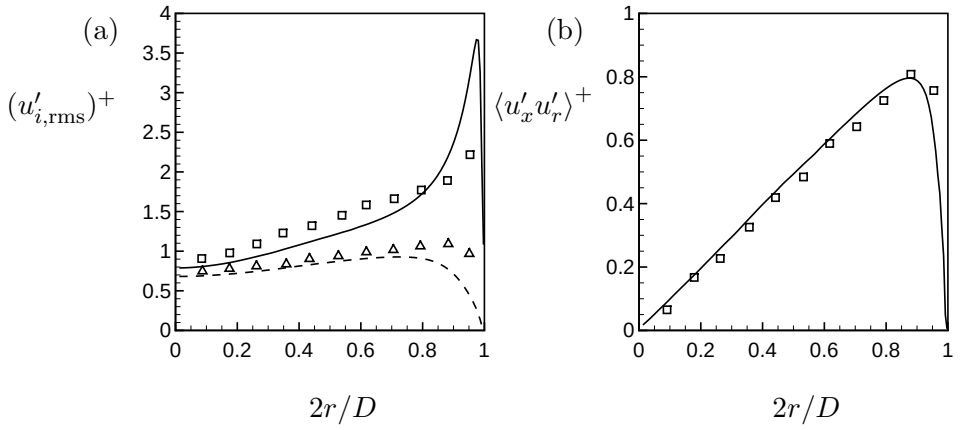

FIGURE 4.2: Time-averaged turbulent fluctuations versus distance from the center of the pipe. (a) RMS fluctuations as compared to experiment. —, $(u'_{x,\mathrm{rms}})^+$ DNS; - -, $(u'_{r,\mathrm{rms}})^+$ DNS; □, $(u'_{x,\mathrm{rms}})^+$ Lawn [78]; △, $(u'_{r,\mathrm{rms}})^+$ Lawn [78]. (b) Reynolds shear stress. —, $\langle u'_x u'_r \rangle^+$ DNS; □, $\langle u'_x u'_r \rangle^+$ Lawn [78].

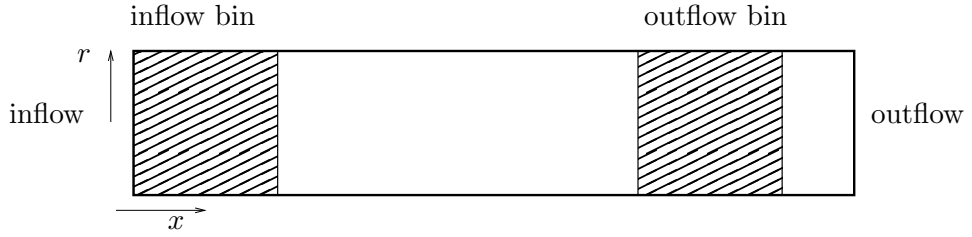

FIGURE 4.3: Inflow and outflow bins for measurement of bubble properties. The length of the inflow/outflow bins is $L_2 = 10D$. The distance between the inflow and outflow bins is L_1. The total distance to the end of the last measurement section is $2L_2 + L_1 = 70D$.

The inflow and outflow measurement sections are visualized in Figure 4.3. Besides the inflow and outflow locations, measurement bins extended from the inflow plane to the outflow plane in the simulation, with a $\Delta x_i = \Delta x_{\mathrm{bin}} = 10D$ (See Figure 4.4).

Figure 4.5 plots the bubble size distribution of the DNS simulation, along with the Colin et al. [1] zero-g experiment at the inflow and outflow. Downstream of injection, the bubbles travel downstream with the flow and collide and coalesce with one another, causing the size distribution to shift towards larger sizes. The size distribution between the experiment and simulation show excellent agreement. Due to coalescence, the number density of the bubbles decreases as the bubble travel downstream. This is observed in Figure 4.6, which plots instantaneous position of bubbles in the pipe flow, both near and

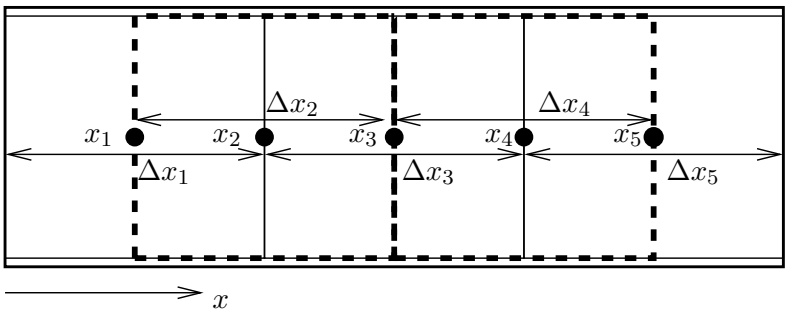

FIGURE 4.4: Streamwise bins for measurement of bubble properties. Each bin ($i = 1, 2, 3, ...$) samples data from bubbles that reside within its streamwise domain ($x_i - \Delta x_i/2 \leq x \leq x_i + \Delta x_i/2$).

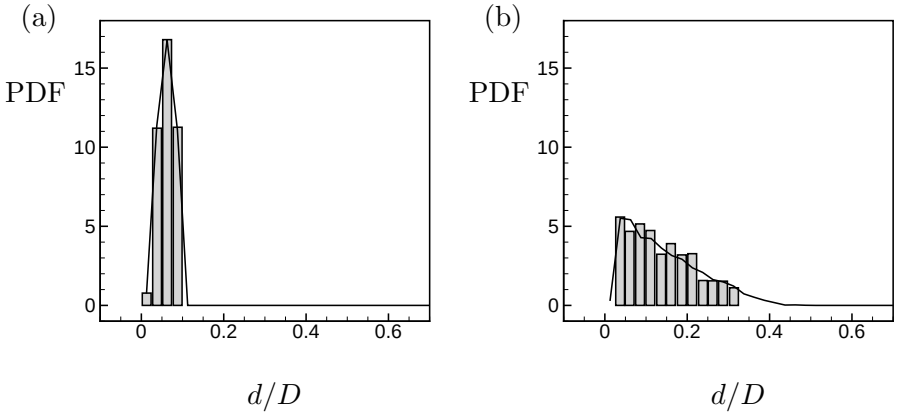

FIGURE 4.5: Comparison of probability distribution function of bubble size from simulation to Colin et al. [1] experiment. Inflow distribution is sampled over $0 \leq x/D \leq 10$ and outflow distribution is sampled over $60 \leq x/D \leq 70$. Solid lines represent simulation results and bars represent results from Colin et al. [1].

far downstream of bubble injection. Far downstream, much larger bubbles are observed than near injection and the overall number of bubbles has decreased.

4.4 Collision details

The evolution of the bubble size distribution depends on the nature of the bubble-bubble collisions. Bubble collision parameters such as relative velocity and bubble size

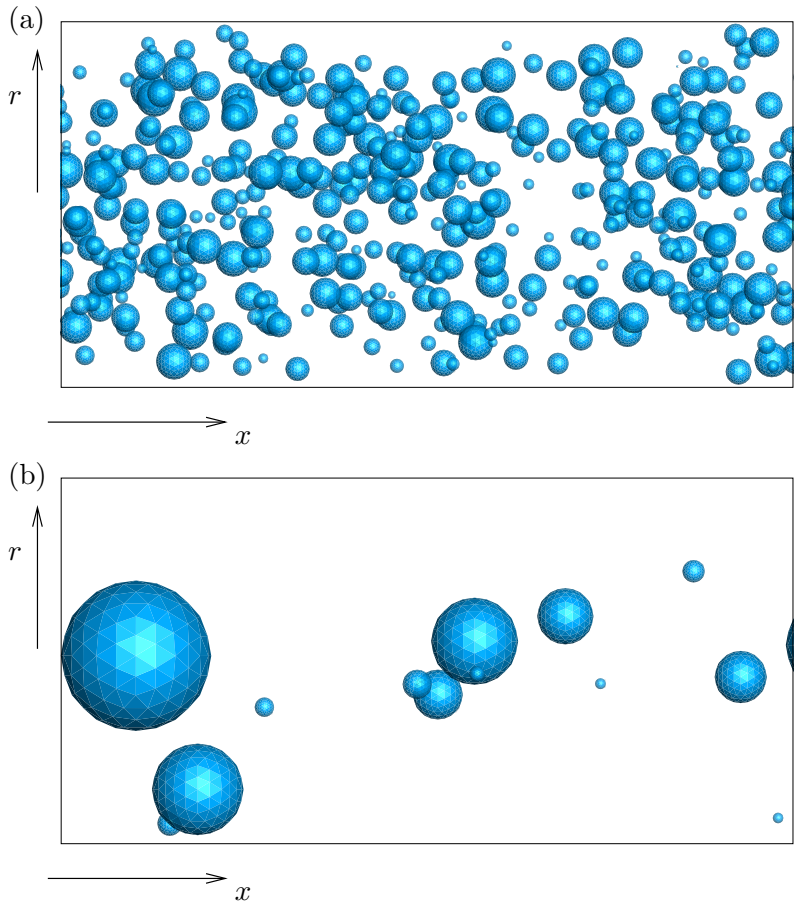

FIGURE 4.6: Instantaneous position of bubbles in turbulent pipe flow, with coalescence. Bubbles are proportional to actual size. Flow is from left to right. View is looking through the pipe, perpendicular to the pipe flow, with the top and bottom boundaries of each figure at $r/D = 0.5$. (a) Near inflow ($4 \leq x/D \leq 6$). (b) Near outflow ($68 \leq x/D \leq 70$).

determine the probability of coalescence. This chapter describes statistics of the bubble-bubble collision process. Mean quantities of collisions ($\overline{f}(x)$) are obtained by integrating over the PDF of f:

$$\overline{f}_j = \int_{-\infty}^{\infty} f \ \mathrm{PDF}(f) \ \mathrm{d}f, \tag{4.4}$$

where the quantities f are sampled for bubbles located within the streamwise bin j between $x_j - \Delta x_{\mathrm{bin}}/2 \leq x \leq x_j + \Delta x_{\mathrm{bin}}/2$.

Instead of averaging over the entire size distribution, mean statistics $\overline{f}(x, d_1, d_2)$ can also be obtained as a function of bubble diameter d_1, d_2 and streamwise distance x by

$$\overline{f}(x, d_1, d_2) = \frac{1}{N_\mathrm{c}(x, d_1, d_2)} \sum_{i=1}^{N_\mathrm{c}(x,d_1,d_2)} f_i(x, d_1, d_2),$$

where $N_\mathrm{c}(x, d_1, d_2)$ is the total number of collisions at x with bubble diameters d_1 and d_2. $\overline{f}(x, d_1, d_2)$ is discretized into streamwise measurement bins and equally-sized bins for d_1 and d_2. The bin-size is determined from the maximum measured bubble diameter d_max in the streamwise bins by $\Delta d_1 = \Delta d_2 = d_\mathrm{max}/10$ for a total of 10×10 bins for each streamwise bin for $\overline{f}(x, d_1, d_2)$. Since there is no statistical difference between d_1 and d_2, $\overline{f}(x, d_1, d_2)$ is enforced to be symmetric about $d_1 = d_2$. Statistics are obtained from four streamwise locations. For smoothness of mean quantities, samples that are larger than $\mathrm{Re_{eq}} = 8000$, $t_d/t_i = 10$ and $V_o = 15$ are discarded from calculations of $\overline{f}(x, d_1, d_2)$ as outliers from visual inspection of their respective PDFs. Also, mean values of $\overline{f}(x, d_1, d_2)$ are blanked if obtained from less than 125 collisions from from bins over streamwise distances$0 \leq x/D \leq 10$, $10 \leq x/D \leq 20$ and $20 \leq x/D \leq 30$, while mean values are blanked if less than 25 collisions are used to obtain statistics from $45 \leq x/D \leq 55$.

Due to coalescence, the number of collisions $N_\mathrm{c}(x)$ decreases rapidly with increasing distance as the number density of bubbles decreases (Figure 4.7a). In Figure 4.8, the total number of collisions decreases with downstream distance for each bin. This makes obtaining converged statistics difficult far downstream ($x/D > 45$). As the size distribution increases due to coalescence, the location for maximum $N_\mathrm{c}(x, d_1, d_2)$ moves to higher values of (d_1, d_2). The movement of the peak of $N_\mathrm{c}(x, d_1, d_2)$ is consistent with the evolution of the size distribution, where larger bubbles are becoming more likely downstream due to coalescence and are also therefore more likely to collide with another bubble.

The mean probability of coalescence $\overline{P_c}(x)$ is plotted in Figure 4.7b as a function of streamwise distance. The mean probability increases slightly near the inflow, then decreases with downstream distance. The value of $\overline{P_c} = 0$ from $0 \leq x/D \leq 10$ since coalescence is turned off in this region. The overall probability decreases from $\sim 30\%$

near the inflow to $\sim 25\%$ near the outflow. The bubbles that collide far downstream are less likely to coalesce than bubbles that collide near the inflow. Figure 4.9 plots the mean probability of coalescence $\overline{P_c}(x, d_1, d_2)$ as a function of x, d_1 and d_2. A value of zero for Figure 4.9a is due to coalesce not turned on in from $0 \leq x/D \leq 10$. Large bubbles are less likely to coalesce than small bubbles. The mean probability of coalescence is ~ 0.5 for small bubbles, and approaches 0.2 for large bubbles. With increasing downstream distance, P_c increases for constant bubble diameters (d_1, d_2).

The mean ratio of fluid drainage timescale to interaction timescale ($\overline{t_d/t_i}(x)$) slightly decreases then increases with downstream distance (See Figure 4.10a), which correllates with the decrease of probability of coalescence $\overline{P_c}(x)$ with increasing downstream distance. Figure 4.10b plots the PDF of t_d/t_i, and the PDFs of t_d/t_i are similar for the four streamwise locations shown. Small bubbles have smallest $\overline{t_d/t_i}(x, d_1, d_2)$, increasing with bubble size (at constant x) (see Figure 4.11). With increasing downstream distance, $\overline{t_d/t_i}(x, d_1, d_2)$ decreases (for (d_1, d_2) held constant).

The mean relative velocity $\overline{V_o}(x)$ decreases with increasing downstream distance (Figure 4.12a). Figure 4.12b plots the evolution of the relative velocity PDF as a function of streamwise distance, with the distribution becoming more concentrated about the mode with increasing downstream distance. The mean relative velocity at collision $\overline{V_o}(x, d_1, d_2)$ is less for small bubbles as compared to large bubbles (Figure 4.13). For a constant (d_1, d_2), $\overline{V_o}(x, d_1, d_2)$ decreases with downstream distance. For constant x, $\overline{V_o}(x, d_1, d_2)$ increases with increasing (d_1, d_2).

The average collision Reynolds number $\overline{\mathrm{Re}_{\mathrm{eq}}}(x)$ is plotted in Figure 4.14a as a function of streamwise distance. $\overline{\mathrm{Re}_{\mathrm{eq}}}(x)$ is ~ 1000 near the inflow, and increases with downstream distance. The PDF of $\mathrm{Re}_{\mathrm{eq}}$ as a function of streamwise distance is given in Figure 4.14b, with $\mathrm{Re}_{\mathrm{eq}} \sim 750$ the most probable value, though the PDF shifts towards larger values of collision Reynolds number with increasing streamwise distance. Mean collision Reynolds number $\overline{\mathrm{Re}_{\mathrm{eq}}}(x, d_1, d_2)$ increases with increasing bubble size (d_1, d_2) (Figure 4.15). Small bubbles have the smallest $\overline{\mathrm{Re}_{\mathrm{eq}}}(x, d_1, d_2)$ for a given x. As downstream distance increases, the collision Reynolds number increases for constant bubble diameter.

The average bubble size increases with downstream distance, as shown in Figure 4.16a. Recall that $d_{\mathrm{eq}} = (2d_1d_2)/(d_1+d_2)$. As the overall bubble size increase, so does d_{eq}. Also, the PDF of d_{eq} (Figure 4.16b) becomes more weighted to larger bubbles as downstream distance increases due to coalescence.

The mean collision Weber number $\overline{\mathrm{We}_{\mathrm{eq}}}(x)$ is ~ 3 (Figure 4.17a). In Figure 4.17b, the PDFs of $\mathrm{We}_{\mathrm{eq}}(x)$ at four different streamwise locations are similar, with low Weber numbers being the most probable.

The mean collision angle $\theta_{\mathrm{c}}(x)$ remains constant throughout the domain, with $\overline{\theta_{\mathrm{c}}} = 2.33$ (Figure 4.18a), which is 135° from the line-of-centers of the colliding bubbles. Figure 4.18b plots the PDF of θ_{c}, and the PDFs are similar for the four streamwise locations shown. The mode of the collision angle θ_{c} is equal to the mean collision angle $\overline{\theta_{\mathrm{c}}}$.

The mean radial location of collision, $\overline{R_{\mathrm{c}}}(x)$, is obtained from the radial component of the point where the colliding bubbles 1 and 2 are touching. In Figure 4.19a, $\overline{R_{\mathrm{c}}}(x)$ decreases with increasing downstream distance, with collisions far downstream occuring more towards the center of the pipe. The PDF of R_{c} for four streamwise locations is shown in Figure 4.19b. Since the collisions are turbulence driven, the most likely location for collision is near the wall, where turbulent fluctuations are largest. Turbulence flutuations are lowest in the center of the pipe, hence collisions near the center are not as likely to occur. With increasing downstream distance, the PDFs of R_{c} become more weighted to the center of the pipe.

4.5 Discussion

A one-way coupled Euler-Lagrangian methodology is used to simulate bubbly flow including the effect of coalescence, and bubble-bubble collisions are computed directly using a hard-sphere approach. A stochastic bubble coalescence model is developed, with the probability of coalescence determined from an expression of coalescence timescales derived by Kamp et al. [48], for the Euler-Lagrangian approach in which collisions and the relative velocity between colliding bubbles are computed directly.

Excellent agreement was obtained for the bubble size distribution between the Colin et al. [1] experiment and numerical simulations including coalescence. Coalescence increases the mean size of the bubbles and also increases the prevalence of large bubbles in the flow. Bubble size increases through the merging of smaller bubbles, decreasing the number density of bubbles. Far downstream from injection, the total number of bubbles is greatly decreased which also decreases the overall number of collisions. The mean probability of coalescence $\overline{P_c}(x)$ was found to decrease slightly with increasing downstream distance which can be attributed to an increase in bubble size due to coalescence.

The probability of coalescence is determined by an expression that is evaluated at the moment of collision and based on the ratio of fluid drainage and bubble-interaction timescales, where $P_\mathrm{c} = \exp(-t_d/t_i)$. With an increase in the ratio of these timescales, the probability of coalescence decreases. There are a number of factors that influence the ratio of the coalescence timescales. Recall the expression (Eqn. 2.124)

$$\frac{t_d}{t_i} \propto \sqrt{\frac{3\rho_\mathrm{f} V_o^2 d_\mathrm{eq}}{C_\mathrm{vm}\sigma}}.$$

The only parameters that vary from collision-to-collision are V_o, d_eq and C_vm. From inspection of the equation for P_c it is evident that P_c decreases with downstream distance due to an increase in the ratio of coalescence timescales. Due to coalescence, d_eq increases as a function of $d_\mathrm{eq} = (2d_1d_2)/(d_1 + d_2)$. The coalescence timescale $t_d/t_i \propto \sqrt{d_\mathrm{eq}}$, thus an increase in bubble diameter will also increase t_d/t_i, reducing the probability of coalescence at the moment of collision. Physically, this can be understood since it will take longer for surface tension to drain the fluid from between small bubbles than large bubbles. The coalescence timescale $t_d/t_i \propto \sqrt{1/C_\mathrm{vm}}$, thus as the ratio of bubble diameters d_1/d_2 departs from 1, the value of C_vm decreases. This increases the timescale t_d/t_i, reducing the probability of coalescence at the moment of collision. The effect can be seen in Figure 4.9, where the probability of coalescence $\overline{P_c}(x, d_1, d_2)$ increases for bubbles with large ratios of relative bubble sizes. The relative velocity $V_o \propto t_d/d_i$, therefore as $\overline{V_o}(x)$ decreases with downstream distance, the effect is to reduce the probability of coalescence.

With increasing downstream distance, the radial location of bubble-bubble collision

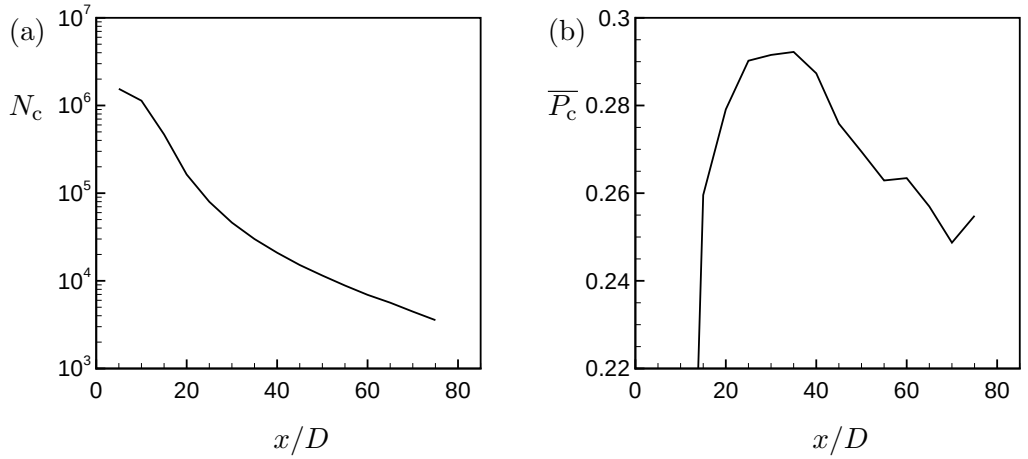

FIGURE 4.7: (a) Streamwise evolution of total number of collisions N_c. (b) Streamwise evolution of mean probability of coalescence $\overline{P_c}$.

$\overline{R_c}(x)$ increases. This is due to the finite size of the large bubbles, who are not able be as near the wall as small bubbles. The velocity scales near the center of the pipe are much larger than that near the wall. Thus, bubbles colliding near the center of the pipe will also have a smaller relative velocity V_o since their velocities are more correlated. However, for a given streamwise location, the relative velocity is shown to increase with increasing bubble size (Figure 4.13). Also, the drag coefficient of the large bubble will decrease (since Re_b increases) and the large bubble is less likely to follow the local flow than smaller bubbles. Other small bubbles in the nearby vicinity are likely to be more correlated to the flow (through a larger drag coefficient), thus small bubbles colliding will have a smaller relative velocity and are more likely to coalesce.

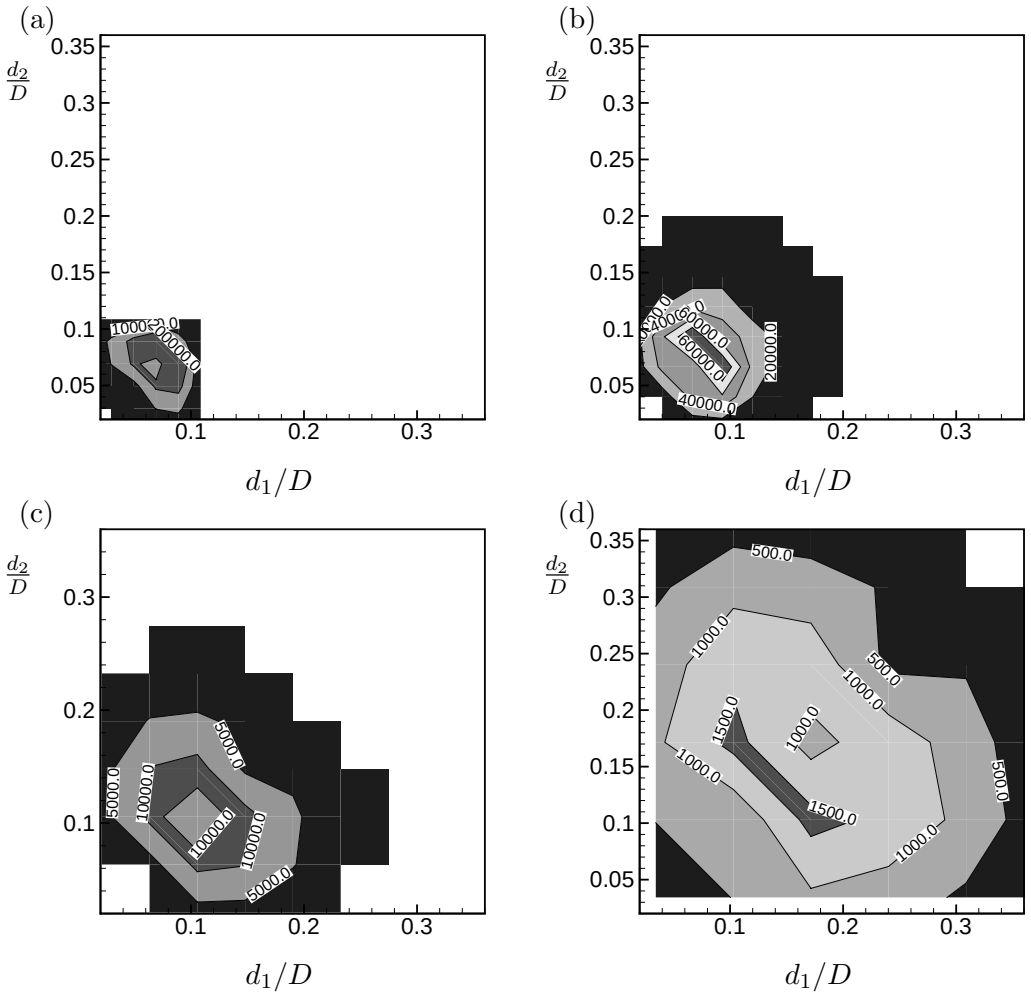

FIGURE 4.8: Number of collisions $N_c(x, d_1, d_2)$ vs. d_1, d_2 for (a) $0 \leq x/D \leq 10$, (b) $10 \leq x/D \leq 20$, (c) $20 \leq x/D \leq 30$, (d) $45 \leq x/D \leq 55$, including coalescence.

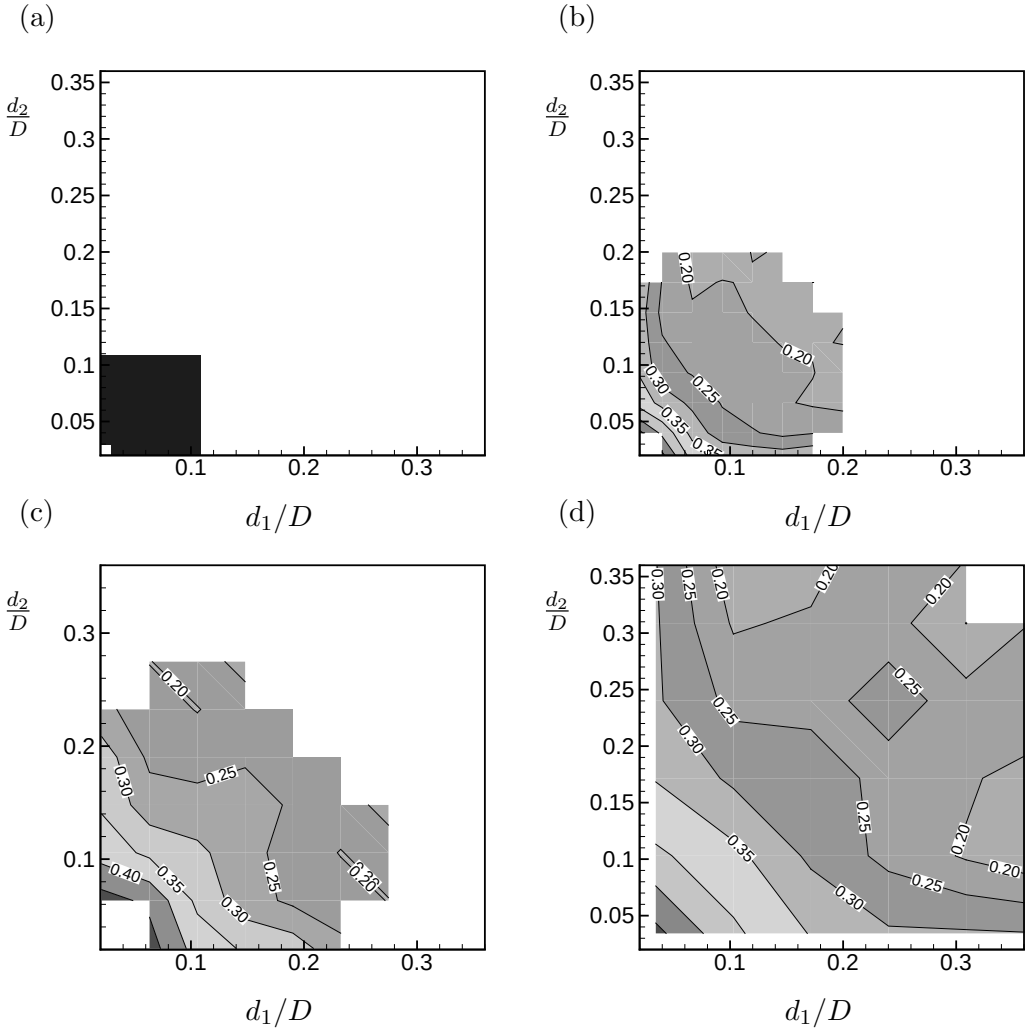

FIGURE 4.9: Probability of coalescence $\overline{P_c}(x, d_1, d_2)$ vs. d_1, d_2 for (a) $0 \leq x/D \leq 10$, (b) $10 \leq x/D \leq 20$, (c) $20 \leq x/D \leq 30$, (d) $45 \leq x/D \leq 55$, including coalescence.

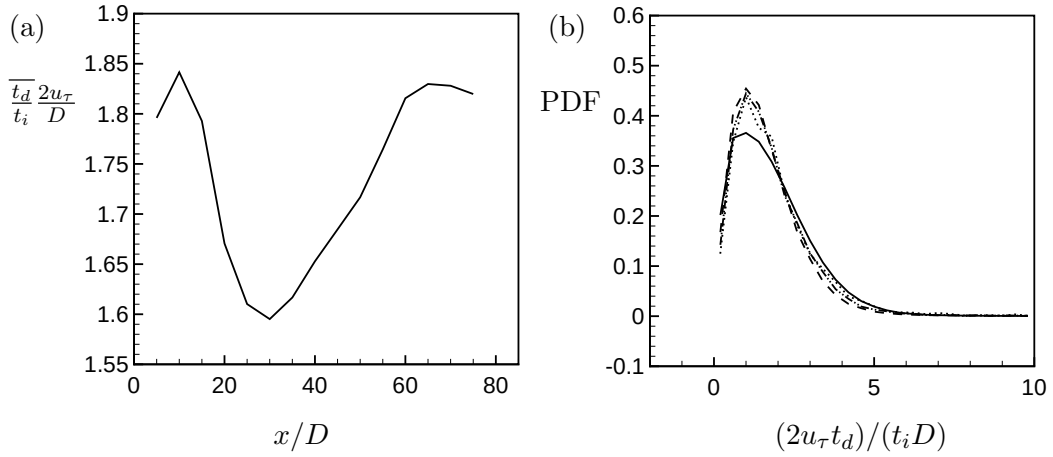

FIGURE 4.10: (a) Streamwise evolution of t_d/t_i. (b) PDF of t_d/t_i for four streamwise locations: —, $0 \leq x/D \leq 10$; - -, $20 \leq x/D \leq 30$; -···-, $45 \leq x/D \leq 55$; · · ·, $70 \leq x/D \leq 80$

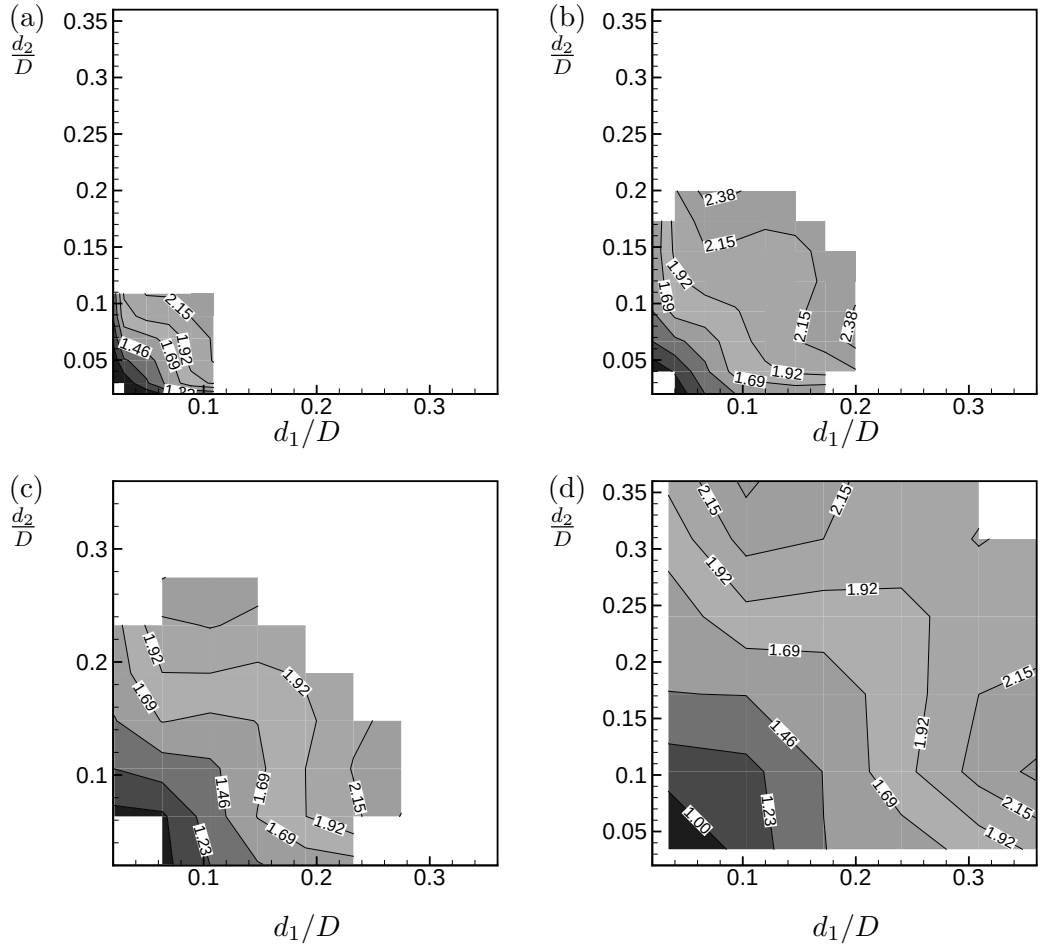

FIGURE 4.11: Ratio of coalescence timescales $\overline{t_d/t_i}(x, d_1, d_2)$ vs. d_1, d_2 for (a) $0 \leq x/D \leq 10$, (b) $10 \leq x/D \leq 20$, (c) $20 \leq x/D \leq 30$, (d) $45 \leq x/D \leq 55$, including coalescence.

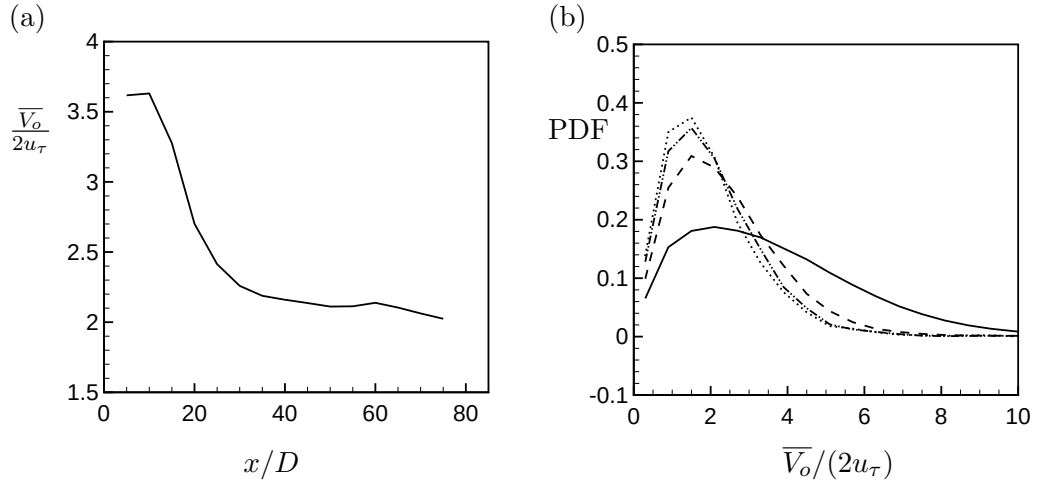

FIGURE 4.12: (a) Streamwise evolution of the magnitude of the relative velocity V_o between colliding bubbles. (b) PDF of R_c for four streamwise locations: —, $0 \leq x/D \leq 10$; - -, $20 \leq x/D \leq 30$; -···-, $45 \leq x/D \leq 55$; · · ·, $70 \leq x/D \leq 80$

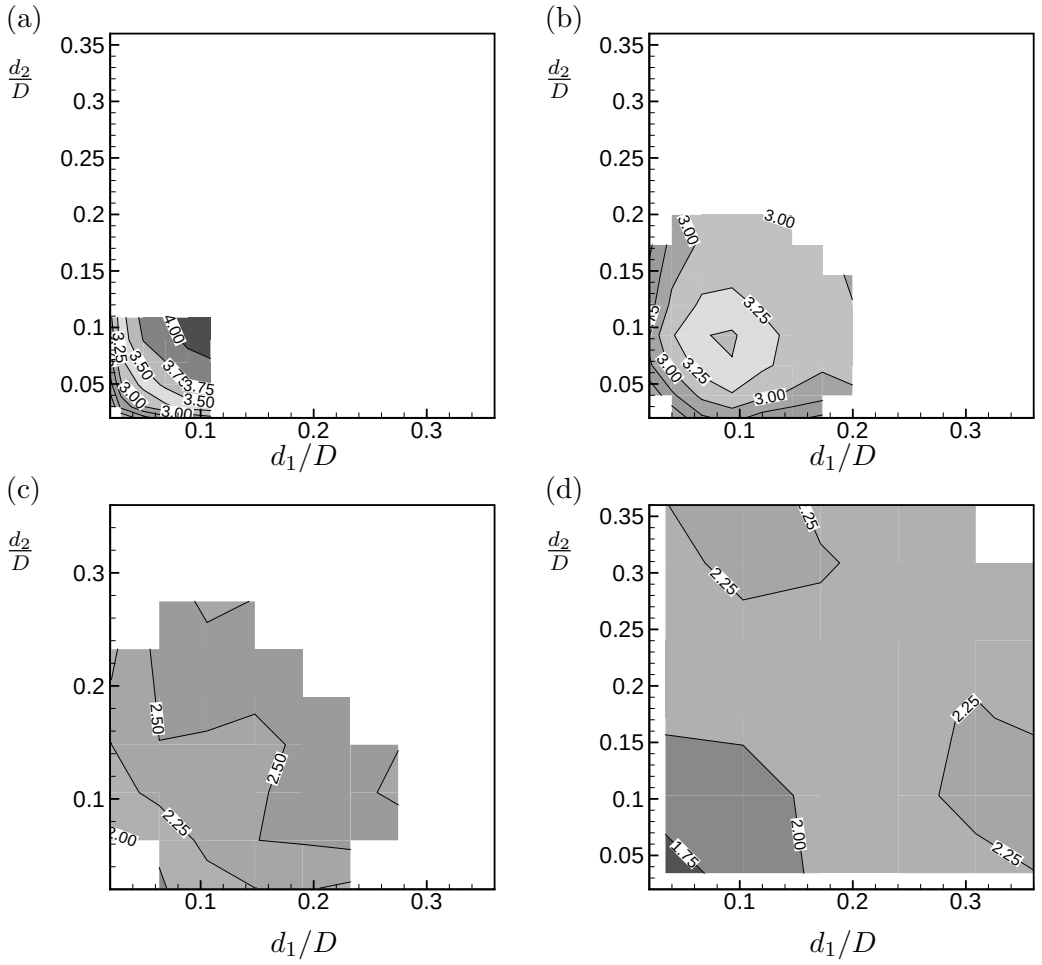

FIGURE 4.13: Relative velocity of collision $\overline{V_o}(x, d_1, d_2)$ vs d_1, d_2 for (a) $0 \leq x/D \leq 10$, (b) $10 \leq x/D \leq 20$, (c) $20 \leq x/D \leq 30$, (d) $45 \leq x/D \leq 55$, including coalescence.

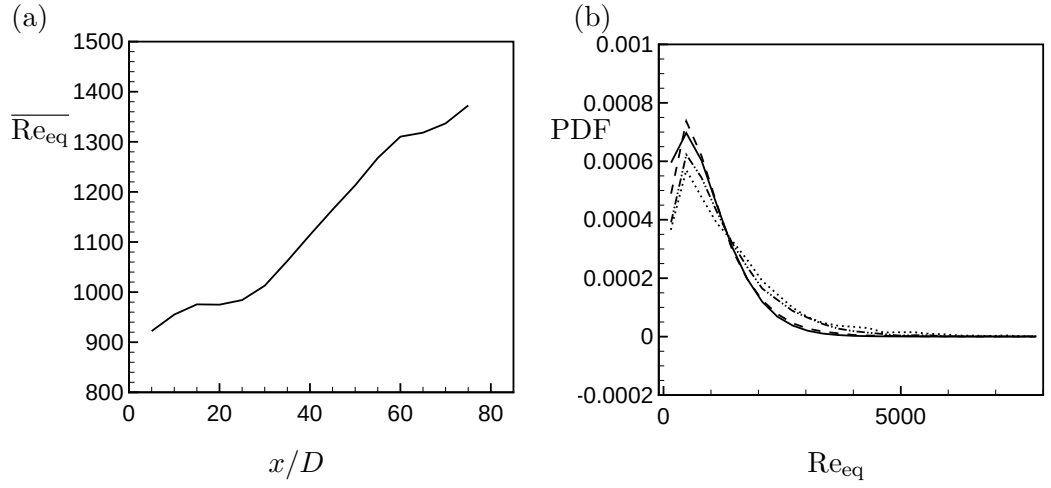

FIGURE 4.14: (a) Streamwise evolution of $\overline{\mathrm{Re}_{\mathrm{eq}}}$. (b) PDF of $\mathrm{Re}_{\mathrm{eq}}$ for four streamwise locations: —, $0 \leq x/D \leq 10$; - -, $20 \leq x/D \leq 30$; -···-, $45 \leq x/D \leq 55$; · · ·, $70 \leq x/D \leq 80$

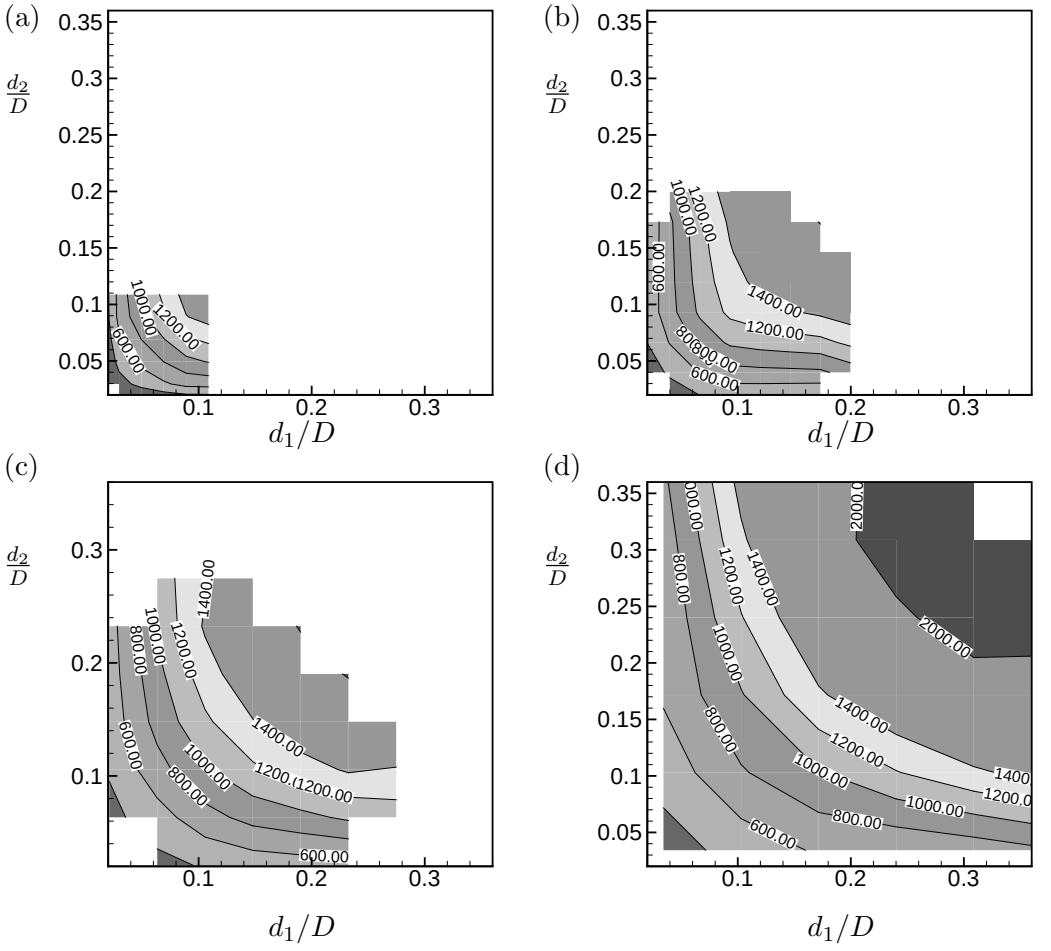

FIGURE 4.15: Collision Reynolds number $\overline{\mathrm{Re}_{\mathrm{eq}}}(x, d_1, d_2)$ vs. d_1, d_2 for (a) $0 \leq x/D \leq 10$, (b) $10 \leq x/D \leq 20$, (c) $20 \leq x/D \leq 30$, (d) $45 \leq x/D \leq 55$, including coalescence.

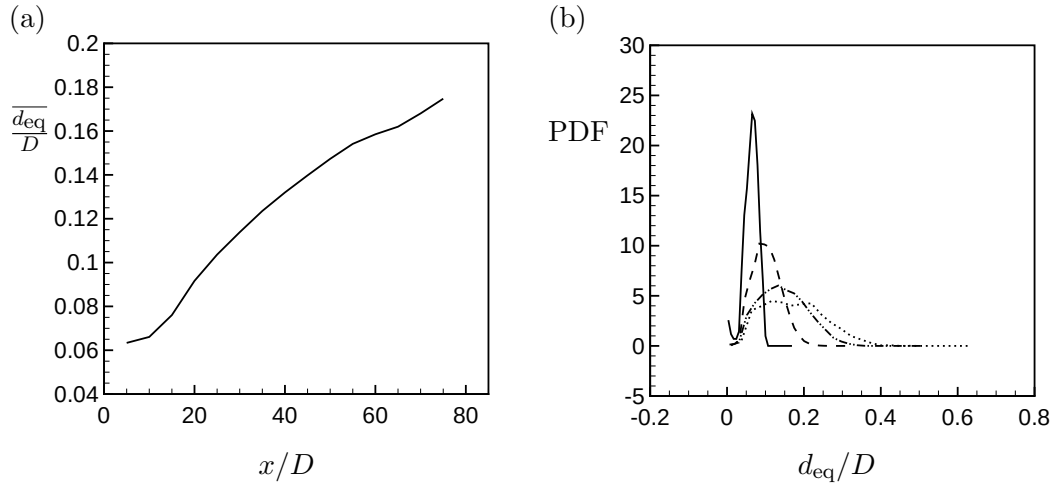

FIGURE 4.16: (a) Streamwise evolution of $\overline{d_{eq}}$. (b) PDF of d_{eq} for four streamwise locations: —, $0 \leq x/D \leq 10$; - -, $20 \leq x/D \leq 30$; ·---·, $45 \leq x/D \leq 55$; · · ·, $70 \leq x/D \leq 80$

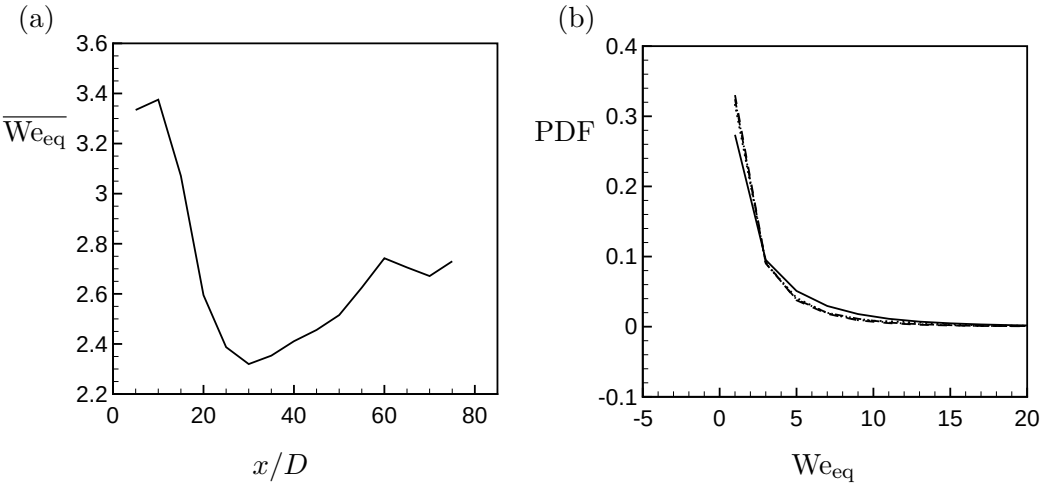

FIGURE 4.17: (a) Streamwise evolution of $\overline{We_{eq}}$. (b) PDF of We_{eq} for four streamwise locations: —, $0 \leq x/D \leq 10$; - -, $20 \leq x/D \leq 30$; ·---·, $45 \leq x/D \leq 55$; · · ·, $70 \leq x/D \leq 80$

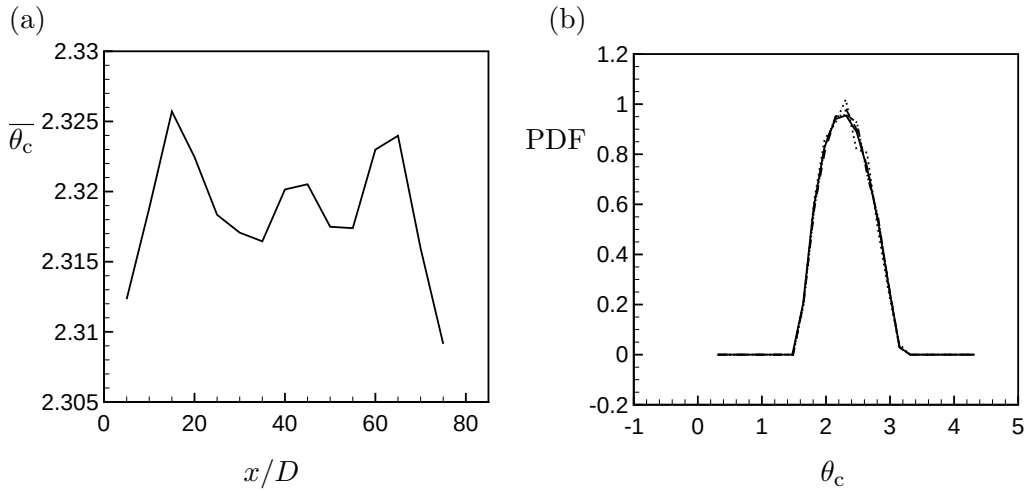

FIGURE 4.18: (a) Streamwise evolution of θ_c. (b) PDF of θ_c for four streamwise locations: —, $0 \leq x/D \leq 10$; - -, $20 \leq x/D \leq 30$; ·-·-, $45 \leq x/D \leq 55$; · · ·, $70 \leq x/D \leq 80$

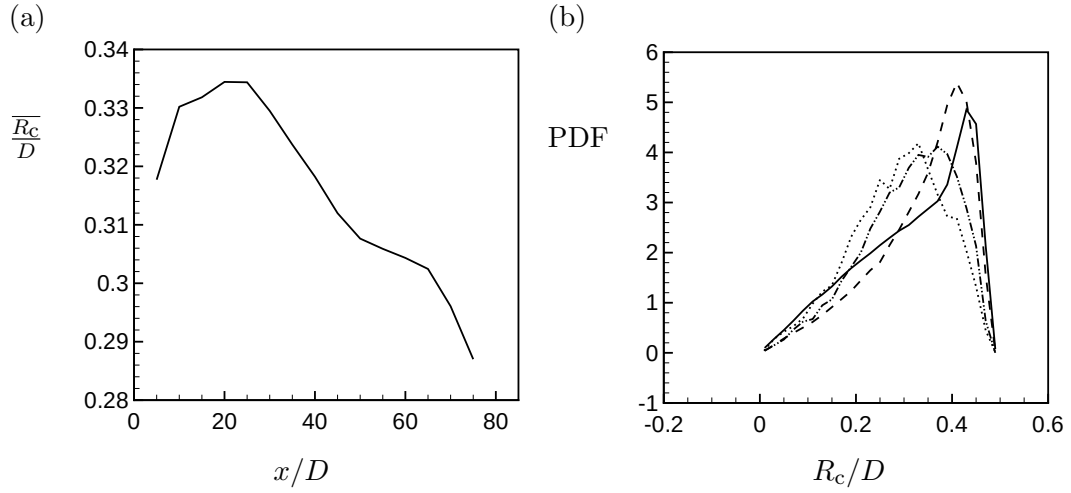

FIGURE 4.19: (a) Streamwise evolution of R_c. (b) PDF of R_c for four streamwise locations: —, $0 \leq x/D \leq 10$; - -, $20 \leq x/D \leq 30$; ·-·-, $45 \leq x/D \leq 55$; · · ·, $70 \leq x/D \leq 80$

Chapter 5

Cavitation in a turbulent flow over a cavity

Turbulent flow over a cavity is a classic canonical problem. Incoming turbulent flow separates at the leading edge of the cavity and a shear layer is formed. Vortices are shed from the leading edge, travel downstream with the flow and impinge on the trailing edge of the cavity. A low-frequency pressure oscillation is observed at the trailing edge due to the impingement of the shear-layer vortices [3]. When the cavitation index σ_v is reduced, cavitation is observed in the flow, first at the expansion corner at the trailing edge, then in the vortices shed from the leading edge when σ_v is further decreased. The cavitation bubbles respond to the pressure fluctuations by rapidly changing their volume. When a shear-layer vortex nears the trailing-edge, the downwash creates a high-pressure region and the cavitating bubbles located near the trailing edge collapse [3].

The one-way coupled Euler-Lagrangian approach was applied to simulate the cavitation experiment by Liu and Katz [3]. Simulating this flow is difficult due to the large numbers of bubbles involved and the complexity of bubble-bubble and bubble-fluid interactions. This chapter shows results for one-way coupled simulations in which the behavior of the bubble radius is determined from the Rayleigh-Plesset equation (Eqn. 2.40), though bubble-bubble collisions, coalescence and breakup were not modeled (though hard-sphere bubble-wall collisions were included). These simulations provide the groundwork for

evaluating the Euler-Lagrangian model in complex, cavitating flows and insight into further improvement. The one-way coupled Euler-Lagrangian model predicted cavitation inception at the trailing edge of the cavity and also in the vortices shed from the leading edge.

5.1 Computational and Physical Parameters

The Liu and Katz [3] experiment was performed in a small water tunnel, with a test section that consisted of a contraction ramp leading to the cavity, followed by a diffusing ramp. The leading edge is the edge of the cavity nearest to the inflow and the trailing edge is the cavity edge nearest the outflow. In the experiment, the cavity height H was 30 mm, L_c was 38.1 mm and the width of the cavity, L_z, was 50.8 mm wide. The free-stream velocity U_∞ was 5 m/s, with a Reynolds number based on the cavity length L_c and free-stream velocity U_∞ of $\mathrm{Re}_L = 1.7 \times 10^5$. The Reynolds number based on the momentum thickness θ near the leading edge of the cavity was $\mathrm{Re}_\theta = 1096$.

Simulations were performed in a domain with a channel inflow leading to a cavity, followed by a channel leading to an outflow plane. The simulation schematic is shown in Figure 5.1. For the simulations, the reference length L_{ref} was set to 1 mm and the reference velocity U_{ref} was set to 1 mm/s. The inflow length L_{in} is 70 L_{ref} and the outflow length is L_{out} is 91.9 L_{ref}. The height from the inflow / outflow section bottom wall to the top wall (L_y) is 33.5 L_{ref}, the length of the cavity is $L_c = 38.1 L_{\mathrm{ref}}$ and the width of the computational domain (L_z) is 50.8 L_{ref}. The coordinate system origin is located at the leading edge of the cavity, mid-way between the periodic boundaries in the spanwise direction. At the outflow a zero-gradient boundary condition is applied in the streamwise direction. At the inflow plane, a separate simulation is performed to generate the appropriate turbulence, and the instantaneous velocity field from the inflow simulation is then interpolated to the inflow plane of the cavity simulation. In this manner, the turbulence at the inflow can be validated to ensure that the correct boundary conditions are being applied. A. Verma performed the single-phase simulations and obtained converged statistics for the flow.

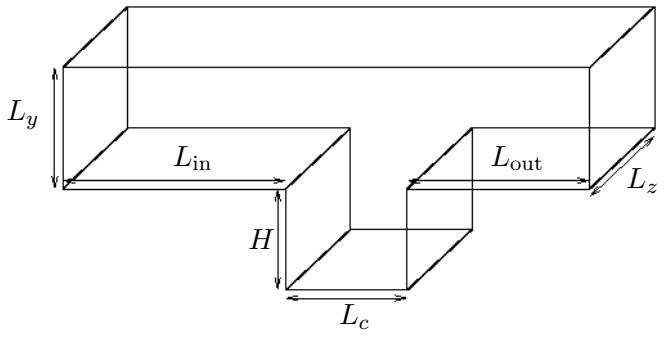

FIGURE 5.1: Domain of the cavity simulation.

The bubble dynamics are solved using the Rayleigh-Plesset equation coupled with the carrier phase solver. In the one-way coupled formulation, physics such as two-way coupling and bubble-breakup are not accounted for, so gas nuclei that incept in the flow would expand indefinitely if unchecked. As a remedy, the bubble radius is limited to a size of $R = 1$ mm $= L_{\text{ref}}$.

Two simulations were performed: 1) a low Reynolds-number simulation performed using DNS and 2) a high Reynolds-number simulation performed using Large-Eddy Simulation (LES). A dynamic Smagorinsky model was used for the LES. Performing a DNS simulation at the experimental Reynolds number of the experiment would be prohibitively expensive and LES reduces the cost of high Reynolds number simulations by modeling the scales at the sub-grid level while resolving the large, unsteady flow-scales discretized by the computational mesh. This method is superior in accuracy in unsteady flow to a RANS approach since the unsteadiness of the flow is retained [18].

To model cavitation inception, micro-bubbles with initial radii ($R_o \sim 10 - 25$mm) are injected in the near-wall region by the cavity leading edge. These bubbles are the gas nuclei that reside in most fluids and are believed to be a mechanism for cavitation inception [9]. When these small nuclei reach a region of very low pressure, their volume grows rapidly and macroscopic pockets of water vapor are formed in the flow. This formation of macroscopic vapor pockets from the unstable rapid growth of the gas nuclei is the definition of cavitation inception. Predicting when and where cavitation inception occurs is very difficult and depends on many factors such as cavitation number σ_v and density of gas nuclei in the flow, among other factors [9].

The cavitation number σ_v is defined as

$$\sigma_v = \frac{P_\infty - P_\mathrm{v}(T_\infty)}{\frac{1}{2}\rho_\infty U_\infty^2}, \tag{5.1}$$

where P_∞ is the far-field (ambient) fluid pressure, $P_\mathrm{v}(T_\infty)$ is the far-field vapor pressure of the carrier fluid at temperature T_∞, ρ_∞ is the fluid density at far-field and U_∞ is usually taken as the free-stream velocity. In general, the lower the cavitation number the more likely cavitation is to occur, and once it occurs lowering the cavitation number increases the occurrence and persistence of vapor pockets.

The local pressure coefficient C_p is defined as the difference from the local pressure to the pressure at free-stream

$$C_p(\vec{x}, t) = \frac{P(\vec{x}, t) - P_\infty}{\frac{1}{2}\rho_\infty U_\infty^2}. \tag{5.2}$$

C_p is dependent on the local flow characteristics and also global quantities such as Reynolds number. In regions of large fluid acceleration or in the centers of vortices, C_p values are low. The cavitation inception index σ_i is defined as the cavitation index where cavitation inception is first observed when the tunnel pressure is slowly lowered.

5.2 Low Reynolds-number simulation

To simulate this flow, the one-way coupled Euler-Lagrangian method was used. A single-phase simulation of the turbulent cavity flow was run to statistical steady state, and then bubbles were injected inside the boundary layer near the leading edge. The Reynolds number based on the free-stream velocity and the cavity wall length was $\mathrm{Re}_L = 17,000$ and the Reynolds number based on the free-stream velocity and boundary layer momentum thickness θ (obtained just before the leading edge) $Re_\theta = U_\infty \theta / \nu_\mathrm{f} = 87.6$. A single bubble was injected every timestep. The cavitation number (taken near the leading edge) was -0.4 and the equilibrium Weber number ($\mathrm{We} = \rho_\mathrm{f} U_\infty^2 R_o / \sigma$) is 3.406 to match conditions for bubbles in water.

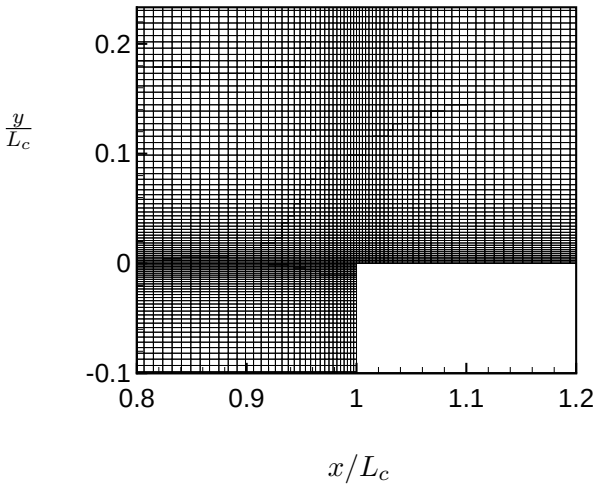

FIGURE 5.2: Computational mesh near the trailing edge for the low Reynolds-number simulation.

A mesh with ~ 7 million grid points was used, with refinement at the leading and trailing edges and the walls of the simulation. Figure 5.2 shows the grid in the trailing edge region. The minimum y spacing is $\Delta y_{\min}/L_{\text{ref}} = 0.05$. A boundary layer is grown from both the top and the bottom walls of the inflow and outflow channels with a growth ratio of 1.05 until a maximum wall-normal spacing of $\Delta y_{\max}/L_{\text{ref}} = 0.33$ is reached. From both the leading and trailing edge a boundary layer mesh is grown from the corner in the x-direction, with a minimum spacing of $\Delta x_{\min}/L_{\text{ref}} = 0.1$. The boundary layer was grown with a ratio of 1.05, with a maximum spacing of $\Delta x_{\max}/L_{\text{ref}} = 0.33$. A uniform grid is used in the spanwise direction, with a grid spacing of $\Delta z/L_{\text{ref}} = 0.996$. The velocity inflow plane is obtained from a laminar Blasius profiles growing from the top and bottom walls, each with a boundary layer thickness $\delta_{99}/L_{\text{ref}} = 1.74$. The simulation was run until all transients were removed, then statistics of the flow were sampled until convergence was achieved.

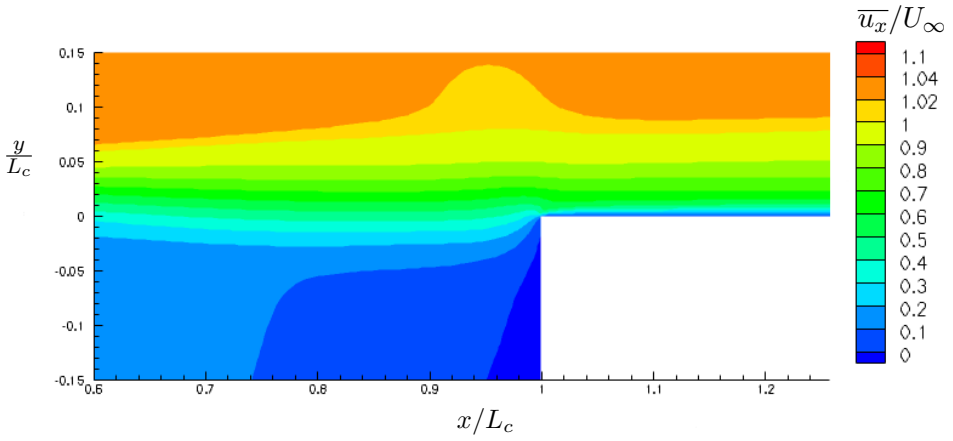

FIGURE 5.3: Mean streamwise velocity $\overline{u_x}$ near trailing edge.

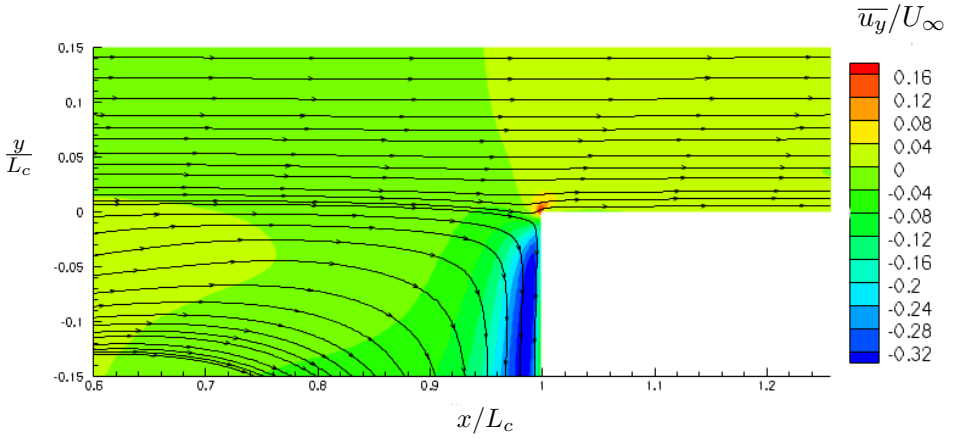

FIGURE 5.4: Mean streamwise velocity $\overline{u_y}$ near trailing edge, along with mean fluid streamlines.

5.2.1 Single-phase statistics

Fluid statistics were obtained for the low-Reynolds number flow simulation without bubbles. Statistics were obtained by sampling the velocity and pressure field over time until convergence was achieved. Statistics are also averaged in the spanwise (periodic) direction. Figures 5.3 and 5.4 plot the mean velocity field and mean streamlines near the trailing edge. The flow is from left to right. Downstream of the cavity leading edge, the flow separates with the high-momentum fluid on top and low-momentum fluid

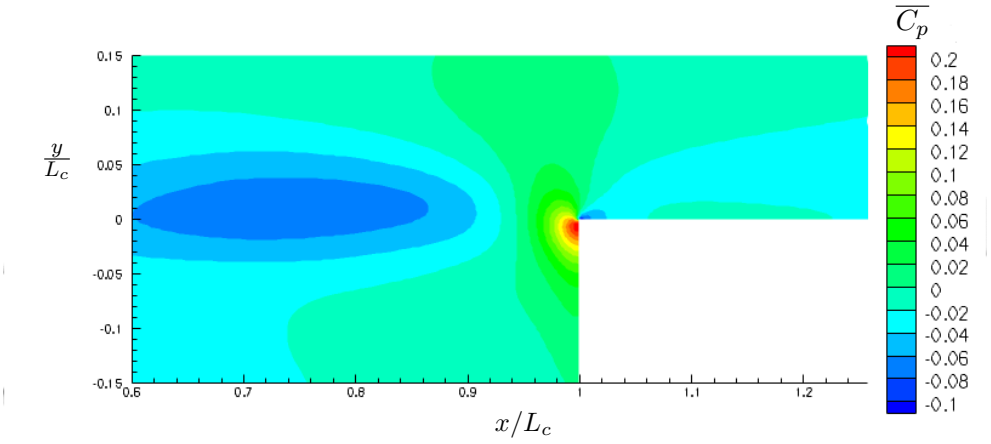

FIGURE 5.5: Mean pressure coefficient $\overline{C_p}$ near trailing edge.

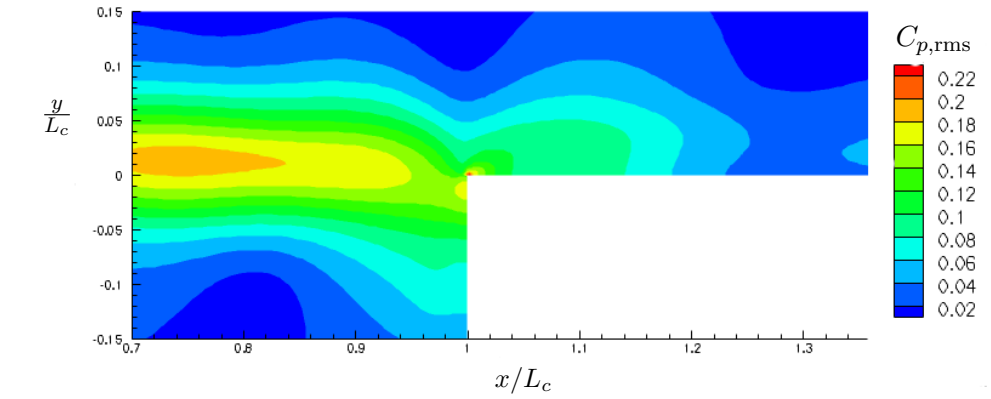

FIGURE 5.6: Pressure coefficient rms value $C_{p,\mathrm{rms}}$ near trailing edge.

recirculating in the cavity. The flow accelerates around the expansion corner at the trailing edge and a boundary layer develops downstream of the expansion corner.

Figures 5.5 and 5.6 plot the mean and rms of C_p in the flow near the trailing edge. When the flow separates from the leading edge, vortices are shed and travel downstream with the flow. This is shown in the plot of instantaneous C_p in Figure 5.7, taken from the spanwise mid-plane of the simulation. The centers of vortical structures are regions of low pressure, and this creates pressure fluctuations observes upstream of the trailing edge in Figure 5.6. When these vortices impinge onto the trailing edge, a high pressure region is formed on the upstream side of the trailing edge. There are large $C_{p,\mathrm{rms}}$ values

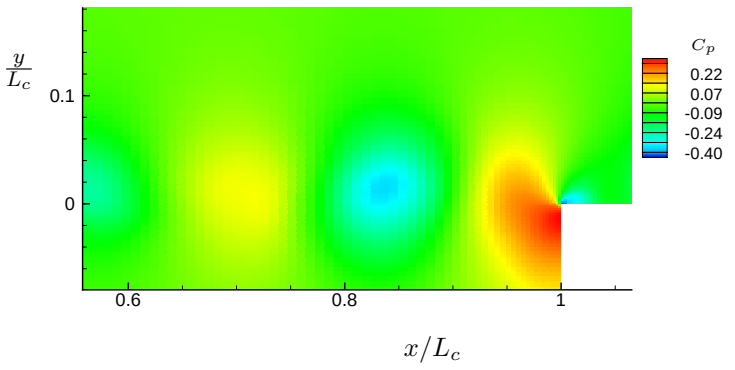

FIGURE 5.7: Instantaneous pressure coefficient C_p.

here since the pressure fluctuates from high pressure (vortex impinging) to low pressure. On the downstream side of the trailing edge, a low pressure region is formed due to the expansion of the flow, though the pressure fluctuates due to the downwash of the incoming vortices shed from the leading edge.

5.2.2 Cavitating flow

To model the gas nuclei, small bubbles with a radius of $R = 10\mu\text{m} = 0.01L_{\text{ref}}$ were injected near the leading edge of the cavity. The initial position of the bubble was determined randomly in the spanwise direction and within a small window with a height of 1.5mm from the cavity wall. Nuclei on the order of $\sim 10\mu$m are observed in water, though obtaining measurements of gas nuclei are difficult to measure [9]. The bubbles travel downstream with the flow and cavitate in the low-pressure regions, if the instantaneous pressure is low enough. Due to the low Reynolds number of the simulation, the minimum pressure that is required to create cavitation could only be obtained by reducing the cavitation number of the simulation to a value of $\sigma_v = -0.4$.

The Blake threshold pressure [81] is a relation that estimates the minimum pressure allowed in the flow (below which unstable bubble growth occurs), given the size of gas

nuclei in the flow. The Blake threshold pressure is defined as

$$P_c - P_v = -\frac{4\sigma}{3R}. \tag{5.3}$$

and a non-dimensional critical pressure σ_c can be defined as

$$\sigma_c = \frac{P_c - P_v}{\frac{1}{2}\rho_f U_\infty}. \tag{5.4}$$

The pressure required for cavitation inception is obtained by

$$\sigma_c = C_{p,\min} + \sigma_v \tag{5.5}$$

and the minimum pressure required for cavitation inception can be obtained, given the radius of the gas nuclei in the flow, minimum pressure coefficient and cavitation index.

For gas nuclei with a critical radius of 10μm, the critical pressure $\sigma_c = -0.4$ and a non-dimensional critical pressure of $C_{p,\min} = -0.8$ must be found in the flow for $\sigma_v = 0.4$. However, the minimum pressure coefficient $C_{p,\min}$ found in the low Reynolds number found in the simulation was -0.4, and therefore the cavitation number σ_v had to be reduced to -0.4 to obtain the critical minimum pressure required for cavitation. The cavitation number is smaller than the Liu and Katz [3] experiment, in which cavitation was observed at $\sigma_v \approx 0.9$ for the $U_\infty = 5$ m/s case, though the simulation Reynolds number Re_L is an order of magnitude smaller than the experiment.

Using the one-way coupled Euler-Lagrangian approach, we were able to obtain qualitatively similar results to the Liu and Katz [3] experiment in the low Reynolds number simulation. Bubbles traveled downstream with the shear-layer vortices and are impinged upon the trailing edge. Due to the downwash on an incoming vortex, cavitated bubbles collapse and move away from the high pressure region. This behavior is observed in Figure 5.8. A number of the gas nuclei have cavitated and grown to a large size and travel downstream with the vortices shed from the leading edge corner. Figure 5.8a shows cavitated nuclei traveling downstream in two vortices, v_a and v_b, where vortex v_a has already impinged upon the trailing edge and v_b is not far behind. In Figure 5.8b,

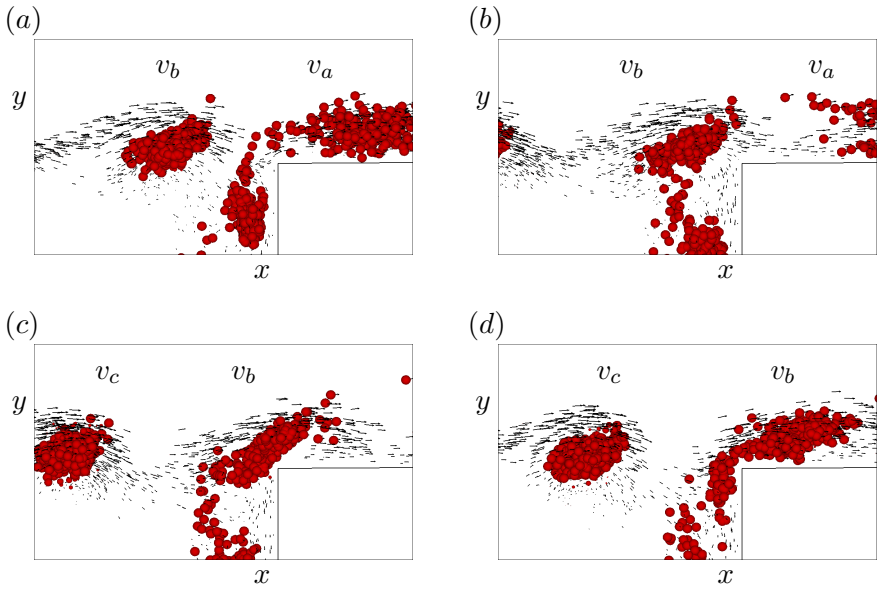

FIGURE 5.8: Instantaneous plots of bubble size and position near the cavity trailing edge. Figures (a)-(d) are sequential in time, with individual vortices denoted by v_a, v_b and v_c.

vortex v_a has traveled downstream from the leading corner and bubbles that were located near the trailing edge began to collapse and move away due the the high pressure region imposed by the downwash of vortex v_b. In Figures 5.8c and 5.8d show vortex v_b impinging upon the trailing edge and vortex v_c can be observed.

5.3 High Reynolds-number simulation

A second, high Reynolds-number simulation was also performed, with a Reynolds number equal to that of the Liu and Katz [3] experiment. The free-stream velocity was set to $U_\infty = 5000 U_{\text{ref}}$.

To obtain physical turbulent inflow, a separate simulation of a turbulent boundary layer was performed using a rescaling method developed by Lund et al. [65]. This involves performing a separate turbulent boundary layer simulation using a grid similar in size to the inflow plane of the cavity simulation and passing the instantaneous flow from the inflow simulation directly to the cavity inflow. The inflow near the bottom wall was obtained from the turbulent inflow simulation, while the flow near the top wall was

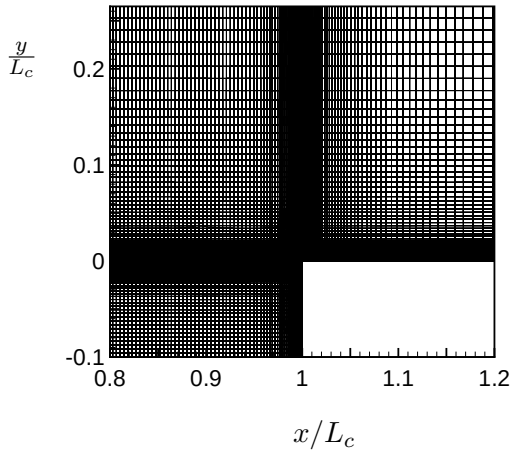

FIGURE 5.9: Computational mesh for the high Reynolds-number simulation, focused on the trailing edge.

set to the mean profile obtained from the inflow simulation. The inflow simulation grid spacing was similar to the cavity inflow section (parameters given below), with the inflow plane of the turbulent inflow simulation beginning $37.5L_{\text{ref}}$ units upstream of the cavity inflow plane. The momentum thickness $\theta/L_{\text{ref}} = 0.1$ and the boundary layer thickness $\delta_{99}/L_{\text{ref}} = 2.3$ at the inflow plane of the inflow simulation.

Periodic boundary conditions were applied in the spanwise direction, and a zero-gradient outflow boundary conditions were implemented. A mesh with 16 million grid points was used, with refinement at the leading and trailing edges and the walls of the simulation. Figure 5.9 shows the grid in the trailing edge region. The minimum y spacing is $\Delta y_{\text{min}}/L_{\text{ref}} = 0.05$. A boundary layer is grown from both the top and the bottom walls of the inflow and outflow channels with a growth ratio of 1.05 for 42 rows for a maximum wall-normal spacing of $\Delta y_{\text{max}}/L_{\text{ref}} = 0.388$. Within the cavity, the maximum $\Delta y/L_{\text{ref}} = 0.161$. From both the leading and trailing edge a boundary layer mesh is grown from the corner in the x-direction, with a minimum spacing of $\Delta x_{\text{min}}/L_{\text{ref}} = 0.05$. The boundary layer was grown with a ratio of 1.05 for 42 grid points, with a maximum spacing of $\Delta x_{\text{max}}/L_{\text{ref}} = 0.388$. A uniform grid is used in the spanwise direction, with a grid spacing of $\Delta z/L_{\text{ref}} = 0.397$. The simulation was run until all transients were removed, then statistics of the flow were sampled until convergence was achieved.

5.3.1 Single-phase statistics

The flow separates over the leading edge, with vortices being shed from the leading-edge corner which then travel downstream with the flow and impinge on the trailing edge corner. Downstream of the leading edge, a shear layer is formed, with high speed flow on the top side and low-speed flow underneath (See Figure 5.10a). When the flow approaches the trailing edge, the flow forms a recirculation zone in the cavity region and expands around the trailing edge corner. Figure 5.10b plots the mean $\overline{u_y}$ velocity along with the mean velocity streamlines. Good agreement is obtained with the mean flow observed in the Liu and Katz [3] experiment.

As the flow separates from the leading edge, vortices are formed which are shed from the leading edge corner. The centers of these vortical structures form low-pressure regions in the flow, though these vortical structures are not as prominent as in the low-Reynolds number simulation. As the flow approaches the trailing edge, a high pressure region is formed on the upstream side of the trailing edge corner. On the downstream side of the trailing edge corner, the flow expands and a low-pressure region is formed. The mean pressure coefficient $\overline{C_p}$ from the simulation is plotted in Figure 5.11a, along with the mean pressure profiles measured from the Liu and Katz [3] experiment (Figure 5.11b). Good agreement is obtained for $\overline{C_p}$ near the trailing edge, though a low-pressure region is observed in the cavity region of the simulation that is not as prominent in the Liu and Katz [3] experiment. Differences between $C_{p,\mathrm{rms}}$ are observed in Figure 5.12, where the experimental pressure fluctuation levels are higher than observed in simulation.

A likely cause of the differences is the three-dimensionality of the experiment. The simulation enforces periodicity in the spanwise direction and is not accounting for possible effects due to the constriction of the side walls or replicating the inflow to the cavity, which has been assumed to be a fully-developed zero pressure gradient boundary layer. These 3D effects were assumed to be negligible when these simulations were first performed, but these assumptions may not be correct. A. Verma (personal communication) has performed turbulent simulations of the single-phase cavity flow with spanwise wall to more closely match experimental conditions, and the $\overline{C_p}$ was found to be more representative of experiment. Also, the experimental measurements show a large negative

mean value of $\overline{u_y}$ in the flow upstream of the leading edge as compared to simulations, which is inconsistent with a zero pressure-gradient turbulent boundary layer inflow.

5.3.2 Cavitating flow

Bubbles were injected near the leading edge (within a window with a height of 1.5mm and distributed uniformly in the spanwise direction). 10 bubbles were injected every timestep. Three separate bubbly simulations with varying bubble sizes were performed. Each run has bubbles injected with a uniform size. The size of the bubbles were equal to $20, 25$ and 30mm for simulations $C1, C2$ and $C3$, respectively. Cavitation inception was observed for all three simulations. The Weber number based on an initial radius $R_o = 10$ μm ($\mathrm{We} = \rho_f U_\infty^2 R_o/\sigma$) is 3.406 to match conditions for bubbles in water.

Figure 5.13 is an instantaneous plot of bubble position, taken from $t = 0.02 L_{\mathrm{ref}}/U_{\mathrm{ref}}$ from the high-Reynolds number simulations for three different bubble sizes. Bubbles are proportional to actual size in the figures and the color contours show the acceleration of the bubble radius. Figure 5.13a plots the bubble position in the $x-y$ plane of bubbles with $-1 \leq Y_z/L_{\mathrm{ref}} \leq 1$ from the simulation with bubbles with $R_o = 20$ μm. Figure 5.13b plots the bubble position in the $x-z$ plane from the simulation with bubbles with $R_o = 20$ μm. Figure 5.13c plots the bubble position in the $x-y$ plane of bubbles with $-1 \leq Y_z/L_{\mathrm{ref}} \leq 1$ from the simulation with bubbles with $R_o = 25$ μm. Figure 5.13d plots the bubble position in the $x-z$ plane from the simulation with bubbles with $R_o = 25$ μm. Figure 5.13e plots the bubble position in the $x-y$ plane of bubbles with $-1 \leq Y_z/L_{\mathrm{ref}} \leq 1$ from the simulation with bubbles with $R_o = 30$ μm. Figure 5.13f plots the bubble position in the $x-z$ plane from the simulation with bubbles with $R_o = 30$ μm. The cavitation of the gas nuclei is the most prominent at the trailing edge of the cavity, though also observed in the the shear-layer region (downstream of the leading edge). As the cavitation bubbles approach the high-pressure zone near the trailing edge many bubbles collapse ($\dot{R} < 0$). The behavior of the flow is qualitatively similar to the Liu and Katz [3] experiment, with the expansion of the flow around the trailing edge being the area most prone to cavitation. Also, cavitation is observed in the vortex cores that are shed from the leading edge, as in experiment.

Increased levels of cavitation were observed for bubbles with a larger radius. This is consistent with the Blake formulation (Eqn. 5.3), with larger bubbles having a larger critical pressure and thus cavitate sooner than small bubbles. The sensitivity to initial bubble radius increases the difficulty in predicting cavitation inception in fluid devices and applications, since gas nuclei size distributions are difficult to measure and to predict [9].

The minimum pressure coefficient $C_{p,\min}$ observed in the flow ~ 1.1. From the cavitation inception index given in the Liu and Katz [3] experiment ($\sigma_v = \sigma_i = 0.87$), the critical bubble radius obtained from

$$C_{p,\min} = \sigma_c - \sigma_i = -\frac{1}{1/2\rho_f U_\infty^2}\frac{4\sigma}{3R_o} - \sigma_i \tag{5.6}$$

is $R_o = 18$ μm, which is similar to the size of bubbles injected in the simulation. If the bubble size in the simulation were to be smaller than $R_o = 18$ μm, cavitation inception would not occur. This is consistent with the reduction of cavitation for the simulation with small bubble size $R_o = 20$ μm compared to simulations with larger initial bubble size.

The two-way coupled simulations along with the modeling of bubble behavior with the Rayleigh-Plesset equation of Shams et al. [29] observed cavitation that was less prevalent downstream of the trailing edge than our simulations, though the initial gas nuclei was larger $R_o \sim 50$ μm. Physics currently not included in the one-way coupled simulations, such as two-way coupling, bubble breakup and coalescence are likely to modify the flow. Two-way coupling effects will increase the local pressure when bubbles move into a region of the flow, which will reduce the prevalence of cavitation.

The one-way coupled Euler-Lagrangian bubble model coupled with the Rayleigh-Pleset equation appears to over-predict cavitation downstream of the trailing edge, though these preliminary results are promising. Cavitation is observed in the low-pressure vortex cores and at the expansion corner at the trailing edge. The one-way coupled Euler-Lagrangian accurately predicts the inception of cavitation at the correct pressures and bubble sizes. The one-way coupled model captures the instantaneous nature of the

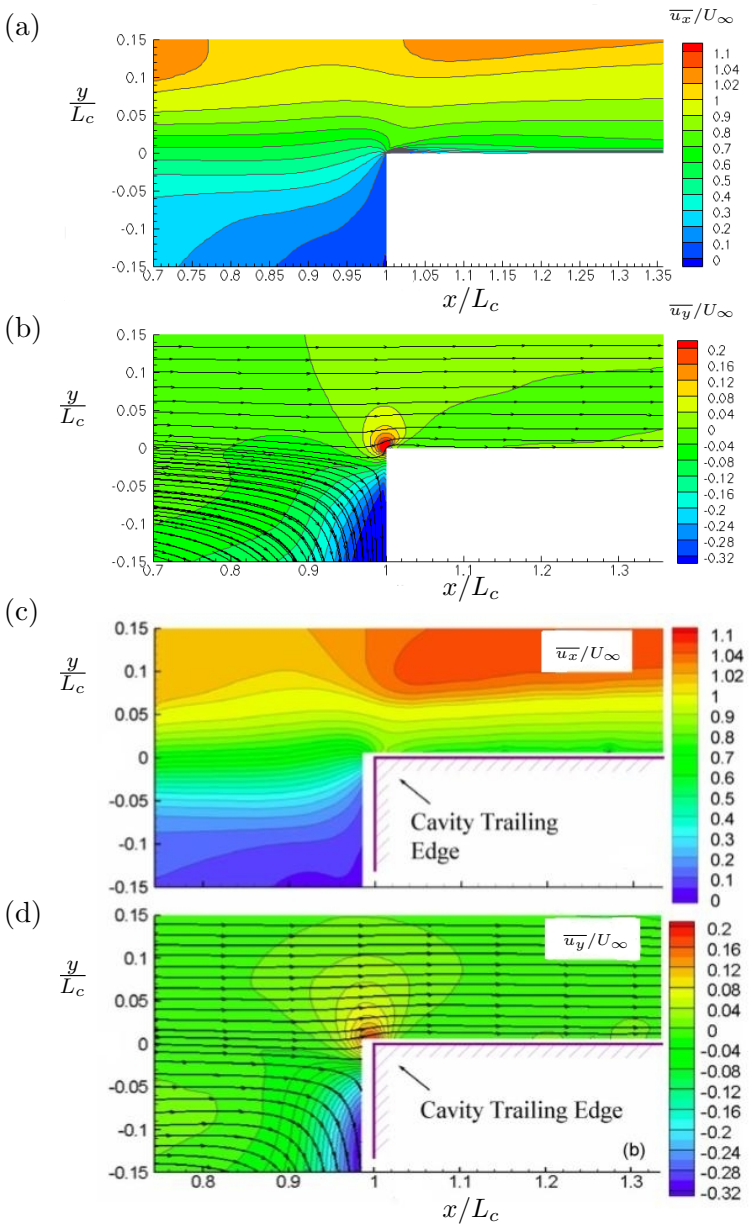

FIGURE 5.10: Comparison of mean velocities and streamlines between simulation and the Liu and Katz [3] experiment. (a) Plot of $\overline{u_x}$ from LES simulation (b) Plot of $\overline{u_y}$ from simulation, along with velocity streamlines. (c) Plot of $\overline{u_x}$ from Liu and Katz [3]. (d) Plot of $\overline{u_y}$ from Liu and Katz [3], along with velocity streamlines.

flow and residence time of bubbles in low and high-pressure areas, which are critical in predicting instantaneous bubble behavior and cavitation inception.

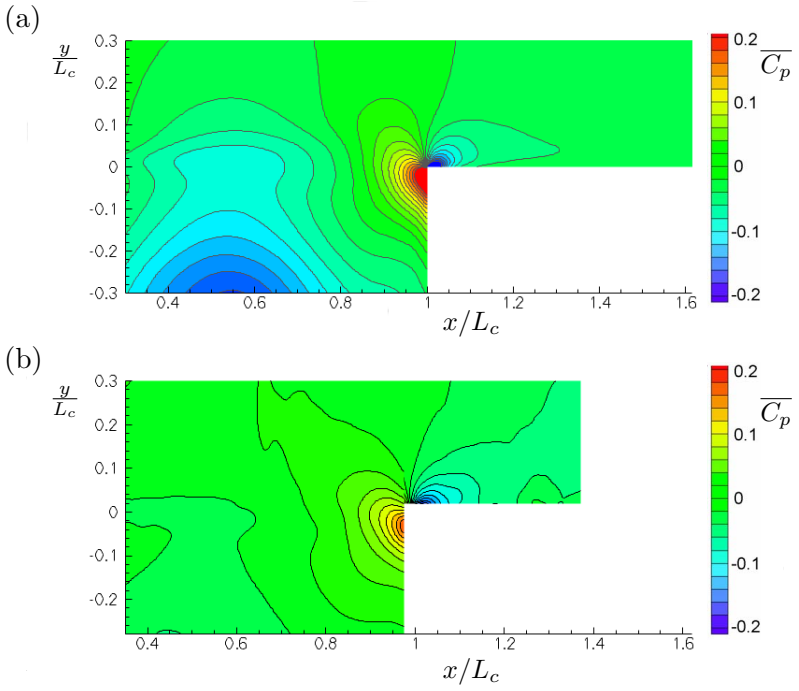

FIGURE 5.11: Comparison of mean pressure coefficient $\overline{C_p}$ between simulation and the Liu and Katz [3] experiment. (a) Plot of $\overline{C_p}$ from LES simulation (b) Plot of $\overline{C_p}$ from Liu and Katz [3].

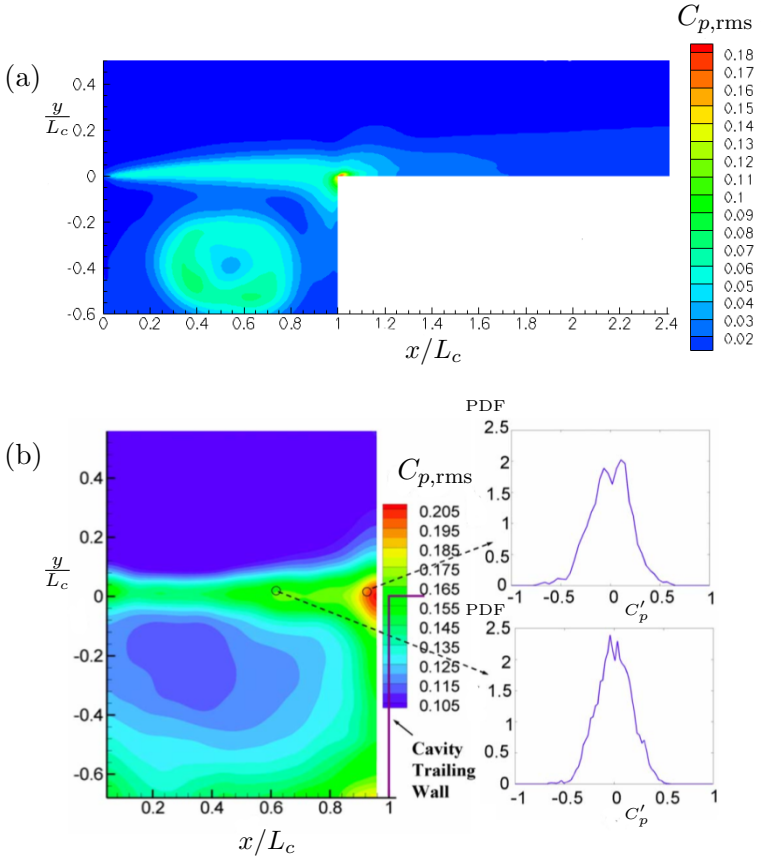

FIGURE 5.12: Comparison of mean pressure coefficient $C_{p,\mathrm{rms}}$ between simulation and the Liu and Katz [3] experiment. (a) Plot of $C_{p,\mathrm{rms}}$ from LES simulation (b) Plot of $C_{p,\mathrm{rms}}$ from Liu and Katz [3].

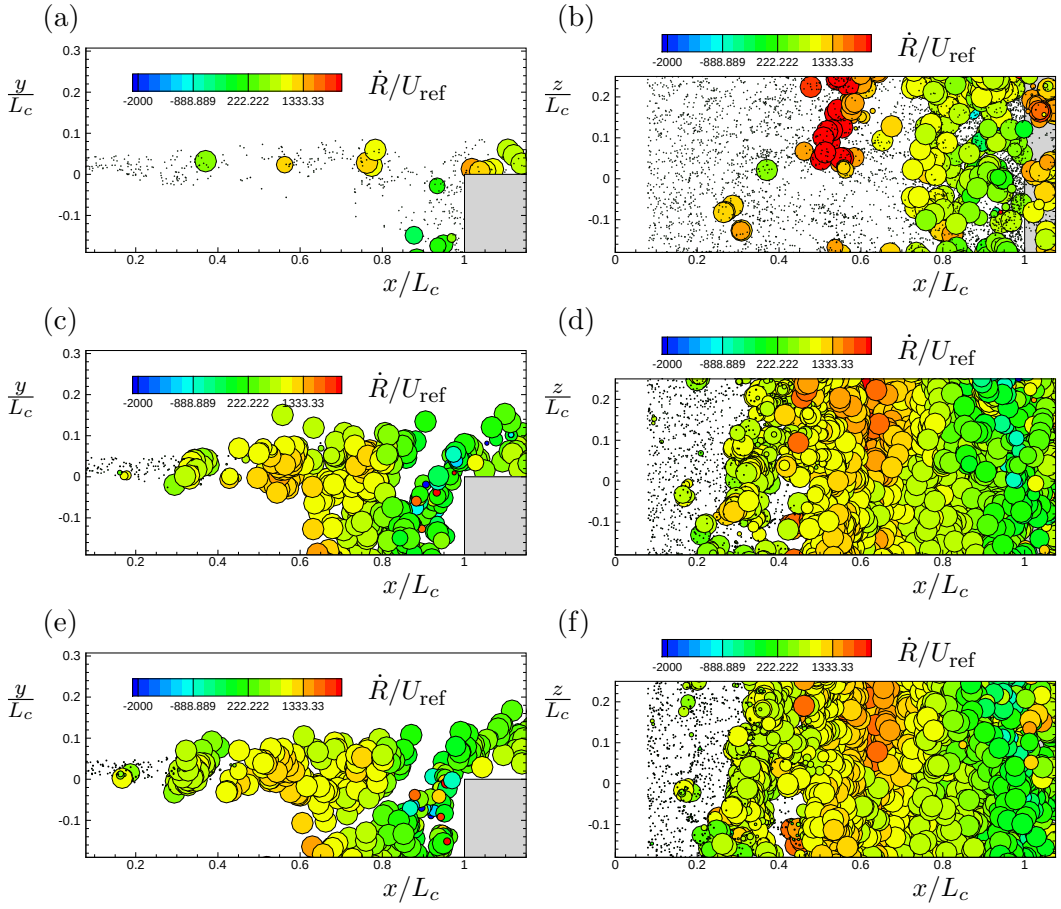

FIGURE 5.13: Plots of bubble instantaneous position at $t = 0.02L_{\mathrm{ref}}/U_{\mathrm{ref}}$ near the cavity trailing edge. Color contours plot the instantaneous radial acceleration for each bubble. (a) $x-y$ plane for $R_o = 20$ μm. (b) $x-z$ plane for $R_o = 20$ μm. (c) $x-y$ plane for $R_o = 25$ μm. (d) $x-z$ plane for $R_o = 25$ μm. (e) $x-y$ plane for $R_o = 30$ μm. (f) $x-z$ plane for $R_o = 30$ μm.

Bibliography

[1] C. Colin, J. Fabre, and A. E. Dukler. Gas-liquid flow at microgravity conditions - 1. *Int. J. Multiphase Flow*, 17:533–544, 1991.

[2] W. C. Sanders, E. S. Winkel, D. R. Dowling, M. Perlin, and S. L. Ceccio. Bubble friction drag reduction in a high-Reynolds-number flat-plate turbulent boundary layer. *J. Fluid Mech.*, 552:353–380, 2006.

[3] X. Liu and J. Katz. Cavitation phenomena occurring due to interaction of shear layer vortices with the trailing corner of a two-dimensional open cavity. *Phys. of Fluids*, 20:041702, 2008.

[4] M. E. McCormick and R. Bhattacharyya. Drag reduction of a submersible hull by electrolysis. *Naval Engrs. J.*, 85(2):11–16, 1973.

[5] S. Ceccio. Friction drag reduction of external flows with bubble and gas injection. *Annu. Rev. Fluid Mech.*, 42:183–203, 2010.

[6] K. M. Kalumuck and G. L. Chahine. The use of cavitating jets to oxidize organic compounds in water. *J. Fluids Eng.*, 122:465–470, 2000.

[7] E. N. Harvey, D. K. Barnes, W. C. McElroy, A. H. Whiteley, D. C. Pease, and K. W. Cooper. Bubble formation in animals: I. physical factors. *J. Cell. and Comp. Physiol.*, 24:1–22, 1944.

[8] R. E. A. Arndt. Cavitation in vortical flows. *Annu. Rev. Fluid Mech.*, 34:143–175, 2002.

[9] C. E. Brennen. *Cavitation and Bubble Dynamics*. Oxford Univ. Press, Oxford, 1995.

[10] File: Turbine Francis worn. http://en.wikipedia.org/wiki/File:Turbine_Francis_Worn.JPG, 2011.

[11] R. E. A. Arndt. Cavitation in fluid machinery and hydraulic structures. *Annu. Rev. Fluid Mech.*, 13:273–328, 1981.

[12] M. Callenaere, J.-P. Franc, J.-M. Michel, and M. Riondet. The cavitation instability induced by the development of a re-entrant jet. *J. Fluid Mech.*, 444:223–256, 2001.

[13] S. Elghobashi. On predicting particle-laden turbulent flows. *Appl. Sci. Res.*, 52: 309–329, 1994.

[14] D. Legendre and J. Magnaudet. The lift force on a spherical bubble in a viscous linear shear flow. *J. Fluid Mech.*, 368:81–126, 1998.

[15] S. Pope. *Turbulent Flows*. Cambridge Univ. Press, Cambridge, UK, 2000.

[16] R. Mittal and P. Moin. Suitability of upwind biased schemes for large-eddy simulation. *AIAA J.*, 30(8):1415–1417, 1997.

[17] F. H. Harlow and J. E. Welch. Numerical calculation of time-dependent viscous incompressible flow of fluid with free surface. *Phys. Fluids*, 8:2182–2189, 1965.

[18] K. Mahesh, G. Constantinescu, and P. Moin. A numerical method for large-eddy simulation in complex geometries. *J. Comp. Phys.*, 197:215–240, 2004.

[19] S. O. Unverdi and G. Tryggvason. A front-tracking method for viscous, incompressible multi-fluid flows. *J. Comp. Phys.*, 100:25–37, 1992.

[20] G. Tryggvason, B. Bunner, A. Esmaeeli, D. Juric, N. Al-Rawahi, W. Tauber, J. Hun, and Y.-J. Jan. A front-tracking method for the computations of multiphase flow. *J. Comp. Phys.*, 169:708–759, 2001.

[21] A. Kanai and H. Miyata. Direct numerical simulation of wall turbulent flows with microbubbles. *Int. J. Num. Meth. Fluids*, 35:593–615, 2001.

[22] T. Kawamura and Y. Kodama. Numerical simulation method to resolve interactions between bubbles and turbulence. *Int. J. Heat & Fluid Flow*, 23:627–638, 2002.

[23] S. Popinet and S. Zaleski. Bubble collapse near a solid boundary: a numerical study of the influence of viscosity. *J. Fluid Mech.*, 464:137–163, 2002.

[24] J. Lu, A. Fernández, and G. Tryggvason. The effect of bubbles on the wall drag in a turbulent channel flow. *Phys. of Fluids*, 17(095102), 2005.

[25] J. Dacles-Mariani, G. G. Zilliac, G. J. Chow, and P. Bradshaw. Numerical/experimental study of a wingtip vortex in the near field. *AIAA Journal*, 33:1561–1568, 1995.

[26] C.-T. Hsiao and L. L. Pauley. Numerical study of the steady-state tip vortex flow over a finite-span hydrofoil. *ASME J. Fluids Engrg.*, 120:345–353, 1998.

[27] C.-T. Hsiao and G. L. Chahine. Scaling of tip vortex cavitation inception noise with a bubble dynamics model accounting for nuclei size distribution. *ASME J. Fluids Engrg.*, 127:55–65, 2005.

[28] C.-T. Hsiao and G. L. Chahine. Numerical study of cavitation inception due to vortex/vortex interaction in a ducted propeller. *J. Ship Res.*, 52(2):114–123, 2008.

[29] E. Shams, J. Finn, and S. V. Apte. A numerical scheme for euler-lagrange simulation of bubbly flows in complex systems. *Int. J. Numer. Meth. Fluids*, 2010.

[30] M. Poreh and J. E. Cermak. Study of diffusion from a line source in a turbulent boundary layer. *Int. J. Heat Mass Transfer*, 7:1083–1095, 1964.

[31] M. R. Maxey, B. K. Patel, E. J. Chang, and L-P Wang. Simulations of dispersed turbulent multiphase flows. *Fluid Dyn. Res.*, 20:143–156, 1997.

[32] M. R. Maxey and G. L. Dent. Some features of particle sedimentation at finite reynolds numbers. In *Third Int. Conf. on Multiphase Flow, ICMF*, Lyon, France, 1998.

[33] G. L. Dent. *Aspects of particle sedimentation in dilute flows at finite Reynolds numbers.* PhD thesis, Brown University, Providence, R.I., 1999.

[34] S. Lomholt. *Numerical investigations of macroscopic particle dynamics in microfluids.* PhD thesis, RisøNational Laboratory, Roskilde, Denmark, 2000.

[35] S. Lomholt, B. Stenum, and M. R. Maxey. Experimental verification of the force coupling method for particulate flows. *Int. J. Multiphase Flow*, 28:225–246, 2002.

[36] M. Mattson and K. Mahesh. Towards numerical simulation of cavitating flows in complex geometries. In *27th Symp. on Naval Hydro.*, Seoul, South Korea, 2008.

[37] M. Mattson and K. Mahesh. Simulation of bubble migration in a turbulent boundary layer. *In press, Phys. of Fluids*, 2011.

[38] V. E., Jr Johnson and T. Hsieh. The influence of the trajectories of gas nuclei on cavitation inception. *6th Naval Hydrodynamics Symp.*, pages 163–179, 1966.

[39] N. H. Thomas, T. R. Auton, K. Sene, and J. C. R. Hunt. Entrapment and transport of bubbles by plunging water. In W. Brutsaert and G. H. Jirka, editors, *Gas Transfer at Water Surfaces*, pages 255–268. D. Reidel Publishing Co., 1984.

[40] T. R. Auton, J. C. R. Hunt, and M. Prud'homme. The force exerted on a body in inviscid unsteady non-uniform rotational flow. *J. Fluid Mech.*, 197:241–257, 1988.

[41] W. L. Haberman and R. K. Morton. An experimental investigation of the drag and shape of air bubbles rising in various liquids. David W. Taylor Model Basin Report 802, Sept. 1953.

[42] T. R. Auton. The lift force on a spherical body in a rotational flow. *J. Fluid Mech.*, 183:199–218, 1987.

[43] G. K. Batchelor. *An Introduction to Fluid Dynamics.* Cambridge Univ. Press, Cambridge, UK, 1967.

[44] C. E. Brennen. *Cavitation and Bubble Dynamics.* Oxford Univ. Press, Oxford, 1995.

[45] P. Babu. *Simulation and modeling of three turbulent flow problems.* PhD thesis, University of Minnesota, Minneapolis, Minnesota, 2007.

[46] W. H. Press, S. A. Tekolsky, W. T. Vetterling, and B. P. Flannery. *Numerical Recipes in Fortran 77: The Art of Scientific Computing.* Cambridge Univ. Press, Cambridge, 1992.

[47] M. P. Allen and D. J. Tildesley. *Computer Simulation of Liquids*. Clarendon Press, New York, 1988.

[48] A. M. Kamp, A. K. Chesters, C. Colin, and J. Fabre. Bubble coalescence in turbulent flows: A mechanistic model for turbulence-induced coalescence applied to microgravity bubbly pipe flow. *Int. J. of Multiphase Flow*, 27:1363–1396, 2001.

[49] S. Muppidi and K. Mahesh. Direct numerical simulation of passive scalar transport in transverse jets. *J. Fluid Mech.*, 598:335–360, 2008.

[50] H. Lamb. *Hydrodynamics*. Dover Publications, New York, 6th edition, 1945.

[51] A. K. Chesters. The modelling of coalescence processes in fluid-liquid dispersions – a review of current understanding. *Trans. I. Chem. E.*, 69 (part A):353–363, 1991.

[52] A. K. Chesters and G. Hofman. Bubble coalescence in pure liquids. *Applied Sci. Res.*, 38:1083–1095, 1982.

[53] P. C. Duineveld. *Bouncing and coalescence of two bubbles in water*. PhD thesis, University of Twente, Enschede, Netherlands, 1994.

[54] C. A. Coulaloglou and L. L. Tavlarides. Description of interaction processes in agitated liquid-liquid dispersions. *Chem. Eng. Sci.*, 32:1289–1297, 1977.

[55] C. L. Merkle and S. Deutsch. Microbubble drag reduction in liquid turbulent boundary layers. *Appl. Mech. Rev.*, 45(3):103–127, 1992.

[56] N. K. Madavan, S. Deutsch, and C. L. Merkle. Measurements of local skin friction in a microbubble-modified turbulent boundary layer. *J. Fluid Mech.*, 156:237–256, 1985.

[57] C. Gabillet, C. Colin, and J. Fabre. Experimental study of bubble injection in a turbulent boundary layer. *Int. J. Multiphase Flow*, 28:553–578, 2002.

[58] B. Jacob, A. Olivieri, M. Miozzi, E. F. Campana, and R. Piva. Drag reduction by microbubbles in a turbulent boundary layer. *Phys. Fluids*, 22:115104, 2010.

[59] S. Pal, C. L. Merkle, and S. Deutsch. Bubble characteristics and trajectories in a microbubble boundary layer. *Phys. Fluids*, 31(4):744–751, 1988.

[60] J. Xu, M. R. Maxey, and G. Karniadakis. Numerical simulation of turbulent drag reduction using micro-bubbles. *J. Fluid Mech.*, 468:271–281, 2002.

[61] A. Ferrante and S. Elghobashi. On the physical mechanisms of drag reduction in a spatially developing turbulent boundary layer laden with microbubbles. *J. Fluid Mech.*, 503:345–355, 2004.

[62] A. Ferrante and S. Elghobashi. Reynolds number effect on drag reduction in a microbubble-laden spatially developing turbulent boundary layer. *J. Fluid Mech.*, 543:93–106, 2005.

[63] M. Mattson and K. Mahesh. Euler-lagrangian simulation of bubble migration in a turbulent boundary layer. In *28th Symp. on Naval Hydro.*, Pasadena, California, 2010.

[64] W. C. Sanders. *Bubble drag reduction in a flat plate boundary layer at high Reynolds numbers and large scales.* PhD thesis, Department of Mechanical Engineering, University of Michigan, 2004.

[65] T. S. Lund, X. Wu, and K. D. Squires. Generation of turbulent inflow data for spatially-developing boundary layer simulations. *J. Comp. Phys.*, 140:233–258, 1998.

[66] M. P. Simens, J. Jiménez, S. Hoyas, and Y. Mizuno. A high-resolution code for turbulent boundary layers. *J. Comp. Phys.*, 228:4218–4231, 2009.

[67] M. R. Maxey, E. J. Chang, and L-P Wang. Interactions of particles and microbubbles with turbulence. *Exp. Thermal and Fluid Sci.*, 12:417–425, 1996.

[68] M. R. Head and P. Bandyopadhyay. New aspects of turbulent boundary-layer structure. *J. Fluid Mech.*, 107:297–338, 1981.

[69] H. Schlichting. *Boundary-Layer Theory.* McGraw Hill, 7th edition, 1979.

[70] K. Wieghardt. Über ausbreitungsvorgänge in turbulenten reibungsschichten. *Z. angew. Math. Mech.*, 27(11/12):346–355, 1948.

[71] E. Olmos, C. Gentric, Ch Vial, G. Wild, and N. Midoux. Numerical simulation of multiphase flow in bubble column reactors. Influence of bubble coalescence and break-up. *Chem. Eng. Sci.*, 56:6359–6365, 2001.

[72] M. Sommerfeld, E. Bourloutski, and D. Bröder. Euler/Lagrange calculations of bubbly flows with consideration of bubble coalescence. *Canadian J. of Chem. Eng.*, 81:508–518, 2003.

[73] P. Chen, J. Sanyal, and M. P. Duduković. Numerical simulation of bubble columns flows: effect of different breakup and coalescence closures. *Chem. Eng. Sci.*, 60: 1085–1101, 2005.

[74] E. I. V. van den Hengel, N. G. Deen, and J. A. M. Kuipers. Application of coalescence and breakup models in a discrete bubble model for bubble columns. *Ind. Eng. Chem. Res.*, 44:5233–5245, 2005.

[75] D. Darmana, N. G. Deen, and J. A. M. Kuipers. Parallelization of an Euler–Lagrange model using mixed domain decomposition and a mirror domain technique: Application to dispersed gas–liquid two–phase flow. *J. Comp. Phys.*, 220:216–248, 2006.

[76] G. A. Bokkers, J. A. Laverman, M. van Sint Annaland, and J. A. M. Kuipers. Modelling of large–scale dense gas–solid bubbling fluidised beds using a novel discrete bubble model. *Chem. Eng. Sci.*, 61:5290–5302, 2006.

[77] M. J. Prince and H. W. Blanch. Bubble coalescence and break–up in air–sparged bubble columns. *A.I.Ch.E. Journal*, 36(10):1485–1499, 1990.

[78] C. J. Lawn. The determination of the rate of dissipation in turbulent pipe flow. *J. Fluid Mech.*, 48(3):477–505, 1971.

[79] M. Rudman and H. M. Blackburn. Large eddy simulation of turbulent pipe flow. In *2nd Intnl. Conf. CFD in Minerals and Process Ind.*, pages 503–508, Melbourne, Australia, December 1999.

[80] J. G. M. Eggels, F. Unger, M. H. Weiss, J. Westerweel, R. J. Adrian, R. Friedrich, and F. T. M. Nieuwstadt. Fully developed turbulent pipe flow: a comparison

between direct numerical simulation and experiment. *J. Fluid Mech.*, 268:175–209, 1994.

[81] F. G. Blake. The onset of cavitation in liquids. Tech. Memo 12, Harvard Univ., 1949.

Appendix A

Bubble time integration

This appendix gives the order of operations for the bubble and carrier fluid time integration for the one-way coupled EL formulation, including collision, coalescence and bubble oscillation.

Begin simulation

$t_n = t_1$

Do while $t_n < t_{\text{final}}$

Advance carrier fluid by Δt (from t_1 to t_2) to obtain $\vec{u}_2$ and P_2

Calculate collision partners

Do while $t_n < t_2$

Determine minimum time to collision, Δt_{col}

Obtain $\frac{dv}{dt}(t_n)$ for each bubble

Set $\Delta t^* = \min\left(\Delta t_{\text{col}}, \Delta t_{\text{bub}}, t_2 - t_n\right)$

Advance all bubble positions and velocities by Δt^* to obtain $\vec{v}^{k+1}$ and $\vec{Y}^{k+1}$

Apply collision / coalescence models and update relevant collision partners

Do while $t_n < t^{k+1}$ (for each bubble individually)

Obtain P_n

Set $\Delta t^*_{\text{RK}} = \min\left(\Delta t_{\text{RK}}, t^{k+1} - t_n\right)$

Advance bubble radius by Δt^*_{RK} to obtain R_{n+1}

$t_{n+1} = t_n + \Delta t^*_{\mathrm{RK}}$

end do

end do

end do

Appendix B

2nd-order spatial interpolation

This appendix describes a 2nd-order spatial interpolation to obtain carrier-fluid properties from the control-volume centroids at a bubble centroid location. The control volume is located at $\vec{x} = \vec{x}_{\mathrm{cv}}$ and the bubble at $\vec{x} = \vec{Y}$. The vector $\vec{s}$ is a vector of relative position between the control volume centroid and the bubble:

$$\vec{s} = \vec{Y} - \vec{x}_{\mathrm{cv}}. \tag{B.1}$$

The unit vector $\hat{s}$ is defined as $\hat{s} = \vec{s}/\left|\vec{s}\right|$, where $\left|\vec{s}\right|$ is the magnitude of the vector $\vec{s}$. A Taylor expansion for a function f about the control volume centroid can be written as

$$f(\vec{x} + \vec{s}) = f(\vec{x}) + \left|\vec{s}\right| \frac{\partial f}{\partial s} + \frac{\left|\vec{s}\right|^2}{2} \frac{\partial^2 f}{\partial s^2}, \tag{B.2}$$

where the gradients of f with respect to $\vec{s}$ are

$$\frac{\partial f}{\partial s} = \frac{\partial f}{\partial x_i}\hat{s}_i = \frac{\partial f}{\partial x}\hat{s}_x + \frac{\partial f}{\partial y}\hat{s}_y + \frac{\partial f}{\partial z}\hat{s}_z \tag{B.3}$$

in Cartesian coordinates. The second derivative of f can be obtained by taking the derivative of $\partial f/\partial s$, which is

$$\frac{\partial^2 f}{\partial s^2} = \frac{\partial}{\partial s}\left(\frac{\partial f}{\partial s}\right). \tag{B.4}$$

This can be expressed in Cartesian coordinates by transforming derivatives into the Cartesian coordinates

$$\frac{\partial}{\partial s}\left(\frac{\partial f}{\partial s}\right) = \frac{\partial}{\partial x_j}\left(\frac{\partial f}{\partial s}\right)\hat{s}_j = \frac{\partial}{\partial x_j}\left(\frac{\partial f}{\partial x_i}\hat{s}_i\right)\hat{s}_j, \tag{B.5}$$

which then can be expanded to

$$\frac{\partial}{\partial x_j}\left(\frac{\partial f}{\partial x}\hat{s}_x + \frac{\partial f}{\partial y}\hat{s}_y + \frac{\partial f}{\partial z}\hat{s}_z\right)\hat{s}_j, \tag{B.6}$$

and in its fully expanded form as

$$\begin{aligned}\frac{\partial^2 f}{\partial s^2} \quad = \quad & \frac{\partial}{\partial x}\left(\frac{\partial f}{\partial x}\hat{s}_x + \frac{\partial f}{\partial y}\hat{s}_y + \frac{\partial f}{\partial z}\hat{s}_z\right)\hat{s}_x + \\ & \frac{\partial}{\partial y}\left(\frac{\partial f}{\partial x}\hat{s}_x + \frac{\partial f}{\partial y}\hat{s}_y + \frac{\partial f}{\partial z}\hat{s}_z\right)\hat{s}_y + \\ & \frac{\partial}{\partial z}\left(\frac{\partial f}{\partial x}\hat{s}_x + \frac{\partial f}{\partial y}\hat{s}_y + \frac{\partial f}{\partial z}\hat{s}_z\right)\hat{s}_z.\end{aligned} \tag{B.7}$$

The above expression can be simplified into the following expression based on the 2nd-derivative of f in Cartesian space and the products of the vector $\vec{s}$

$$\frac{\partial^2 f}{\partial s^2} = \frac{\partial^2 f}{\partial x_j \partial x_i}\hat{s}_i\hat{s}_j = F_{ij}\hat{s}_j\hat{s}_i, \tag{B.8}$$

where $F_{ij} = \partial^2 f/\partial x_i \partial x_j$ is a 3×3 tensor. The Taylor series expansion can be written in Cartesian coordinates as

$$f(\vec{x}+\vec{s}) = f(\vec{x}) + |\vec{s}|\frac{\partial f}{\partial x_i}\hat{s}_i + \frac{|\vec{s}|^2}{2}F_{ij}\hat{s}_j\hat{s}_i. \tag{B.9}$$